DISSERTATION

DEVELOPING HIGH-PERFORMANCE MICROFLUIDIC PAPER-BASED ANALYTICAL DEVICES

Submitted by

Michael Paul Nguyen

Department of Chemistry

In partial fulfillment of the requirements

For the Degree of Doctor of Philosophy

Colorado State University

Fort Collins, Colorado

Summer 2018

Doctoral Committee:

Advisor: Charles S. Henry

Alan Van Orden
Steven H. Strauss
Anthony J. Marchese

ABSTRACT

DEVELOPING HIGH-PERFOMANCE MICROFLUIDIC PAPER-BASED ANALYTICAL DEVICES

Small-scale systems to manipulate fluids, also referred to as microfluidics, have proven effective at reducing analytical costs by increasing the portability of diagnostic devices. Microfluidic paper-based analytical devices (μPADs) have also proven to be cost-effective while remaining disposable, possessing the capacity to store reagents, and producing quantitative diagnostic results. These benefits have lead the field to increase exponentially since the seminal publication, with 63 review articles currently published on the subject. Most articles in the field focus on three topics: 1) new applications, 2) new methods of analysis with broad applicability, and 3) new ways to manipulate fluids in devices. A host of new analytes and clever architectures are being developed for a variety of applications, including environmental analysis and diagnostics. However, several critical obstacles remain for μPADs including improving detection limits, reducing analysis time, increasing selectivity, and increasing the range of measurable analytes.

The work described in this dissertation presents three studies that address these issues. The first study examines simple factors to improve sample delivery through a cellulose channel that directly and significantly impact detection limits. Here I show how common μPAD designs lose roughly 50% of sample prior to quantification. This major challenge has been solved through geometry changes that led to a 94% increase in signal when compared to standard designs. While Ni(II) detection was used to study the system, the methods are translated to Mn(II) detection, antibiotic purity tests and determination of nitrite in saliva suggesting the broad applicability of the methods.

The second study aimed at decreasing analysis time by utilizing multiple layers of paper in μPADs. I present the ability to tune speed, distance, and time at which the fluid travels with the formation of a microchannel between the layers. By increasing both the number of paper layers and the distance between them, the solution flux is dramatically increased in agreement with theoretical predictions. However, experimental flow rates deviate from predictions at large spacings. The detailed characterization and current understanding of the fast flow properties allow us to design assays that take seconds to complete instead of minutes along with improved analytical performance.

Developing a selective test for Al(III) in food, mining and water samples is the goal of the last study. To address this need, a fluorescent ligand selective for Al(III) was synthesized and characterized on a μPAD for the first time. A distance-based μPAD for Al(III) exhibited a linear response from 2–55 ppm and a limit of detection of 2 ppm. This chemistry was also further developed with a radial μPAD that measures diameter of a color response as opposed to distance. Despite a smaller linear range with this radial device, the limit of detection is 0.9 ppm, which is below the concentration relevant to plant health. All three of these studies highlight improving the analytical performance of μPADs with carefully selected assays and deliberate device design.

ACKNOWLEDGMENTS

First, I would like to acknowledge and thank my advisor, Professor Chuck Henry, for taking a chance and providing a supportive space for me to continue my graduate work. You take your role as mentor above and beyond and I hope to one day inspire those around me as you have with me. Next, I want to thank my former advisor, Professor Matt Shores, for helping shape the tools necessary to becoming a meticulous scientist and a critical thinker. While in the Shores group, both Dr. David Boston and Dr. Indrani Bhowmick were crucial mentors and friends during my development as a young investigator.

Second, I would like to thank my coworkers in the Henry group for helping me get started in a new laboratory and continue to help me tackle my analytical endeavors. I want to thank Dr. Nathan Meredith for helping me launch my first project. Your guidance shaped how I thought about paper devices in a light that has helped progress my future work. I also want to thank Dr. Jaclyn Adkins for allowing me to pick your brain about the fundamentals of paper microfluidics and supporting my habit of going to lunch rather than eating the one I brought. The acknowledgements continue with Dr. Casey Quinn and Dr. Kevin Klunder who I could always count on staying late in the old building and taking time to grab a cold one when the opportunity presented itself. I cannot fail to acknowledge all the help Dr. Robert Channon has been as both a collaborator and friend. You have been a great companion on our trips to the corner shop (when I can understand what you are saying).

Lastly, I want to thank my amazing family and friends for supporting and believing in me the last five years. My journey to this point encompassed many ups and downs, but without you I would not have learned to embrace the struggle and make it to through. Each one of you has been instrumental to any success I may have encountered. Most of all I want to thank my parents, especially you Mom, for always guiding and inspiring me. I could have never done all of this without your unrelenting love and extraordinary work ethic instilled in me.

TABLE OF CONTENTS

CHAPTER 1. MICROFLUIDIC PAPER-BASED ANALYTICAL DEVICES

*These sections have been selected from the *Analytical Chemistry* **2017**, *89*(1), 71 review article for which I was responsible for writing.

CHAPTER 2. DESIGN CONSIDERATIONS FOR REDUCING SAMPLE LOSS IN MICROFLUIDIC PAPER-BASED ANALYTICAL DEVICES*

*This work has been published in *Analytica Chimica Acta* **2018**, *1017*, 20.

CHAPTER 1. MICROFLUIDIC PAPER-BASED ANALYTICAL DEVICES

1.1 Chapter Overview

As humans, we are continually exposed to an insurmountable number of chemicals. In some cases, these chemicals allow us to breathe and in others they may cause irreparable respiratory disease.[1] The concept of the “exposome” encompasses the interactions an individual will have with environmental exposures from the cradle to the grave. Much like the Human Genome Project, where the human genome was successfully mapped, the Human Exposome Project is a large collaboration that aims to identify and understand how these exposures relate to human health.[2] The connection from this large collaboration to my research is to employ analytical chemistry strategies for quantifying different exposures. There are many ways to identify and quantify the chemicals we encounter in our air, water, and soil; however, the focus of my work has been developing inexpensive, portable, and user-friendly paper devices to do so. Using paper as a vessel to perform chemical analysis is not new. The development and use of litmus dates to alchemist Arnaldus de Villa Nova around 1300 AD. Since then, a variety of paper-based devices have been developed.[3] Unfortunately, poor analytical performance of these devices in real-world applications limit their utility. This poor performance may reference the sensitivity (the capacity to measure changes in analyte concentration) or the detection limit (the smallest quantity of an analyte that is significantly different from the blank). Here, poor performance is often the result of interferences in complex mixtures or matrixes. Aiming to identify, understand, and overcome the issues that relate to poor device performance is the focus of my dissertation.

1.2 Need for Point-of-Care Analysis

In 2016, healthcare costs in the United States rose by 4.3% to $3.3 trillion, an increase largely attributable to prolonged time to diagnosis.[4] As a consequence of these increasing healthcare costs, physicians often deny potentially beneficial diagnostics to patients as a method to cut costs.[5] Alongside their high cost, the process for analyzing human biological samples have a long journey from patient to laboratory. After initial retrieval, these samples may need to be stored at –80 °C to avoid degradation, be transported to a centralized laboratory, analyzed by a trained technician with cumbersome instrumentation such as inductively coupled mass spectrometers (ICP-MS), and be communicated to the patient. Unfortunately, this expensive and time-intensive process is how environmental samples are typically analyzed for harmful metal contaminants. As a result, progress updates on monitoring and remediation efforts in places like Flint, MI are slowed. Access to rapid and affordable point-of-need analysis is not just a problem in the United States, it is a problem worldwide. Access to point-of-need analysis in developing countries is scarce due to limited resources.

The key to controlling or even reducing costs, therefore, lies in cheaper, faster, and more accurate diagnoses for environmental monitoring and assessment. Alternatives, however, exist. Traditional microfluidics have proven effective at reducing costs by increasing the portability of diagnostic devices.[6] In addition to increasing portability, groups have demonstrated the ability for microfluidics to separate, sort, and analyze micron-sized particles such as single cells.[7] Further improvements can be achieved using a microfluidic devices made from paper.

1.3 Microfluidic Paper-Based Analytical Devices

1.3.1 Advantages and Limitations of μPADs

Microfluidic paper-based analytical devices (μPADs) have also proven to be cost-effective methods for analysis while remaining disposable, possessing the capacity to store reagents, and producing quantitative diagnostic results.[8] Distinctly, these μPADs self-transport fluids without the need for bulky, external pumps.

Since the first microfluidic paper-based analytical device (μPAD) was introduced by Whitesides and coworkers in 2007, the field has continued to develop at an exponential rate with notable impacts to academic and industrial communities.[9] This growth is illustrated in Figure 1.1 where the sum of times the term "paper-based microfluidics" is published from 1999 to 2018. Generally, μPADs are fabricated from cellulosic paper as a substrate can transport small volumes (0.1 to 100 μL) of liquids using channels with millimeter dimensions. While μPADs may lack the high mechanical robustness of traditional microfluidic materials (i.e., glass,[10] silicon,[11]

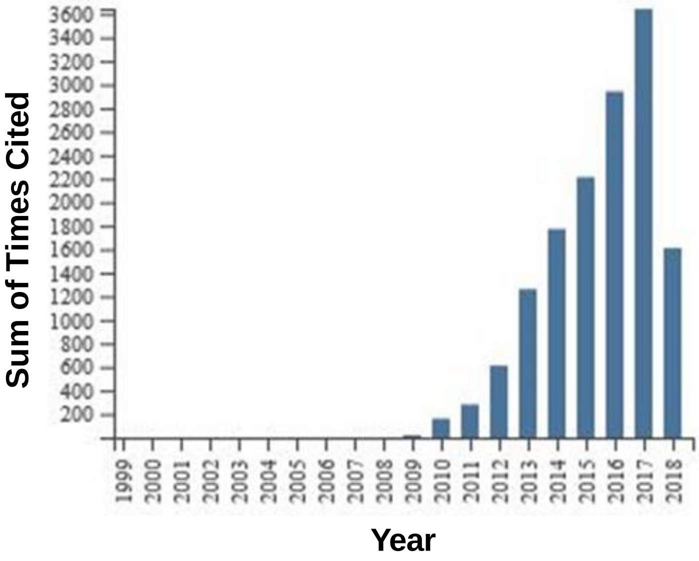

Figure 1.1. Web of Science search for "paper-based microfluidics": accessed 04/21/2018

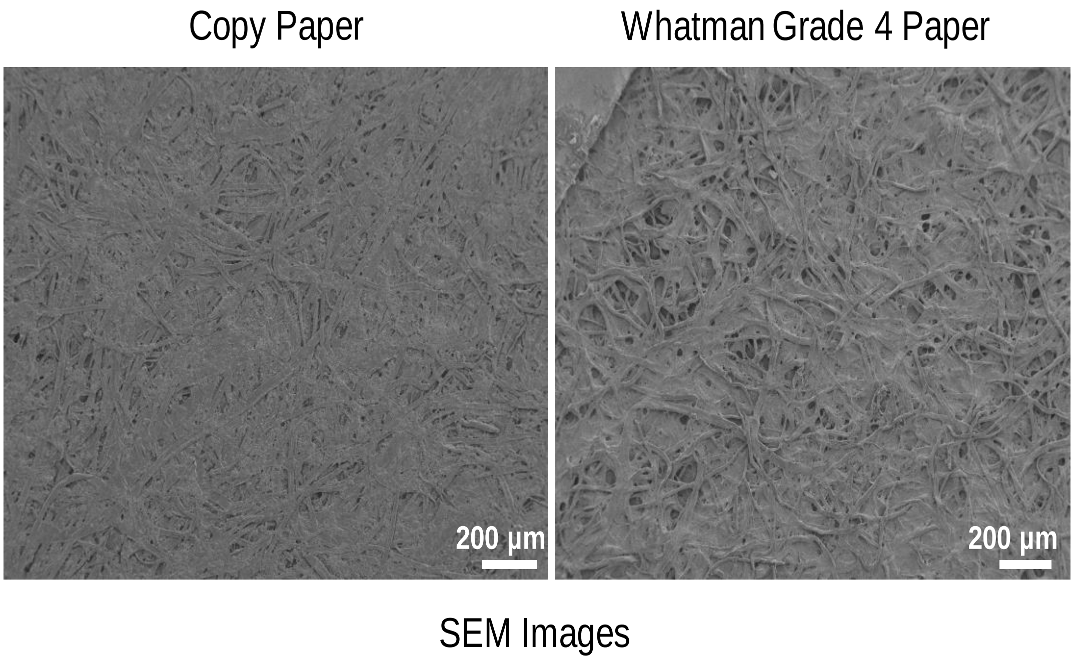

Figure 1.2. Scanning electron microscopy images of copy paper and Whatman Grade 4 Paper.

polymers[12]), they have other advantages.[13] As an abundant, inexpensive, lightweight, and biodegradable material, cellulosic paper is a natural platform for microfluidics. Cellulose is a natural polymer made up of repeating glucose units. The pendant hydroxyl groups of the glucose units make cellulose hydrophilic. In addition to its hydrophilic structure, cellulosic paper is spun into fibers creating a porous network for fluids to be transported. Cellulose's hydrophilicity and porosity thus generate flow via capillary action without the need for external pumps or power

$$\mathrm{L} = \sqrt{\frac{\gamma D t}{4\mu}}$$

L = capillary length
t = time
γ = surface tension
D = capillary diameter
μ = dynamic viscosity

Equation 1.1. The Lucas-Washburn equation that models capillary flow in porous material.

supplies. This capillary flow is also well-modeled by the Lucas-Washburn (LW) equation found in Equation 1.1.[14,15]

What separates µPADs from lateral flow assays (LFAs) is the use of patterning techniques to create well-defined and fluid directing channels. Due to the use of simple fabrication techniques, µPADs are also amenable to roll-to-roll processing techniques which drastically reduce the cost of manufacturing.[16] Application of µPADs is particularly favored in point-of-need settings that require rapid analysis with low-cost and simple operation. While many of these applications are relevant to diagnostics in developing countries where resources and experts are limited, numerous applications exist in the developed world as well. For example, monitoring water quality in the home or in the environment may be of great interest.

The categories of analytes measured on µPADs include health biomarkers (pH, nitrite, glucose, proteins, etc.), metals and inorganic ions (Fe, Ni, Cu, Co, Cd, Cr, Pb, K, etc.),[17] pathogens (bacteria, viruses, etc.)[18] and various organic molecules (amines, nitroaromatics, etc.). These lists are ever increasing as the field continues to grow. The ability to design multiplexed assays, or analyze multiple analytes on a single device, is very powerful for broad spectrum analysis. These advantages have driven growth of the field toward applications of the portable analytical devices for clinical diagnostics, environmental monitoring, and food safety assurance.

Unfortunately, µPADs are also characterized by poor performance metrics. Large sample loss or sample retention are attributed to high limits of detection and low sensitivity.[19,20] Both evaporation and non-specific binding to the cellulose fibers can limit the sample transport that leads to poor analytical performance.[20] Sample preconcentration techniques are often employed to detect analytes of very low concentrations.[21] Additionally, filtration or separation methods may be required to limit interferences that may induce false positive or false negative signals.[18] Both sample preconcentration and pretreatment, however, increase complexity which may induce error when performing the analytical measurement.

Besides poor analytical performance, the scope of analytes available to measure are often limited due to inherent properties of using paper-based devices. µPADs transport fluids very slowly which limits the speed and number of analyses that can be performed. Thus, slow transport of fluids is unfavorable for analytes that are susceptible to fouling or degradation. These devices are also limited in their inability to mobilize large particles due to small pore sizes (11–22 µm).[22] This means analysis of micron-sized particles such as particulate matter, cells, and large bacteria is largely absent in the µPAD literature. In some cases, samples of interest are insoluble in water and require the use of organic solvents. Unfortunately, organic solvents can often dissolve or wet the barriers used to create patterned fluidic channels.

1.3.2 Materials and Fabrication

The material selection and fabrication can largely reduce the impacts of the disadvantages mentioned above. Besides the improvement in analytical performance and scope, core to the novelty of µPADs are their low cost of materials and ease of fabrication. Fabrication methods often

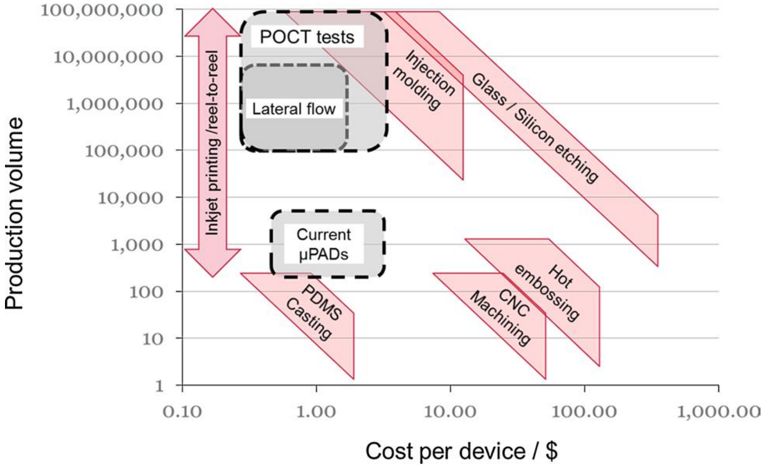

Figure 1.3. Cost and production volume comparison for common lab-on-a-chip fabrication technologies. Reprinted from Jenkins, G.; Wang, Y.; Xie, Y. L.; Wu, Q.; Huang, W.; Wang, L. H.; Yang, X. *Microfluid. Nanofluidics* **2015**, *19*, 251 (ref 16), with permission of Springer.

target lowering the cost per device, increasing production volume, or adding assay functionality. Figure 1.3 shows cost-production volume relationships for a number of different device materials, including several µPAD fabrication methods.[16] A variety of µPAD fabrication methods have been recently reported with emphasis on improving the solvent compatibility, deposition of new reagents and barrier materials, improved designs for flow control, and new architectures and functionalities for new applications. Novel porous materials as well as devices with enhanced properties including resistance to aggressive solutions have been reported.

Wax is the dominant workhorse material for solution barriers in µPADs due to the ease of printing designs using commercially available printers and the hydrophobicity of the barriers that act to channel fluid flow. Once wax is printed on a paper substrate and melted, the wax coats the cellulose fibers creating a hydrophobic barrier. While wax has many advantages, surfactants and organic solvents can wet and dissolve the barriers, resulting in solution penetration over and/or through the wax barrier and a loss of sample to the device. Alternative barrier materials can provide a wider range of chemical compatibility. Jahanshahi *et al.* used a pullulan, a polysaccharide polymer, as a barrier to organic solvents in tandem with wax barriers to fabricate omniphobic devices.[23] To create that device, the combination of a hydrophobic wax and an organic solvent resistant pullulan were patterned in series. Laser direct-writing (LDW) techniques have also been shown to form hydrophobic barriers by polymerizing photopolymer-impregnated filter paper, and this approach has also been applied to fabricate time delay barriers. He *et al.* created delay barriers in filter paper by adjusting the write speed of a laser to control the barrier height, which resulted in the delayed flows of different solutions throughout the device.[24] Figure 1.4A shows a schematic for barrier fabrication and the delay of liquid flow with barriers made with different laser writing speeds. Silanes can also be used to create solvent barriers. Jiang *et al.* showed that hydrophobic paper generated by treatment with octadecyltrichlorsilane (OTS) could be made hydrophilic with a handheld corona generator.[25] By using a PMMA mask, hydrophilic channels were regenerated where the ozone contacted the surface; they even used the corona generator as initiators for single-use turn-on valves. Other silicone barriers such as tetrakis(dimethylsiloxy)silane and 1,3-dimethyltetramethoxysilane were used Rajendra *et al.* to generate barriers showing resistance to aqueous, organic, and surfactant solutions.[26] With simplicity in mind, Sameenoi *et al.*. showed that a one-step screen-printing method for patterning hydrophobic polystyrene could be used to create barriers.[27] In another example of using common hydrophobic materials, Sharpie ink has been shown to work as an alternative to wax. Xu *et al.* showed that the Sharpie ink could be harvested and loaded into cartridges and patterned with an ink jet printer.[28] One disadvantage, noted by Xu *et al*., was that the ethanol solution used in the ink evaporates leading to poor shelf life.[28] Gallibu *et al.* addressed the lifetime concern by coupling Sharpie markers to an XY plotter to draw hydrophobic channels.[29] Other low cost strategies for fabricating µPAD barriers utilized Parafilm in either embossing or photolithography processes.[30] Both of these methods to fabricate hydrophobic channels, i.e., embossing and the photolithography, can be implemented with basic office supplies and laboratory benchtop tools.

Automated inkjet printing methods for deposition of reagents and hydrophobic barriers have become very popular. These printing methods are designed to provide good control of deposition volume (pL to nL), accuracy of defined geometries (±10 µm), and potential for roll-to-roll processing.[31] The use of three-dimensional (3D) printers has also grown recently.[31b, 32] Asano *et al.* printed both hydrophilic channels and hydrophobic barriers in conjunction with a patterned photomask.[31b] They succeeded by first impregnating chromatography paper with octadecyltrichlorosilane in n-hexane, leaving a hydrophobic surface once dried. They followed the

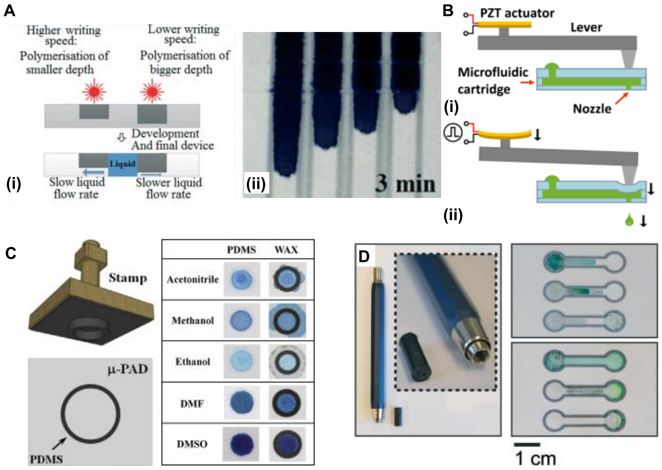

Figure 1.4. (A) (i) Variable depth inside the paper substrate, created using pulsed laser exposure (ii) delay of liquid flow after the introduction of blue ink in fluidic channels with barriers created using different speeds. Reproduced from He, P. J. W.; Katis, I. N.; Eason, R. W.; Sones, C. L. *Lab Chip* **2015**, *15*, 4054 (ref 24), with permission of The Royal Society of Chemistry. (B) (i) and (ii) represent the printing states before and after mechanical loads from the piezoelectric actuator. Reprinted from Li, B. Q.; Fan, J. Z.; Li, J. N.; Chu, J. R.; Pan, T. R. *Biomicrofluidics* **2015**, *9*, 11 (ref 31), with the permission from AIP Publishing. (C) Stamp with geometry of hydrophobic PDMS barrier along with images of side-by-side comparison showing compatibility of PDMS barriers and wax barriers with some organic solvents. Reprinted from Dornelas, K. L.; Dossi, N.; Piccin, E *Anal. Chim. Acta.* **2015,** *858*, 82 (ref 34), with permission from Elsevier. (D) Reagent pencil with image when water is added to the sample zone of devices, it dissolves the reagents from the pencil traces and transports them into the test zone (top); the final appearance of the reagents in the test zone. Reproduced from Mitchell, H. T.; Noxon, I. C.; Chaplan, C. A.; Carlton, S. J.; Liu, C. H.; Ganaja, K. A.; Martinez, N. W.; Immoos, C. E.; Costanzo, P. J.; Martinez, A. W. *Lab Chip* **2015**, *15*, 2213 (ref 36), with permission from The Royal Society of Chemistry.

deposition step by irradiating the surface with ultraviolet (UV) light using a photomask to obtain selective regeneration of hydrophilic behavior. An advantage to 3D-printing the photomask is that 100 μm width channels can be fabricated while maintaining sample flux. In other cases, 3D printers were modified to be used as wax printers by Pearce *et al.*[32a]

A challenge with inkjet printing is the risk of contamination when printing multiple inks, which necessitates meticulous cleaning of the cartridges and print heads. To address the contamination issue, Li *et al.*, fabricated a user-friendly custom piezoelectric mechanism that gave controllable deposits with pL to nL volumes.[31a] Figure 1.4B shows the piezoelectric actuator releasing fluid to the substrate. This cost-friendly method utilized a unique cartridge-nozzle system that reduced the risk of contamination by keeping the reagents from contacting the piezoelectric actuator and the cartridge. Advantages to using high-performance reagent printing methods such as the Dimatix DMP-3000 were demonstrated by Jenkins *et al.* using flow-ready polydimethylsilonxane (PDMS) channels with widths of 60 µm.[16] The narrow channel width showed promise for smaller sample volume applications where analytes may be difficult to obtain or in low abundance. Jenkins *et al.* notes that this method may be advantageous for high-volume roll-to-roll processing methods previously described.[33] A simple PDMS printed channel alternative was shown by Dornelas *et al.* using stamps to fabricate hydrophobic barriers that also showed good chemical compatibility with water, organic solvents (i.e., acetonitrile, methanol, ethanol, dimethylformamide, and dimethyl sulfoxide), and surfactants (i.e., sodium dodecyl sulfate, cetyltrimethylamnonium bromide, Triton X-100).[34] Figure 1.4C shows an image of the stamp and a comparison of the chemical compatibility between PDMS and wax printed barriers with various organic solvents.

Hand drawn deposition methods have advantages of ease of use and transport in the field. Crayons were previously employed to draw hydrophobic barriers, however, innovations have been realized with custom reagent pencils and pens.[35] Mitchell *et al.* showed that sensitive, biologically relevant reagents could be combined with graphite and pressed into pellets for use in mechanical pencils.[36] As a comparison, a solution deposition method for horseradish peroxidase (HRP) exhibited signals for 3 days while the pencil loaded HRP method showed signal for up to 10 days. Figure 1.4D shows the reagent pencil along with the drawn reagents at the moment when water is added to the device and also after the dissolved sample reaches the detection zone. Oyola-Reynoso *et al.* employed a similar strategy but with ink pens.[37] Their pens were loaded with a trichloro perfluorosilane/n-hexane ink and used to create hand drawn hydrophobic barriers. Nuchtavorn *et al.* used Sharpie ink and bovine serum albumin (BSA) bio-ink in a similar fashion but with the pend coupled to a Craft cutter to automate the drawing process.[38] Carrasquilla *et al.* showed the feasibility of printing bioinks without the need for hydrophobic barriers.[39] These megadalton-sized long-chain DNA aptamer bioinks were shown to have more effectively print characteristics when applied with a thermal printhead instead of a piezoelectric head.

While μPADs traditionally utilize capillary action to create flow for sample transport, control of that flow is important for temporally dependent transformations such as timed reagent additions; this principle is also relevant for applications such as serial injections and dilutions. Kinahan *et al.* described the use of slowly dissolving films for temporally controlled reagent release on disk devices.[40] Alkyl ketene dimer (AKD) is known to establish hydrophobic barriers. Salentijn *et al.* showed this, as well as subsequent regeneration of hydrophilic behavior in the paper after oxygen plasma treatment.[41] The level of hydrophobicity could be controlled through AKD loading in the paper. Additionally, the AKD deposition could be manipulated to form gates that were impermeable to aqueous solutions but successfully wetted after the addition of alcohol to the mixture. Songok *et al.* showed that the use of converging and diverging channel geometries provided control over flow rate, and enabled longer duration flows.[42] Toley *et al.* programmed 3D μPADs to automatically control turn-on valves through use of swellable sponge-like materials.[43] Figure 1.5A shows the turn-on action of the valve due to swelling of channel A and the connection made with channel B. Thermally activated release of sample from sponge-like materials was demonstrated by Niedl *et al.*[44] Using hydrogels such as N-isopropylacrylamide 97% (NIPAM), they controlled the release of sample to a paper device. These hydrogels have the ability to swell to 85 wt%, however, the material does not release the liquid when in contact with the paper at room temperature. At any temperature above 30 °C, though, the hydrogel dispensed the entire sample. In contrast, acrylamide (AcAM) hydrogels will release known fractions of the sample volume, in a manner that varies linearly with temperature over the range from 30 to 60 °C. Figure 1.5B shows the release of fluid with NIPAM and NIPAM-AcAm at different temperatures. Akyazi *et al.* lowered the flow rate of aqueous samples by employing two different sets of hydrogels. The first was Ionogels 1 (IL-1) and 2 (IL-2) and the second was a mixure of 1-ethyl-3-methylimidazolium ethyl sulfate IL and trihexyltetradecyl-phosphonium dicyanamide IL.[45] Once these ionic gels were drop-cast and UV-photopolymerized, fluid flow rates were measured in straight-channel devices. Both devices loaded with ionogels slowed the flow rate compared to the unmodified device, with the phosphonium gel (IL-2) exhibiting the slowest flow rate.

Traditionally devices are sealed through lamination or packing tape to lower contamination risk as well as to lower effects of humidity and evaporation.[46] However, da Silva *et al.* has shown that new methods of sealing can affect the flow rate; the triboelectric effect was used as a means to electrostatically seal a μPAD between two poly(ethylene terephthalate) (PET) films.[47] The positively and negatively charged PET was generated by rubbing them against polytetrafluoroethylene (PTFE) and poly(methyl methacrylate) (PMMA), respectively. When comparing the flow rates between electrostatically sealed devices and unsealed devices, the charged devices delayed the flow rate as a result of the attraction of the polar water molecules to the charged surfaces. Figure 1.5C shows the tribocharging, tribosealing and the sample's distance traveled up the device.

There are a number of three-dimensional (3D) devices recently published that use the origami construction method to measure analytes.[48] Despite the large flux of these origami devices published with new applications, the scope of this review highlights new fabrication schemes in

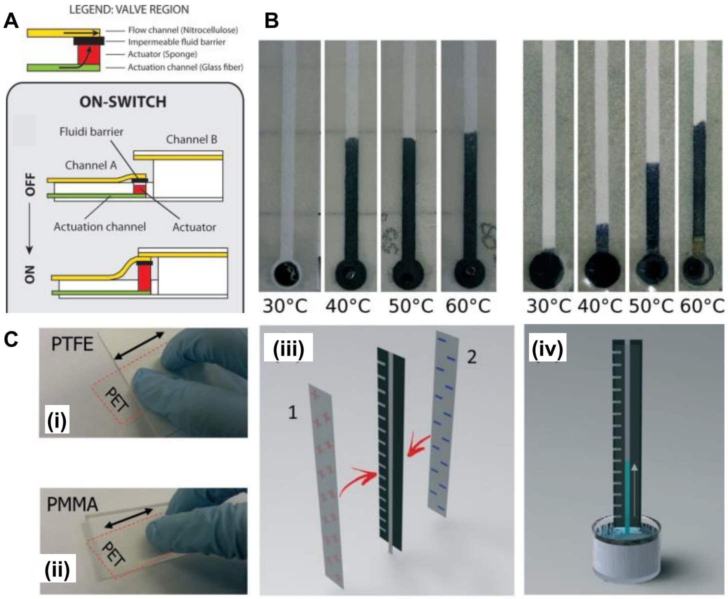

Figure 1.5. (A) Schematic of an on-switch. It consists of two flow channels, A and B, placed at two different levels. Upon actuation, one end of channel A lifts up to connect to one end of channel B. Reproduced from Toley, B. J.; Wang, J. A.; Gupta, M.; Buser, J. R.; Lafleur, L. K.; Lutz, B. R.; Fu, E.; Yager, P. *Lab Chip* **2015**, *15*, 1432-1444 (ref 43), with permission of The Royal Society of Chemistry. (B) Images displaying the switch-like liquid release from a NIPAM hydrogel at different temperatures (left) and images illustrating the gradual linear release of liquid from a composite NIPAM-AcAm hydrogel at different temperatures. Reproduced from Niedl, R. R.; Beta, C. *Lab Chip* **2015**, *15*, 2452-2459 (ref 44), with permission of The Royal Society of Chemistry. (C) Images of the manual tribocharging of PET sheets by rubbing on PTFE (i) and PMMA (ii) surfaces. Schematic representation of the tribosealing process by electrostatic "sandwich type" contact (iii) and the distance traveled by the fluid front inside the paper channel over time. Reproduced from da Silva, E.; Santhiago, M.; de Souza, F. R.; Coltro, W. K. T.; Kubota, L. T. *Lab Chip* **2015**, *15*, 1651-1655 (ref 47), with permission of The Royal Society of Chemistry.

this section; those origami devices will be discussed in following sections. Wang *et al.* have shown a unique greeting card "pop-up" electrochemical paper-based analytical device (ePAD) which can control fluidic and electrical conductivity simply by folding it. When the device is "open", the sample is contained in a reaction zone. Once the reaction is complete and the device is "closed", the reaction zone comes in contact with the detection zone. This 3D device is fabricated from a single sheet of paper and also allows for control of the fluid's path and timing.[49] Another single layer 3D device was fabricated by Jeong *et al.* using double-sided wax printing to create the microfluidic network.[50] The vertical and horizontal channels were fabricated by varying the pattern on either side and then melting the wax and pressing the device with a laminator. This double-sided printing method shows promise for high production volume since the 3D devices can be fabricated in 35.5 s. Another 3D device was developed from Camplisson *et al.* using a two-layer configuration. The two-layer system's wicking rate was found to be significantly increased compared to that of one-layer devices.[51] The flow rates were measured at both 100% and 35% relative humidity and compared with Lucas-Washburn (LW) behavior for both the unsealed one- and two-layer devices. At 100% RH the flow rates of both the single and two-layer devices are accurately predicted by the LW equation. At 35% RH the flow rates in both devices only followed LW behavior for the first 5 minutes. Deviation from predicted behavior was accredited to solvent evaporation, which is not accounted for in the LW equation.

Functional structures such as electrodes have been incorporated into µPADs and have found broad application in addition to chemical analysis (vide infra). Flow rates (distance/time) on paper were historically measured colorimetrically with dyes. Recently, Bathany *et al.* measured the flow rate by incorporating an electrode as an electrochemical sensor for conductive aqueous samples.[52] Here a polycarbonate device was assembled with inlet and outlet reservoirs and a working electrode lying flat between them. When an electrolyte solution was added to the reservoir and a paper strip was added into the outlet, the rate of the fluid wicking up the paper was calculated using the Cottrell equation based on the current being measured. They also investigated the effects on flow rates by treating the device with oxygen plasma and a DEX polymer. Mixing of reagents has also been explored by incorporating a zig-zag channel geometry containing an electrode.[53] The behavior of electrokinetically-driven flow in a zig-zag channel was studied by Dey *et al.* via the mixing of red and blue food coloring.[53] It was shown that mixing was enhanced by controlling the electrokinetically mediated flow. Typically, electrodes with low intrinsic resistance are added to devices to maximize the applied current, but Matsuda *et al.* incorporated more resistive electrodes to take advantage of Joule heating, which aided in controlling temperature sensitive reactions, concentrating the sample on a given zone, as well as creating a stop valve.[54]

1.3.3 Detection Motifs

There are much fewer examples of varying detection motifs compared to the fabrication, however, most µPADs commonly use either of the five following detection schemes: 1) colorimetric, 2) luminescence, 3) electrochemiluminescence, 4) electrochemical, and 5) tandem systems.[46] The first µPADs used semiquantitative colorimetry schemes to validate whether a given analyte was present and perhaps have an idea of a high or low concentration. This colorimetry was further developed as the intensity of a color development could more accurately quantify a concentration for a given analyte. The intensity of a color can be analyzed by eye through a comparison to a reference card, similar to that of a pH test. The intensity of a color can also be analyzed by an image processing program such as ImageJ, following a picture or scanned copy of the device. The later reduces issues such as personal subjectivity, however, this also increases the complexity of the device with the need for a camera and computer to perform the analysis. Phone applications are being developed to do this in an all-in-one platform, reducing the burden of bulkier electronics.[55] In conjunction, small single-board computers such as *Raspberry Pi* sytems, are also being developed for the same reasons, which would reduce cost compared to that of a mobile phone. Recently, distance-based colorimetric detection has been published where the length of a developed color band corresponds to a concentration of an analyte.[56] This read-by-eye detection motif combines the simplicity of the colorimetric test without the need for electronics to reduce subjectivity.

Related to colorimetry, luminescence or fluorescence detection on μPADs have also been employed for their highly sensitive measurements.[39] Here, specific analytes can interact with substrates to cause light emission when excited with a light source. This emission can be measured with low-cost and simple camera phone detectors. Electrochemically generated luminescence or electrochemiluminescence has also been used to lower background emission signals.

Electrochemical techniques were first introduced by Henry *et al.*, for the determination of glucose, lactate, and uric acid.[57] These electrochemical μPADs or ePADs can provide lower limits of detection and more sensitive measurements. Techniques such as voltammetry, amperometry and impedance are more commonly utilized.[58] To perform these measurements, carbon-based and metallic wires electrodes are the traditionally employed for their wide availability and good characterization.[58]

Tandem detection motif systems, or systems that use combinations of the aforementioned sensor techniques exemplify μPADs' design versatility. These systems allow for simpler analysis for perhaps easier detectable analytes and more analytical rigor for difficult to detect or dilute analytes.[5959] Specific analytes may also be better suited for either colorimetric, luminescence, or electrochemical analysis. For example, a bacteria cell may not be electrochemically active and require colorimetric or luminescent detection schemes.

1.4 Conclusions

Bringing chemists, engineers, biologists, and clinicians together has massively grown the field since the seminal publication. As a result, new analytes, designs, and assays have been developed. However, major concerns for the field of paper-microfluidics concerning of poor sensitivity, high detection limits, poor reagent selection, slow analysis, and large particle retention remain. My studies specifically target these major challenges. The original motivations to developing μPADs (i.e. inexpensive, accurate, and practical analytical devices) to improve environmental and disease diagnostics are employed throughout my work. Along with the scientific contributions, the motivation behind this work is to advance these devices beyond the laboratory and towards real-world diagnostics.

REFERENCES

1. Brera, S.; Nicolini, A., Respiratory manifestations due to nickel. *Acta Otorhinolaryngologica Italica* **2005,** *25* (2), 113-115.
2. Wild, C. P., Complementing the Genome with an “Exposome”: The Outstanding Challenge of Environmental Exposure Measurement in Molecular Epidemiology. *Cancer Epidemiology Biomarkers & Prevention* **2005,** *14* (8), 1847-1850.
3. (a) Yetisen, A. K.; Akram, M. S.; Lowe, C. R., Paper-based microfluidic point-of-care diagnostic devices. *Lab on a Chip* **2013,** *13* (12), 2210-2251; (b) Yamada, K.; Shibata, H.; Suzuki, K.; Citterio, D., Toward practical application of paper-based microfluidics for medical diagnostics: state-of-the-art and challenges. *Lab on a Chip* **2017,** *17* (7), 1206-1249; (c) Cunningham, J. C.; DeGregory, P. R.; Crooks, R. M., New Functionalities for Paper-Based Sensors Lead to Simplified User Operation, Lower Limits of Detection, and New Applications. In *Annual Review of Analytical Chemistry, Vol 9*, Bohn, P. W.; Pemberton, J. E., Eds. Annual Reviews: Palo Alto, 2016; Vol. 9, pp 183-202.
4. National Health Expenditure Accounts. https://www.cms.gov/Research-Statistics-Data-and-Systems/Statistics-Trends-and-Reports/NationalHealthExpendData/NationalHealthAccountsHistorical.html.
5. (a) Peter, A. U., Physicians, Thou Shalt Ration: The Necessary Role of Bedside Rationing in Controlling Healthcare Costs. *HealthcarePapers* **2002,** *2* (2), 10-21; (b) Scheunemann, L. P.; White, D. B., The Ethics and Reality of Rationing in Medicine. *Chest* **2011,** *140* (6), 1625-1632.

6. Sackmann, E. K.; Fulton, A. L.; Beebe, D. J., The present and future role of microfluidics in biomedical research. *Nature* **2014,** *507,* 181.

7. (a) Nivedita, N.; Garg, N.; Lee, A. P.; Papautsky, I., A high throughput microfluidic platform for size-selective enrichment of cell populations in tissue and blood samples. *Analyst* **2017,** *142* (14), 2558-2569; (b) Kang, C.-C.; Yamauchi, K. A.; Vlassakis, J.; Sinkala, E.; Duncombe, T. A.; Herr, A. E., Single cell–resolution western blotting. *Nature Protocols* **2016,** *11,* 1508; (c) Nivedita, N.; Ligrani, P.; Papautsky, I., Dean Flow Dynamics in Low-Aspect Ratio Spiral Microchannels. *Scientific Reports* **2017,** *7,* 44072.

8. Yang, Y.; Noviana, E.; Nguyen, M. P.; Geiss, B. J.; Dandy, D. S.; Henry, C. S., Paper-Based Microfluidic Devices: Emerging Themes and Applications. *Analytical Chemistry* **2017,** *89* (1), 71-91.

9. Martinez, A. W.; Phillips, S. T.; Butte, M. J.; Whitesides, G. M., Patterned Paper as a Platform for Inexpensive, Low-Volume, Portable Bioassays. *Angewandte Chemie International Edition* **2007,** *46* (8), 1318-1320.

10. Grover, W. H.; Skelley, A. M.; Liu, C. N.; Lagally, E. T.; Mathies, R. A., Monolithic membrane valves and diaphragm pumps for practical large-scale integration into glass microfluidic devices. *Sensors and Actuators B: Chemical* **2003,** *89* (3), 315-323.

11. Harris, N. R.; Hill, M.; Beeby, S.; Shen, Y.; White, N. M.; Hawkes, J. J.; Coakley, W. T., A silicon microfluidic ultrasonic separator. *Sensors and Actuators B: Chemical* **2003,** *95* (1), 425-434.

12. Becker, H.; Locascio, L. E., Polymer microfluidic devices. *Talanta* **2002,** *56* (2), 267-287.

13. Nge, P. N.; Rogers, C. I.; Woolley, A. T., Advances in Microfluidic Materials, Functions, Integration, and Applications. *Chemical Reviews* **2013,** *113* (4), 2550-2583.

14. Washburn, E. W., The Dynamics of Capillary Flow. *Physical Review* **1921,** *17* (3), 273-283.

15. Kolloid-Gesellschaft, *Colloid and Polymer Science: Kolloid-Zeitschrift & Zeitschrift Für Polymere*. Springer: 1918.

16. Jenkins, G.; Wang, Y.; Xie, Y. L.; Wu, Q.; Huang, W.; Wang, L. H.; Yang, X., Printed electronics integrated with paper-based microfluidics: new methodologies for next-generation health care. *Microfluidics and Nanofluidics* **2015,** *19* (2), 251-261.

17. (a) Mentele, M. M.; Cunningham, J.; Koehler, K.; Volckens, J.; Henry, C. S., Microfluidic Paper-Based Analytical Device for Particulate Metals. *Analytical Chemistry* **2012,** *84* (10), 4474-4480; (b) Gerold, C. T.; Bakker, E.; Henry, C. S., Selective Distance-Based K+ Quantification on Paper-Based Microfluidics. *Analytical Chemistry* **2018**.

18. (a) Srisa-Art, M.; Boehle, K. E.; Geiss, B. J.; Henry, C. S., Highly Sensitive Detection of Salmonella typhimurium Using a Colorimetric Paper-Based Analytical Device Coupled with Immunomagnetic Separation. *Analytical Chemistry* **2018,** *90* (1), 1035-1043; (b) Adkins, J. A.; Boehle, K.; Friend, C.; Chamberlain, B.; Bisha, B.; Henry, C. S., Colorimetric and Electrochemical Bacteria Detection Using Printed Paper- and Transparency-Based Analytic Devices. *Analytical Chemistry* **2017,** *89* (6), 3613-3621.

19. Nguyen, M. P.; Meredith, N. A.; Kelly, S. P.; Henry, C. S., Design Considerations for Reducing Sample Loss in Microfluidic Paper-Based Analytical Devices. *Analytica Chimica Acta* **2018**.

20. Ota, R.; Yamada, K.; Suzuki, K.; Citterio, D., Quantitative evaluation of analyte transport on microfluidic paper-based analytical devices (μPADs). *Analyst* **2018,** *143* (3), 643-653.

21. Meredith, N. A.; Quinn, C.; Cate, D. M.; Reilly, T. H.; Volckens, J.; Henry, C. S., Paper-based analytical devices for environmental analysis. *Analyst* **2016,** *141* (6), 1874-1887.

22. Evans, E.; Gabriel, E. F. M.; Coltro, W. K. T.; Garcia, C. D., Rational Selection of Substrates to Improve Color Intensity and Uniformity on Microfluidic Paper-Based Analytical Devices. *The Analyst* **2014,** *139* (9), 2127-2132.

23. Jahanshahi-Anbuhi, S.; Pennings, K.; Leung, V.; Kannan, B.; Brennan, J. D.; Filipe, C. D. M.; Pelton, R. H., Design Rules for Fluorocarbon-Free Omniphobic Solvent Barriers in Paper-Based Devices. *Acs Applied Materials & Interfaces* **2015,** *7* (45), 25434-25440.

24. He, P. J. W.; Katis, I. N.; Eason, R. W.; Sones, C. L., Engineering fluidic delays in paper-based devices using laser direct-writing. *Lab on a Chip* **2015,** *15* (20), 4054-4061.

25. Jiang, Y.; Hao, Z. X.; He, Q. H.; Chen, H. W., A simple method for fabrication of microfluidic paper-based analytical devices and on-device fluid control with a portable corona generator. *Rsc Advances* **2016,** *6* (4), 2888-2894.

26. Rajendra, V.; Sicard, C.; Brennan, J. D.; Brook, M. A., Printing silicone-based hydrophobic barriers on paper for microfluidic assays using low-cost ink jet printers. *Analyst* **2014,** *139* (24), 6361-6365.

27. Sameenoi, Y.; Nongkai, P. N.; Nouanthavong, S.; Henry, C. S.; Nacapricha, D., One-step polymer screen-printing for microfluidic paper-based analytical device (μPAD) fabrication. *Analyst* **2014,** *139* (24), 6580-6588.

28. Xu, C. X.; Cai, L. F.; Zhong, M. H.; Zheng, S. Y., Low-cost and rapid prototyping of microfluidic paper-based analytical devices by inkjet printing of permanent marker ink. *Rsc Advances* **2015,** *5* (7), 4770-4773.

29. Gallibu, C.; Gallibu, C.; Avoundjian, A.; Gomez, F. A., Easily Fabricated Microfluidic Devices Using Permanent Marker Inks for Enzyme Assays. *Micromachines* **2016,** *7* (1), 7.

30. Yu, L.; Shi, Z. Z., Microfluidic paper-based analytical devices fabricated by low-cost photolithography and embossing of Parafilm (R). *Lab on a Chip* **2015,** *15* (7), 1642-1645.

31. (a) Li, B. Q.; Fan, J. Z.; Li, J. N.; Chu, J. R.; Pan, T. R., Piezoelectric-driven droplet impact printing with an interchangeable microfluidic cartridge. *Biomicrofluidics* **2015,** *9* (5), 11; (b) Asano, H.; Shiraishi, Y., Development of paper-based microfluidic analytical device for iron assay using photomask printed with 3D printer for fabrication of hydrophilic and hydrophobic zones on paper by photolithography. *Analytica Chimica Acta* **2015,** *883*, 55-60.

32. (a) Pearce, J. M.; Anzalone, N. C.; Heldt, C. L., Open-Source Wax RepRap 3-D Printer for Rapid Prototyping Paper-Based Microfluidics. *Jala* **2016,** *21* (4), 510-516; (b) He, Y.; Gao, Q.; Wu, W. B.; Nie, J.; Fu, J. Z., 3D Printed Paper-Based Microfluidic Analytical Devices. *Micromachines* **2016,** *7* (7), 12.

33. Focke, M.; Kosse, D.; Muller, C.; Reinecke, H.; Zengerle, R.; von Stetten, F., Lab-on-a-Foil: microfluidics on thin and flexible films. *Lab on a Chip* **2010,** *10* (11), 1365-1386.

34. Dornelas, K. L.; Dossi, N.; Piccin, E., A simple method for patterning poly(dimethylsiloxane) barriers in paper using contact-printing with low-cost rubber stamps. *Analytica Chimica Acta* **2015,** *858*, 82-90.

35. Zhong, Z. W.; Wang, Z. P.; Huang, G. X. D., Investigation of wax and paper materials for the fabrication of paper-based microfluidic devices. *Microsystem Technologies* **2012,** *18* (5), 649-659.

36. Mitchell, H. T.; Noxon, I. C.; Chaplan, C. A.; Carlton, S. J.; Liu, C. H.; Ganaja, K. A.; Martinez, N. W.; Immoos, C. E.; Costanzo, P. J.; Martinez, A. W., Reagent pencils: a new technique for solvent-free deposition of reagents onto paper-based microfluidic devices. *Lab on a Chip* **2015,** *15* (10), 2213-2220.

37. Oyola-Reynoso, S.; Heim, A. P.; Halbertsma-Black, J.; Zhao, C.; Tevis, I. D.; Ccedil;inar, S.; Cademartiri, R.; Liu, X. Y.; Bloch, J. F.; Thuo, M. M., Draw your assay: Fabrication of low-cost paper-based diagnostic and multi-well test zones by drawing on a paper (Reprinted). *Talanta* **2015,** *145*, 73-77.

38. Nuchtavorn, N.; Macka, M., A novel highly flexible, simple, rapid and low-cost fabrication tool for paper-based microfluidic devices (mu PADs) using technical drawing pens and in-house formulated aqueous inks. *Analytica Chimica Acta* **2016,** *919*, 70-77.

39. Carrasquilla, C.; Little, J. R. L.; Li, Y. F.; Brennan, J. D., Patterned Paper Sensors Printed with Long-Chain DNA Aptamers. *Chemistry-a European Journal* **2015,** *21* (20), 7369-7373.

40. Kinahan, D. J.; Kearney, S. M.; Faneuil, O. P.; Glynn, M. T.; Dimov, N.; Ducree, J., Paper imbibition for timing of multi-step liquid handling protocols on event-triggered centrifugal microfluidic lab-on-a-disc platforms. *Rsc Advances* **2015,** *5* (3), 1818-1826.

41. Salentijn, G. I. J.; Hamidon, N. N.; Verpoorte, E., Solvent-dependent on/off valving using selectively permeable barriers in paper microfluidics. *Lab on a Chip* **2016,** *16* (6), 1013-1021.

42. Songok, J.; Toivakka, M., Controlling capillary-driven surface flow on a paper-based microfluidic channel. *Microfluidics and Nanofluidics* **2016,** *20* (4), 9.

43. Toley, B. J.; Wang, J. A.; Gupta, M.; Buser, J. R.; Lafleur, L. K.; Lutz, B. R.; Fu, E.; Yager, P., A versatile valving toolkit for automating fluidic operations in paper microfluidic devices. *Lab on a Chip* **2015,** *15* (6), 1432-1444.

44. Niedl, R. R.; Beta, C., Hydrogel-driven paper-based microfluidics. *Lab on a Chip* **2015,** *15* (11), 2452-2459.

45. Akyazi, T.; Saez, J.; Elizalde, J.; Benito-Lopez, F., Fluidic flow delay by ionogel passive pumps in microfluidic paper-based analytical devices. *Sensors and Actuators B: Chemical* **2016,** *233*, 402-408.

46. Cate, D. M.; Adkins, J. A.; Mettakoonpitak, J.; Henry, C. S., Recent Developments in Paper-Based Microfluidic Devices. *Analytical Chemistry* **2015,** *87* (1), 19-41.

47. da Silva, E.; Santhiago, M.; de Souza, F. R.; Coltro, W. K. T.; Kubota, L. T., Triboelectric effect as a new strategy for sealing and controlling the flow in paper-based devices. *Lab on a Chip* **2015,** *15* (7), 1651-1655.

48. (a) Jiawang, D.; Bowei, L.; Lingxin, C.; Wei, Q., A Three-Dimensional Origami Paper-Based Device for Potentiometric Biosensing. *Angewandte Chemie* **2016,** *128* (42), 13227-13231; (b) Li, W.; Qian, D.; Wang, Q.; Li, Y.; Bao, N.; Gu, H.; Yu, C., Fully-drawn origami paper analytical device for electrochemical detection of glucose. *Sensors and Actuators B: Chemical* **2016,** *231*, 230-238; (c) Wu, L. D.; Ma, C.; Ge, L.; Kong, Q. K.; Yan, M.; Ge, S. G.; Yu, J. H., Paper-based electrochemiluminescence origami cyto-device for multiple cancer cells detection using porous AuPd alloy as catalytically promoted nanolabels. *Biosensors & Bioelectronics* **2015,** *63*, 450-457; (d) Cunningham, J. C.; Scida, K.; Kogan, M. R.; Wang, B.; Ellington, A. D.; Crooks, R. M., Paper diagnostic device for quantitative

electrochemical detection of ricin at picomolar levels. *Lab on a Chip* **2015,** *15* (18), 3707-3715.

49. Wang, C. C.; Hennek, J. W.; Ainla, A.; Kumar, A. A.; Lan, W. J.; Im, J.; Smith, B. S.; Zhao, M. X.; Whitesides, G. M., A Paper-Based "Pop-up" Electrochemical Device for Analysis of Beta-Hydroxybutyrate. *Analytical Chemistry* **2016,** *88* (12), 6326-6333.
50. Jeong, S. G.; Lee, S. H.; Choi, C. H.; Kim, J.; Lee, C. S., Toward instrument-free digital measurements: a three-dimensional microfluidic device fabricated in a single sheet of paper by double-sided printing and lamination. *Lab on a Chip* **2015,** *15* (4), 1188-1194.
51. Camplisson, C. K.; Schilling, K. M.; Pedrotti, W. L.; Stone, H. A.; Martinez, A. W., Two-ply channels for faster wicking in paper-based microfluidic devices. *Lab on a Chip* **2015,** *15* (23), 4461-4466.
52. Bathany, C.; Han, J. R.; Abi-Samra, K.; Takayama, S.; Cho, Y. K., An electrochemical-sensor system for real-time flow measurements in porous materials. *Biosensors & Bioelectronics* **2015,** *70*, 115-121.
53. Dey, R.; Kar, S.; Joshi, S.; Maiti, T. K.; Chakraborty, S., Ultra-low-cost 'paper-and-pencil' device for electrically controlled micromixing of analytes. *Microfluidics and Nanofluidics* **2015,** *19* (2), 375-383.
54. Matsuda, Y.; Shibayama, S.; Uete, K.; Yamaguchi, H.; Niimi, T., Electric Conductive Pattern Element Fabricated Using Commercial Inkjet Printer for Paper-Based Analytical Devices. *Analytical Chemistry* **2015,** *87* (11), 5762-5765.
55. Jung, Y.; Kim, J.; Awofeso, O.; Kim, H.; Regnier, F.; Bae, E., Smartphone-based colorimetric analysis for detection of saliva alcohol concentration. *Appl. Opt.* **2015,** *54* (31), 9183-9189.

56. Cate, D. M.; Dungchai, W.; Cunningham, J. C.; Volckens, J.; Henry, C. S., Simple, distance-based measurement for paper analytical devices. *Lab on a Chip* **2013,** *13* (12), 2397-2404.

57. Dungchai, W.; Chailapakul, O.; Henry, C. S., Electrochemical Detection for Paper-Based Microfluidics. *Analytical Chemistry* **2009,** *81* (14), 5821-5826.

58. Adkins, J.; Boehle, K.; Henry, C., Electrochemical paper-based microfluidic devices. *Electrophoresis* **2015,** *36* (16), 1811-1824.

59. Apilux, A.; Dungchai, W.; Siangproh, W.; Praphairaksit, N.; Henry, C. S.; Chailapakul, O., Lab-on-Paper with Dual Electrochemical/Colorimetric Detection for Simultaneous Determination of Gold and Iron. *Analytical Chemistry* **2010,** *82* (5), 1727-1732.

CHAPTER 2. DESIGN CONSIDERATIONS FOR REDUCING SAMPLE LOSS IN MICROFLUIDIC PAPER-BASED ANALYTICAL DEVICES

2.1 Chapter Overview

The field of microfluidic paper-based analytic devices (μPADs) is most notably characterized by portable and low-cost analysis, however struggles to achieve the high sensitivity and low detection limits needs required for many environmental applications hinder widespread adoption of this technology. Loss of analyte to the device material represents an important problem impacting sensitivity. Critically, we found that at least 50% of a Ni(II) sample is lost when being transported down a 30 mm paper channel that is representative of structures commonly found in μPADs. In this work, we report simple strategies such as adding a waste zone, a larger detection zone and an elution step to increase device performance. A μPAD combining the best performing functionalities lead to a 78% increase in maximum signal and a 28% increase in sensitivity when transporting Ni(II) samples. Using the same combination μPAD lead to a 94% increase in maximum signal for Mn(II) samples. This work was published in Analytica Chimica Acta.[1] Dr. Nathan A. Meredith helped me start this project by introducing the idea of sample loss to me. Sydney P. Kelly helped test the developed methods with for the Mn(II) assay improvement.

2.2 Introduction

Endeavors such as the Human Exposome Project demonstrate the growing interest in understanding the relationship between chronic exposure to environmental pollutants and changes in human health.[2] To understand complex exposures, efficient and selective methods are needed that can both identify and quantify chemical exposures from a variety of sources. Microfluidic paper-based analytical devices (μPADs) provide a tool that brings this level of analysis from the laboratory to the point-of-need due to their ease of use, portability, and low cost. Interest in μPADs has grown rapidly, and a number of applications have been developed in areas of both biological and environmental interest.[3] μPADs have used electrochemical and colorimetric detection motifs to measure concentration, with electrochemical detection frequently providing improved detection limits relative to colorimetric methods.[4] While the number and variety of applications continue to increase, an understanding of the paper properties that affect sensitivity has lacked. Exploring the properties of paper as well as the interactions of samples and reagents with the cellulose substrate will enable further optimization of μPADs and related sensors.

Flow in μPADS is due to capillary action (imbibition) within the hydrophilic porous network; this flow may be modelled by Darcy's law and the Lucas-Washburn equation as described in multiple articles and reviews.[5] However, Li, et al identified a major limitation of current μPAD research as inefficient sample delivery to the detection zone through a combination of sample retention by the cellulose network and sample evaporation.[6] Due to sample losses during transport, limits of detection (LOD) on μPADs are frequently higher than traditional techniques, and/or larger sample volumes are required to achieve comparable LODs. Recent work has focused on modifying flow rates and enhancing sample delivery by modifying the paper substrate using dissolvable bridges, creating flow channels with polymer films by applying coverings with varying contact angles, varying the channel geometries, and/or selecting substrates with different pore sizes.[7] While these studies have shown improvement, they have neither evaluated the fundamental impacts of the unmodified cellulose on sensitivity and detection limit nor provided simple solutions to aid in addressing this problem.

The work reported here expands on previous studies focusing on reducing sample retention within the cellulose network. To test strategies for reducing sample loss, colorimetric detection was chosen for its simple fabrication and quantification. Using Ni(dmg)$_2$ as a model colorimetric system, sample retention in a lateral flow μPAD was indirectly determined by comparing the intensity of the detection zone against a spot test.[8] The spot test acts as a "zero-loss" test for which the sampling zone and detection zone are the same and there is no channel component for sample loss. Sample loss to the cellulose was also determined by extracting the retained fraction into solution and quantifying with absorbance spectroscopy. The results suggested 50% or more of the initial sample never reaches the detection zone. Thus, the extent of sample retention was investigated as a function of distance of travel, detection zone geometry, the inclusion of a flow-through waste region beyond the detection zone, fiber compression, and addition of a subsequent elution step. These investigations lead to a device optimization, which resulted in a maximum signal increase of 78% and sensitivity increase of 28%.

2.3 Experimental Section

2.3.1 Materials

All of the following commercially available reagents were analytical grade and used as received without further purification: $NiSO_4 \cdot 6H_2O$, dimethylglyoxime (dmg), and 4-(2-pyridylazo)resorcinol (PAR). The 0.1 M dmg solution was made using isopropanol. The $MnCl_2 \cdot H_2O$ and 0.1 M PAR solutions were made with Ultrapure water (18.2 MΩ cm) from a Mill-Q system (Merck Millipore Darmstadt, Germany) and used throughout. Whatman Grade 4 Qualitative (W4Qual) filter paper was purchased from GE Healthcare Life Sciences. Scotch^{TM} heavy duty packing tape and 3 mil Scotch^{TM} thermal lamination pouches sealed devices. The 0.1 M borate buffer was made using sodium tetraborate (pH 9.35).

2.3.2 Equipment

CorelDraw X4 was used for device design and the devices were printed on a Xerox ColorQube 8870 wax printer. A Xerox DocuMate 3220 was used to scan the devices prior to image analysis. ImageJ 1.49 was used to analyze the red intensity of the Ni(dmg)$_2$ complex. An Agilent 8453 UV-visible spectrophotometer was used for absorption measurements of Ni(PAR)$_2$ and Mn(PAR)$_2$. A Sartorius PR-50 pH meter with a PY-P28-2S electrode was used for all pH measurements and calibrated daily prior to use. A 30W CO$_2$ Epilog Laser Engraver was used to fabricate the wax-free devices. An Apache AL 13P thermal laminator was used to seal devices in lamination pouches.

2.3.3 Device Designs

Devices were constructed by first cutting the Whatman paper into 8.5" x 11" sheets to fit them into the printer. A "Sky Blue" (R = 0, G = 124, B = 195) colored wax was used for the barriers to provide good contrast to the red-pink colored Ni(dmg)$_2$ complex. The diameter of the sample and detection zones for the standard device were 5 mm and the channel was 2.5 mm wide. From one end to another, the device was 30 mm long. Some devices have black rings printed around the detection zone to help with data acquisition. These printed rings helped align the image analysis tool with a regular size and position. After devices were wax printed, the wax was melted at 150°C into the fibers to create a hydrophobic barrier. An aluminum plate was placed over the device during heating to uniformly distribute pressure and heat. After melting, the bottom layer of the devices was sealed with Scotch^{TM} Heavy Duty packing tape to prevent leaking. A portion of 0.5 μL borate buffer was first pipetted to the detection region and allowed to dry prior to adding 1 μL of the dmg ligand dissolved in isopropanol. Once the reagents were completely dry (~15 min), devices were ready for sample addition (Figure S2.1). Laser cut, wax-free devices were also made for comparison. The dimensions of laser cut devices were the same as the melted wax devices. For laser cut devices, a filter paper sheet with packing tape on the back was used so that an array of devices was created using only the edge of the device as a barrier. This method provided a leak-free barrier for the volumes used. All reagent depositions were identical to those for the wax devices. Laminated devices followed the same procedure as the other devices but after the buffer and ligand deposition, the device was placed in a 3 mil thermal lamination sheet and melted with two passes into a laminator at 350 °F. Then the sampling zone was punched out with a hole-punch and re-sealed on the back with packing tape. To carry-out the extraction in Section 3.3, the detection zone was cut off a used device and the remainder of the device (sampling zone and channel) was placed in 4 mL of deionized water for 24 hrs to extract residual Ni(II). The resulting Ni(II) sample was analyzed by using PAR as the colorimetric indicator.

2.3.4 Image Analysis

Image analysis was done using ImageJ following the procedure of Mentele et al.[9] Instead of using the 8-bit grey scale, the green color space was used. This was achieved by splitting the color channels (“Image” → “Color” → “Split Channels”) and using the “green” channel data. After the image was processed, the “oval” tool was used to select the image data for the detection zone area. In some devices, a circular black line was added to the device to aid the oval placement and improve the consistency of the image analysis. The “Raw Integrated Density” values were divided by 1×10^5 and used for the intensities in this work.

2.3.5 Data Analysis Procedure

To best quantify sample loss, units of moles were monitored versus signal intensity. When comparing the effectiveness of the various device designs, a comparison of the percent differences in maximum signal between 0–1.5 μmol Ni(II) were made. All reported values of maximum signal were statistically significant compared to the standard channel test as determined using a two-tailed sample T-test. The changes in sensitivity of each device was monitored by comparing the percent differences in the slopes of the intensities between 0–0.12 μmol Ni(II) (0, 0.05, 0.06, 0.07, 0.12 μmol). The percent differences in the slope were found to be statistically significant as determined from the error in the slope unless otherwise stated.

2.4 Results & Discussion

2.4.1. "Zero-loss" and Standard Test

Most μPADs use channels to transport sample; however, the extent of sample loss due to transport is poorly understood. Sample loss to paper substrates is potentially complex, thus the first test focused on understanding the amount of sample retention in the transport channel. A comparison of intensities for a zero-loss (spot test) and a channel (standard) device was evaluated for a 12.5 μL aliquot of nine Ni(II) concentrations (0 – 0.12 M). Images of the spot test and standard channel devices are shown in Figure 2.1a. For consistency, the channel device had the same diameter detection zone as the spot test but incorporated a 30 mm long channel. The $Ni(dmg)_2$ intensity in the detection zones was analyzed 1 hr after the Ni(II) sample was added. The spot test data (n = 6) showed a steep increase in signal with increasing Ni(II) concentration, reaching saturation near 1.3 times excess Ni(II) to dmg (stoichiometric equivalence between 0.078 & 0.125 μmol on Figure 2.1a). The channel device data (n = 5) does not show saturation until 15 times excess of Ni(II) (Figure 2.1a). The data suggests the channel is responsible for retaining >50% of the Ni(II) below 0.15 μmol. Next, we explored potential modes of sample retention (wax barrier, inlet, channel length, etc.) aimed to understand and minimize sample loss.

2.4.2 Wax Barrier

To direct flow, wax printed barriers are commonly used to create channel barriers.[10] Despite being hydrophobic, wax barriers are still porous networks and provide potential modes for sample retention. The wax barrier was investigated as a mechanism for retaining sample. When removing the wax barrier (laser cut devices, n = 4), there was a 20% decrease in maximum signal and a 15% decrease in sensitivity (Figure 2.1a). The wax barrier thus improved sample delivery to the detection zone. The sample speed through the laser cut devices was noticeably faster when compared to their wax counterparts. Flow rate has been shown to decrease with the addition of wax barriers but also results in an increased signal intensity for colorimetric detection schemes.[11] With the differences in flow rate between wax printed and laser cut devices, the speed rather than the porous wax barriers appears to affect the device performance.

2.4.3 Channel Retention

As observed in the spot test versus standard channel studies, most of the sample is not measured by the standard channel device. Having examined the effect of the paper channel on the intensity of the deposited sample, a test of how cellulose retained metals was of great interest. Cellulose has been reported to have a weak affinity for metals.[12] To test the strength of these Ni–cellulose interactions in a μPAD format, the detection zone of a used device was placed in 4 mL of deionized water to extract residual Ni(II). The resulting Ni(II) sample was analyzed using PAR as the colorimetric indicator. A plot of the theoretical amount of sample versus the detected amount sample is shown in Figure 2.1b. The values obtained from the UV-vis measurements reflect how much Ni(II) is lost to the device. Between 0-0.6 μmol, up to 50% of the sample does not reach the detection zone. Despite cellulose's β-ᴅ-glucose repeating units having low affinity (0–0.955 mmol metal g^{-1} cellulose) for metals, this study confirmed there is enough affinity between the cellulose network and the Ni(II) that sample is retained in the channel even after soaking in water overnight.[12-13]

2.4.4. *Water Elution*

When most analytes are added to µPADs for colorimetric detection, there is no ancillary treatment to increase the analyte transport, leaving significant analyte in the transport channel undetected. It has previously been reported that a washing step can help eliminate unbound antigen and antibody from µPADs.[14] Our next experiment evaluated the effectiveness of a similar elution step aimed to transport channel-retained sample to the detection zone. To do this, a second elution of water was added to the sample inlet of the device after the original Ni(II) reached the detection zone and dried (~15 min). The Ni(dmg)$_2$ intensities were compared before and after washing (Figure 2.1c). The washing method was effective at moving more sample to the detection zone,

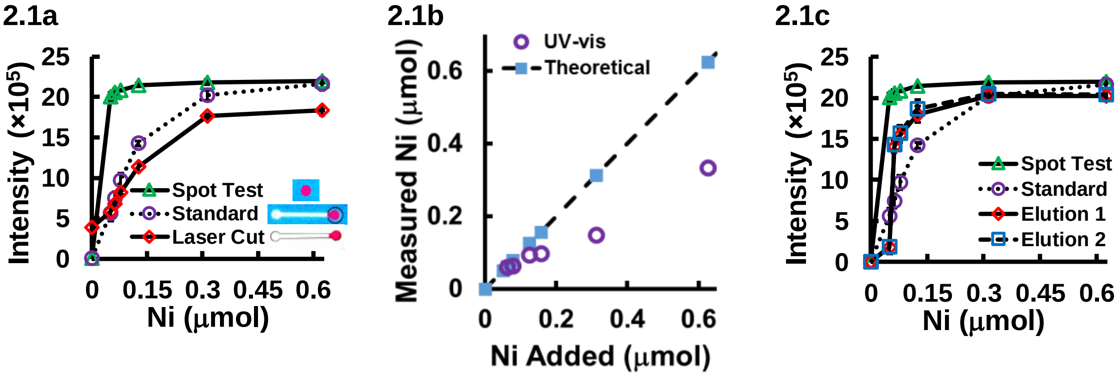

Figure 2.1a. Plot showing intensity of the spot test and the standard channel device versus the laser cut device. Images of these devices are placed in the plot for visualization (inset: devices are shown to right of the legend, respectively). **Figure 2.1b.** The open circle data set shows the number of moles of Ni(II) detected through UV-vis. The closed diamond data set shows the actual amount of moles of Ni(II) deposited on the device. **Figure 2.1c.** Comparison of the elution steps after a standard sampling.

leading to an increase in sensitivity of 8% despite a decrease of 7% in the maximum signal (n = 5). Here the sensitivity difference with the washing step is not statistically significant however the step is efficient at increasing the sensitivity in Section 3.10. A possible rationale for this increase in performance is that once the front of the solution front reaches the detection zone, there is no longer a driving force (or capillary action) to keep sample traveling toward the detection zone. There may be a slight increase of sample transport by diffusion when the whole channel is wet, however, due to evaporation issues in μPADs, this effect is minimal at best.

2.4.5 Distance

Distance is believed to be an important consideration when designing devices due to issues of evaporation hindering sample transport and the ability of the cellulose network to retain the analyte. The distance between the detection and sampling zones was thusly studied. A device was fabricated where the distance between the detection and sampling zones was varied from 11 to 44 mm (Figure 2.2a). The further the detection zone is from the sampling zone, the lower the Ni(II) intensity (n = 3), which is not surprising given prior results as shown in Figure 2.2b. This also parallels the observations outlined in Section 3.1

2.4.6 Sampling Zone

Based on initial results indicating retention of metals by the paper substrate, the impact of inlet geometry on signal was tested. The shape of the sampling zone was varied from the traditional circular zone to a simple rounded tip (small inlet) the width of the microfluidic channel (Figure S2.3). When the circular inlet was replaced with the small inlet, the speed at which the sample flowed greatly increased, reducing overall assay time. The faster assay resulted in a decrease of maximum signal by 4% with no statistically significant increase sensitivity (n = 5). Despite the

2.2a

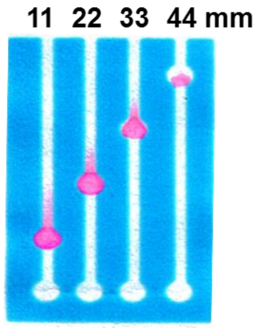

2.2b

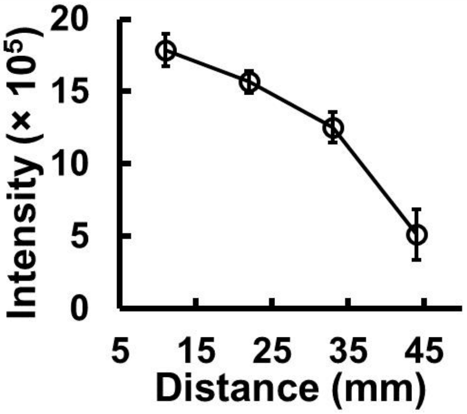

Figure 2.2a. Device showing distance dependence on signal of Ni(dmg)$_2$.

Figure 2.2b. Plot showing the effect of distance on the sample intensity of Ni(dmg)$_2$ at 3.25 mM Ni(II).

small decrease in signal as a result of the geometry change in the sample inlet, increasing the speed of the sample delivery was a successful outcome with regards to decreasing analysis time.

2.4.7 Detection Zone

While it is likely much of the unmeasured Ni(II) remains in the channel, it is also possible that sample complexed by dmg under the paper surface is not detected. If true, then increasing the surface area of the detection zone would increase the measured intensity per μmol of Ni(II). To test this hypothesis, the detection zone area was increased two-fold while the same volume and concentration of buffer and ligand added to the device. To fully cover the detection zone, dmg was deposited onto the device so that the edge of the reagent evaporated at the interface between the channel and the detection zone. By doubling the size of the detection zone, the maximum signal was increased by 63% and the sensitivity increased by 21% (Figure 2.3a, n = 5). By far, this manipulation had the highest increase in both performance metrics. Some bleeding of the red colored complex outside of the distinct red circle was observed with the larger zone. Future experiments using thinner paper could address this problem. We suspect that with thinner paper, there would be more exposed surface area relative to the total volume, resulting a higher signal.

2.4.8 Waste Zone

In the distance dependence study, it was observed that some Ni(dmg)$_2$ complex passed out of the detection zone as there was no barrier stopping sample flow. This raised the question whether adding a “waste zone” at the end of the device would help increase sample wicking to the detection zone. It has been previously shown by Mendez et al that incorporating a 270° hemisphere fan to the end of a microfluidic channel can be used to generate a constant flow rate once the sample reaches the fan.[15] Adding the fan increased the maximum signal by 15% and the sensitivity by 10% (Figure 2.3b). The waste zone functionality proved to be successful at allowing more sample to reach the detection zone. There was a small amount of bleeding of the Ni(dmg)$_2$ complex in the channel past the detection zone but since the complex is insoluble in water, this bleeding was not extensive.

2.4.9 Mechanical Compression

Lastly, pre-swelling and lamination of the devices were explored. The pre-swelled devices were soaked in water and allowed to dry before use. The purpose for swelling the fibers was to create smaller channels and mimic conditions where devices are pre-wetted during fabrication or use. It is believed that the lamination mechanically compresses the pores in addition to reducing evaporation. Through the pre-wetting step, the maximum signal is increased by 7% but the sensitivity difference was not statistically significant (n = 5). Lamination of the device increased signal by 29% but the sensitivity decreased by 7% (Figure 2.3c, n = 5). Generally, the manipulations that exhibited higher maximum signals exhibited higher sensitivity values. However, for the pre-swelled and laminated devices, lower sensitivities and higher maximum signals were observed. Due to the data trends for both manipulations being quite similar, it is believed that both manipulations provide some compression resulting in smaller pores. Surface area measurements (BET) analysis of cellulose show that water can swell fibers by 61%, creating pores with smaller diameters.[16] This compression of the pores may also provide unique pathways for the fluid to travel as the swelling process irreversibly eliminates the cellulose supramolecular structure.[17] Mechanical energy associated with lamination can also cause for the degradation of the cellulose supramolecular structure by disrupting its fibrillar architecture.[18] This collapsing of the supramolecular structure in both manipulations ultimately leads us to pursue the idea that a collapse the of the cellulose supramolecular structure causes the unique behavior. Fidale et al has shown the effects of swelling of fibers in various aprotic and protic solvents if one wanted to tune the substrate to exploit this phenomenon.[19] Further studies are underway to understand the specific factors associated with pre-wetting and laminating that impact sample delivery.

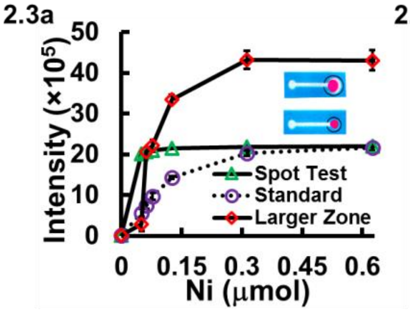

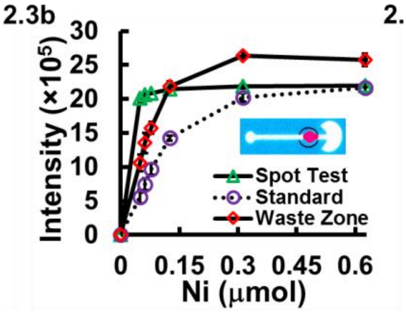

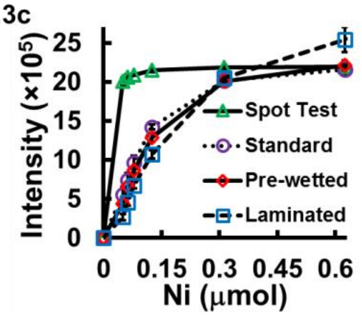

Figure 2.3a. Comparison between the standard channel and the larger zone modified test (inset: devices are shown above the legend, with the larger zone device above the standard). **Figure 2.3b.** Comparison of standard channel to the waste zone modified device (inset: device is shown above the legend). **Figure 2.3c.** The comparison of the standard test versus one that was pre-wetted with Millipore water and the laminated device.

2.4.10 Additive Device

Based on prior results, a device was fabricated combining the manipulations (small inlet, larger detection zone, waste zone and an elution step) that increased the sensitivity and maximum signal. This additive device resulted in an increase in signal and sensitivity of 73% and 23%, respectively for the resulting device. After the elution of water in this device, the maximum signal and sensitivity increased to 78% and 28%, respectively (Figure 2.4, n = 4). As opposed to what was observed in Section 2.4, the elution step increases both the maximum signal and sensitivity to statistically significant values. Indeed, the combination of these manipulations was effective in significantly increasing the device performance.

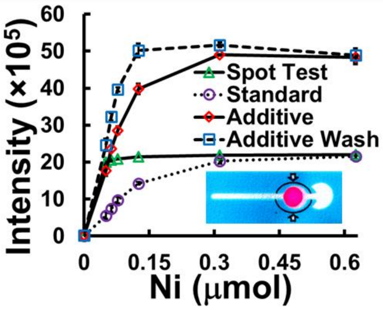

Figure 2.4. The comparison of the standard test versus the additive test along with its washing (inset: device is shown below legend).

2.4.11 Mn(PAR)$_2$

To show these concepts were not unique to the Ni(II)-dmg chemistry, Mn(II) was measured with PAR as the colorimetric ligand. Unlike Ni(dmg)$_2$, the Mn(PAR)$_2$ complex is not a precipitation product under aqueous conditions which provides for variation in the nature of the colorimetric reaction. A comparison of the results for the standard device and the additive device are shown in Figure S2.4. The combination device increased the maximum signal by 94%. The sensitivity was not calculated due to the very high increase in signal at the amounts of Mn(II) used. This test

Table 2.1. Tabulated comparison of maximum signal and sensitivity between devices.

Device	Maximum Signal (Intensity × 10^5)	Sensitivity (Intensity × 10^5 μmol^{-1})
Spot Test	22.0 ± 0.3	---
Standard	22.8 ± 0.6	115
Laser Cut	18.5 ± 0.2	60.8
Elution Step	21.2 ± 0.5	164
Small Inlet	21.8 ± 0.3	117
Larger Detection Zone	43.9 ± 1.5	285
Waste Zone	26.4 ± 0.4	176
Pre-wetted	24.6 ± 1.3	105
Laminated	30.6 ± 2.4	88
Additive	49.0 ± 0.2	320
Additive + Wash	51.7 ± 0.6	407

provides more evidence that the additive device allows for more sample to travel to the detection zone and be detected by reflectance but in a different system.

2.5 Conclusions

As the field of fast and cost-effective sensors grows, it is important to consider simple concepts to lower detection limits and increase dynamic range. The intricate cellulose network commonly used in μPADs provides many torturous avenues for sample retention resulting in poor detection limits and low sensitivity. This study investigated varying travel distances, wax barriers, shape of both detection and sampling zones, pre-swelling fibers, lamination, waste zones and washing steps to compare against the standard and spot test devices. By selecting and combining the manipulations that increased performance of the device, we increased both the maximum signal and sensitivity by 78% and 28%, respectively. Significant performance enhancement was also observed when moving to the detection of Mn(II) with PAR. While this study was aimed at reducing metal sample loss to the μPAD, the retention of varying sample types to the device can be reduced by employing these modifications and principles. The significance of this work may also translate to ePAD technology by increasing the concentration of analytes on the surface of the electrodes. One may imagine that in a stripping voltammetry detection scheme where the detection method relies on efficient sample delivery to the surface of the electrode, these principles may also apply. Not tested here was an experiment aimed to improve sample delivery of biological samples, however this is likely the focus of future work.

REFERENCES

1. Nguyen, M. P.; Meredith, N. A.; Kelly, S. P.; Henry, C. S., Design considerations for reducing sample loss in microfluidic paper-based analytical devices. *Analytica Chimica Acta* **2018,** *1017*, 20-25.
2. Wild, C. P., Complementing the Genome with an "Exposome": The Outstanding Challenge of Environmental Exposure Measurement in Molecular Epidemiology. *Cancer Epidemiology Biomarkers & Prevention* **2005,** *14* (8), 1847-1850.
3. (a) Liana, D. D.; Raguse, B.; Gooding, J. J.; Chow, E., Recent Advances in Paper-Based Sensors. *Sensors* **2012,** *12* (9), 11505; (b) Yetisen, A. K.; Akram, M. S.; Lowe, C. R., Paper-based microfluidic point-of-care diagnostic devices. *Lab on a Chip* **2013,** *13* (12), 2210-2251; (c) Cate, D. M.; Adkins, J. A.; Mettakoonpitak, J.; Henry, C. S., Recent Developments in Paper-Based Microfluidic Devices. *Analytical Chemistry* **2015,** *87* (1), 19-41; (d) Adkins, J.; Boehle, K.; Henry, C., Electrochemical paper-based microfluidic devices. *Electrophoresis* **2015,** *36* (16), 1811-1824; (e) Xia, Y. Y.; Si, J.; Li, Z. Y., Fabrication techniques for microfluidic paper-based analytical devices and their applications for biological testing: A review. *Biosensors & Bioelectronics* **2016,** *77*, 774-789; (f) Meredith, N. A.; Quinn, C.; Cate, D. M.; Reilly, T. H.; Volckens, J.; Henry, C. S., Paper-based analytical devices for environmental analysis. *Analyst* **2016,** *141* (6), 1874-1887; (g) Busa, L.; Mohammadi, S.; Maeki, M.; Ishida, A.; Tani, H.; Tokeshi, M., Advances in Microfluidic Paper-Based Analytical Devices for Food and Water Analysis. *Micromachines* **2016,** *7* (5), 86; (h) Lin, Y.; Gritsenko, D.; Feng, S.; Teh, Y. C.; Lu, X.;

Xu, J., Detection of heavy metal by paper-based microfluidics. *Biosensors and Bioelectronics* **2016,** *83*, 256-266.

4. Dungchai, W.; Chailapakul, O.; Henry, C. S., Electrochemical Detection for Paper-Based Microfluidics. *Analytical Chemistry* **2009,** *81* (14), 5821-5826.
5. (a) Kauffman, P.; Fu, E.; Lutz, B.; Yager, P., Visualization and measurement of flow in two-dimensional paper networks. *Lab on a Chip* **2010,** *10* (19), 2614-2617; (b) Fu, E.; Ramsey, S. A.; Kauffman, P.; Lutz, B.; Yager, P., Transport in two-dimensional paper networks. *Microfluidics and Nanofluidics* **2011,** *10* (1), 29-35; (c) Kim, J.; Kim, H.-Y., On the dynamics of capillary imbibition. *Journal of Mechanical Science and Technology* **2012,** *26* (12), 3795-3801.
6. Li, X.; Ballerini, D. R.; Shen, W., A perspective on paper-based microfluidics: Current status and future trends. *Biomicrofluidics* **2012,** *6* (1), 011301-011301-13.
7. (a) Xu, Y.; Enomae, T., Paper substrate modification for rapid capillary flow in microfluidic paper-based analytical devices. *RSC Advances* **2014,** *4* (25), 12867-12872; (b) Songok, J.; Toivakka, M., Controlling capillary-driven surface flow on a paper-based microfluidic channel. *Microfluidics and Nanofluidics* **2016,** *20* (4), 9; (c) Houghtaling, J.; Liang, T.; Thiessen, G.; Fu, E., Dissolvable Bridges for Manipulating Fluid Volumes in Paper Networks. *Analytical Chemistry* **2013,** *85* (23), 11201-11204; (d) Jahanshahi-Anbuhi, S.; Chavan, P.; Sicard, C.; Leung, V.; Hossain, S. M. Z.; Pelton, R.; Brennan, J. D.; Filipe, C. D. M., Creating fast flow channels in paper fluidic devices to control timing of sequential reactions. *Lab on a Chip* **2012,** *12* (23), 5079-5085; (e) Elizalde, E.; Urteaga, R.; Berli, C. L. A., Rational design of capillary-driven flows for paper-based microfluidics. *Lab on a Chip* **2015,** *15* (10), 2173-2180; (f) Evans, E.; Gabriel, E. F. M.; Coltro, W. K.

T.; Garcia, C. D., Rational Selection of Substrates to Improve Color Intensity and Uniformity on Microfluidic Paper-Based Analytical Devices. *The Analyst* **2014,** *139* (9), 2127-2132.

8. Booth, E.; Strickland, J. D. H., The Compounds Formed between Nickel(II) and Dimethylglyoxime by Alkaline Oxidation. *Journal of the American Chemical Society* **1953,** *75* (12), 3017-3019.
9. Mentele, M. M.; Cunningham, J.; Koehler, K.; Volckens, J.; Henry, C. S., Microfluidic Paper-Based Analytical Device for Particulate Metals. *Analytical Chemistry* **2012,** *84* (10), 4474-4480.
10. Carrilho, E.; Martinez, A. W.; Whitesides, G. M., Understanding Wax Printing: A Simple Micropatterning Process for Paper-Based Microfluidics. *Analytical Chemistry* **2009,** *81* (16), 7091-7095.
11. Hong, S.; Kim, W., Dynamics of water imbibition through paper channels with wax boundaries. *Microfluidics and Nanofluidics* **2015,** *19* (4), 845-853.
12. Zhou, D.; Zhang, L.; Zhou, J.; Guo, S., Cellulose/chitin beads for adsorption of heavy metals in aqueous solution. *Water Research* **2004,** *38* (11), 2643-2650.
13. d'Halluin, M.; Rull-Barrull, J.; Bretel, G.; Labrugère, C.; Le Grognec, E.; Felpin, F.-X., Chemically Modified Cellulose Filter Paper for Heavy Metal Remediation in Water. *ACS Sustainable Chemistry & Engineering* **2017**.
14. Mohammadi, S.; Busa, L. S. A.; Maeki, M.; Mohamadi, R. M.; Ishida, A.; Tani, H.; Tokeshi, M., Novel concept of washing for microfluidic paper-based analytical devices based on capillary force of paper substrates. *Analytical and Bioanalytical Chemistry* **2016,** *408* (27), 7559-7563.

15. (a) Mendez, S.; Fenton, E. M.; Gallegos, G. R.; Petsev, D. N.; Sibbett, S. S.; Stone, H. A.; Zhang, Y.; López, G. P., Imbibition in Porous Membranes of Complex Shape: Quasi-stationary Flow in Thin Rectangular Segments. *Langmuir* **2010,** *26* (2), 1380-1385; (b) Adkins, J. A.; Noviana, E.; Henry, C. S., Development of a Quasi-Steady Flow Electrochemical Paper-Based Analytical Device. *Analytical Chemistry* **2016,** *88* (21), 10639-10647.

16. El Seoud, O. A.; Fidale, L. C.; Ruiz, N.; D'Almeida, M. L. O.; Frollini, E., Cellulose swelling by protic solvents: which properties of the biopolymer and the solvent matter? *Cellulose* **2008,** *15* (3), 371-392.

17. Klemm, D.; Philipp, B.; Heinze, T.; Heinze, U.; Wagenknecht, W., General Considerations on Structure and Reactivity of Cellulose: Section 2.2–2.2.3. In *Comprehensive Cellulose Chemistry*, Wiley-VCH Verlag GmbH & Co. KGaA: 2004; pp 43-82.

18. Klemm, D.; Philipp, B.; Heinze, T.; Heinze, U.; Wagenknecht, W., General Considerations on Structure and Reactivity of Cellulose: Section 2.3–2.3.7. In *Comprehensive Cellulose Chemistry*, Wiley-VCH Verlag GmbH & Co. KGaA: 2004; pp 83-129.

19. Fidale, L. C.; Ruiz, N.; Heinze, T.; Seoud, O. A. E., Cellulose Swelling by Aprotic and Protic Solvents: What are the Similarities and Differences? *Macromolecular Chemistry and Physics* **2008,** *209* (12), 1240-1254.

CHAPTER 3. RAPID FLOW IN MULTILAYER MICROFLUIDIC PAPER-BASED ANALYTICAL DEVICES

3.1 Chapter Overview

Microfluidic paper-based analytical devices (μPADs) are a versatile and inexpensive point-of-care (POC) technology, but their widespread adoption has been limited by slow flow rates and the inability to carry out complex online analytical measurements. In the present work, we investigate multilayer μPADs as a means to generate enhanced flow rates within self-pumping paper devices. Through optical and electrochemical measurements, the fluid dynamics are investigated and compared to established flow theories within μPADs. Critically, we demonstrate a ~168-fold increase in flow rate (velocity = 1.85 $\text{cm}\cdot\text{s}^{-1}$, volumetric flow rate = 1.95 $\text{mL}\cdot\text{min}^{-1}$, over 5.5 cm) through precise control of the channel height in a two-layer paper device, as compared to archetypical single-layer μPAD designs. These design considerations are then applied to a self-pumping sequential injection device format, known as a three-dimensional paper network (3DPN). These 3DPN devices are characterized through flow injection analysis of a ferrocene complex and anodic stripping detection of cadmium, exhibiting a 5× enhancement in signal compared to stationary measurements. This work was published in Lab on a Chip. Dr. Robert B. Channon and I are co-first authors on this manuscript and equally contributed to the experimental work and writing. He was responsible for applying the rapid flow phenomenon to improve electrochemical detection of metals on the μPADs. Alexis G. Scorzelli and Elijah M. Henry both helped with volume dependent studies and explored various device designs.

3.2 Introduction

The recent emergence of point-of-care (POC) devices has transformed analytical science by enabling in-situ detection of a wide range of analytes across a variety of measurement domains.[1] POC devices are often characterized by their simplicity and low-cost compared to traditional measurement technologies.[1] These features have brought quantification and treatment from centralized laboratories to home and field, resulting in significant enhancements in patient care.[1,2] However, high sensitivity, high selectivity and complex reaction schemes are challenging to implement in a POC format without adding cumbersome and/or expensive external equipment.[1-3]

Microfluidic paper-based analytical devices (μPADs) are an attractive POC platform, given their portability, disposability, simple fabrication with inexpensive materials, ease of use, ability to store reagents, and compatibility with a wide range of analytes.[4-7] Sample transport is generated through capillary action, circumventing the need for external pumps and reducing device cost and complexity.[8, 9] Despite their widespread use, μPADs face several significant challenges, including the effect of testing conditions (e.g. humidity),[10] low sensitivity,[9] low selectivity,[11] sample loss,[12] and additional challenges associated with adapting POC technologies from the lab to the field.[13] In particular, low transport velocities within μPADs result in long assay times (40 – 60 min),[8, 14-18] which diminishes their effectiveness as POC assays.

Sample flow in μPADs is frequently described by the Lucas-Washburn equation,

$$l(t) = \sqrt{\frac{\gamma r t \cos\theta}{2\mu}} \qquad (3.1)$$

where l is the distance traversed down the channel (m) at time t (s), γ is the interfacial tension ($N \cdot m^{-1}$), r is the mean capillary radius (m), θ is the fluid contact angle on the paper, and μ is the fluid viscosity ($N \cdot s \cdot m^{-1}$). Many experimental factors, such as sample volume, gravity, fiber swelling, viscous drag and evaporation effects are not treated within Equation (3.1),[5] and more comprehensive analytical[10, 19-21] or computational[22] modeling is challenging, often requiring ad hoc variables to fit theory to experimental data.[10]

Control of sample flow rate in μPADs is critical for optimizing most assays. The slow to moderate flow rates common in μPADs result in slower data acquisition times compared to classical microfluidic devices (tens of minutes versus seconds). This limitation can be attributed to the paper substrates' ability to transport sample via capillary action. In some applications, lower flow rates may be desired, such as for enzymatic reactions that proceed slowly.[9, 23] However, fast flow rates are needed for measurement of quasi-stable species and for enhancement of electrochemical signals through increased mass transport.[9, 10, 24] Recently, μPADs have been developed with increased sample velocities through use of either hollow channels,[18, 22] carved channels,[15] or multiple layers of paper through stacking or folding.[9, 10, 22, 25] Hollow channels, in particular, have been shown to give a ~7× increase in flow rate compared to single-layered devices.[18] Many of these approaches, however, require the use of syringe pumps or head pressure to increase flow rates. Flow rates in μPADs are also complicated by evaporation,[10, 26] changes in substrate properties (e.g., pore size and fiber width) between different paper types,[4, 27] and swelling of the paper fibers.[22] Although evaporation effects are often managed through sealing of devices with tape or lamination,[5, 9, 10] the effect of this sealing on flow rates within μPADs has not been formally investigated, to the best of our knowledge.

Methods for the sequential injection of multiple reagents are critical for μPAD advancement.[14, 28] However, slow flow rates, the need to introduce reagents in a specific order,[29] the requirement for different reaction times for different assay steps,6 and manual manipulation errors[30] have made μPADs challenging to design, and difficult to use with rapid assay protocols. Sequential-injection μPADs have been developed to address this need,[17, 23, 31, 32] most notably one- and two-dimensional paper networks (1DPN, 2DPN).[19, 29, 33] Unfortunately, many of the approaches described to date are impractical for POC settings (i.e., operator instigation[34-36] or specific temperature or electrical signals to open or close valves[37]) and most designs still suffer from long reaction times and undue sample mixing between successive injections.[19] In summary, whilst several reports have investigated the introduction of multiple reagents and functionalities within μPADs, the fast, controlled and timed sequential addition of multiple reagents remains a challenge.[14, 17, 38]

In this work, we present the design of multilayered μPADs that exhibit considerably higher flow rates than previously described.[29, 32, 33] We first characterize fundamental aspects of sample flow in these devices. We also describe the ability to apply these devices for timed, sequential injections in a self-pumping format, henceforth referred to as a three-dimensional paper network (3DPN). Through careful device design, the flow rate and injection timings can be tuned for specific applications. Electrochemical detection and optical imaging are used to characterize the flow phenomena, leading to an improved understanding of flow within 3DPNs. The device's analytical potential is demonstrated by comparing square-wave anodic stripping analysis of cadmium in a paper-based spot test, a μPAD, and a 3DPN.

3.3 Experimental Section

3.3.1 Materials and Equipment

Whatman grade 1 chromatography paper, Whatman grade 1 qualitative paper, and Whatman grade 4 qualitative paper were purchased from GE Healthcare sciences (UK). Scotch Heavy Duty Shipping packing tape (3M) and Scotch Permanent double-sided tape (3M) were purchased from Office Max. Great Value FD&C Red 40 dye was purchased from Wal-Mart Stores, Inc. (Bentonville, AR). Conductive Ag paint was purchased from SPI Supplies (West Chester, PA, USA). Potassium nitrate (KNO_3), ferric chloride ($FeCl_3 \cdot 6H_2O$), sodium hydroxide (KOH), and 30% hydrogen peroxide (H_2O_2) were purchased from Fisher Scientific (Fairlawn, NJ, USA). Cadmium(II) nitrate, bismuth(III) oxide and sodium acetate trihydrate were purchased from Sigma Aldrich (St. Louis, MO). Glacial acetic acid was purchased from EMD Millipore (Billerica, MA). Au and Ag microwires (both 25 μm diameter, 99.99% pure) were purchased from California Fine Wire Company (Grover Beach, CA, USA) and ferrocenylmethyltrimethylammonium hexafluorophosphate ($FcTMA^+$) was synthesized according to a previously described procedure.39 All solutions were prepared in ultrapure Milli-Q water (18.2 MΩ·cm, MilliPore, MA, USA). The humidity in the laboratory varied between 25 and 40% from day to day. Nothing was done to control humidity during experiments. All devices were printed with a Xerox ColorQube 8870 wax printer (Norwalk, CT, USA), and lamination was performed with an Apache AL 13P thermal laminator. Paper and tape segments were cut with a 30 W Epilog Zing Laser Cutter and Engraver (Golden, CO, USA) for device fabrication.

3.3.2 Device Fabrication

Two multilayer μPAD designs were tested, namely straight channel and 3DPN devices, as illustrated in Figure 3.1 and Figure 3.7a respectively. All devices were designed in CorelDRAW

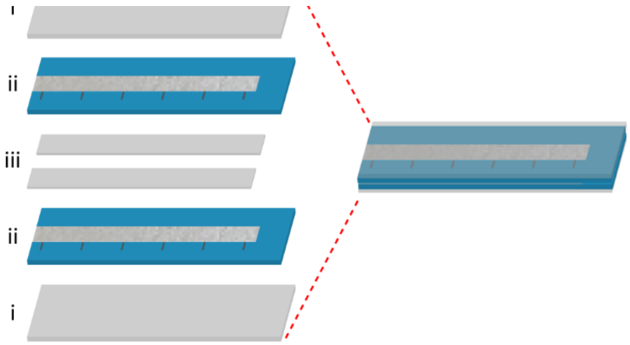

Figure 3.1. Illustration of straight channel multilayer µPADs, fabricated from i) packing tape, ii) wax-modified Whatman 1 qualitative paper and iii) double sided tape.

X4 (Ottawa, Ontario, CAN), fabricated from Whatman 1 chromatography paper (thickness = 96 µm, mean capillary radius = 0.22 µm) and printed with "Sky Blue" (R = 0, G = 124, B = 195) colored wax (Figure 1-ii). To confine the fluid flow, hydrophobic wax barriers were created by melting wax printed devices on a hot plate (Fisher Scientific IsoTemp) at 150°C for 90 s. The µPADs all featured a channel width of 4.52 mm after printing and melting the wax barriers. Each device was then laser cut using a CO_2 engraver (Epilog, Golden, CO) to individually separate them. Multilayer paper devices were held together with double sided tape (78 µm thickness, Figure 1-iii); the distances between the multiple sheets of paper were varied by stacking multiple layers of double sided tape between them (78 µm increments). The double-sided tape was hand cut to fit the outside of the paper channel on the wax region of the device (Figure 3.1-ii). Unless otherwise stated, packing tape was used to seal the outside of the µPADs and 3DPNs (Figure 1-i), the µPADs were held vertically (90° relative to the benchtop), and experiments were started by lowering the device onto microwells containing the dye or electrochemical mediators.

3.3.3 Electrochemical and Image Analysis

All electrochemical measurements were carried out with a CH Instruments 1242B model potentiostat (Bee Cave, TX, USA) with an Au microwire working electrode. For $FcTMA^+$ oxidation, and Ag/AgCl reference/counter electrode was used in a 2-electrode setup.[9] For stripping analysis, three Au electrodes were used as working, pseudo-reference and counter electrodes in a 3-electrode setup. Before use, fresh Au microwires were cut and cleaned by submerging in a solution containing 25% H_2O_2 and 50 mM KOH for 20 min, followed by submerging in ultra-pure water for 5 min.[40] Ag/AgCl reference electrodes were fabricated by submerging an Ag microwire in 50 mM $FeCl_3$ for 50 s then submerging in ultrapure water for 5 min.[41] All videos and pictures were recorded with an Nikon Coolpix L110 camera and analyzed in MPC-HC (Windows). Conductive Ag paint was used to make an Ohmic contact between the microwire and the potentiostat's alligator clips. Square-wave anodic stripping voltammetry was carried out through deposition at –1.6 V vs an Au reference electrode for different times based on the device format. Square wave stripping voltammetry was carried out after a 10 s equilibration time, scanning from −1.5 to 0 V, with a 15 mV a step potential, 75 mV amplitude and 10 Hz frequency.

3.4 Results & Discussion

3.4.1 Investigation of Sealing method

As highlighted by various research groups, the sealing method can have significant effects on flow in μPADs.[10, 17, 42] Therefore, the flow rate in straight channel μPADs was investigated using packing tape, lamination and an unsealed control (open) for a single layer of paper. Flow rates were calculated by monitoring the time the fluid front from of a 150 μL aliquot of diluted food dye traversed a straight channel μPAD. As shown in Figure 3.2a, significantly faster flow rates are observed for taped ($0.014\ cm{\cdot}s^{-1}$) over both open ($0.0057\ cm{\cdot}s^{-1}$) and laminated devices

($0.0033\ \mathrm{cm{\cdot}s^{-1}}$), for distances up to 4.2 cm. Slower flow rates are expected in the open device, as evaporation leads to a significant reduction in flow rate over longer distances.[10] We attribute the faster flow rates in taped devices over laminated ones to the generation of micropores between the tape and paper, which are not present in lamination due to a tighter seal.[9] In fact, flow in the open and laminated devices had completely ceased by ~4.5 cm. Additionally, it has been reported[12] that laminated devices may impose additional mechanical compression that shrink the pores or otherwise change their supramolecular structure.

3.4.2 Multilayer Paper Design

Next, the effect of multiple layers of paper on the flow rate was investigated. Since 1710, various mathematical fits to model flow between closely positioned substrates (glass capillaries, paper, etc.) have been reported.[43-50] However, the application of fast flow between paper layers has received comparatively little attention. Recently, parallel substrates (hydrophilic and hydrophobic) have been used in tandem for fast and continuous flow for applications in paper spray ionization.[51] Previous reports on fast flow μPADs have employed 2 layers of paper or hollow channels.[9, 10, 18] In this study, the flow rate of 150 μL of red dye down the length of the device (6.22 cm) was noticeably faster for 2 ($0.010\ \mathrm{cm{\cdot}s^{-1}}$) and 3 ($0.0075\ \mathrm{cm{\cdot}s^{-1}}$) layer devices compared to single ($0.0047\ \mathrm{cm{\cdot}s^{-1}}$) layer devices as shown in Figure 3.2b. This is attributed to the generation of ~12 μm gaps or channels between the paper layers upon wetting, as has been previously observed.[9,10] Interestingly, μPADs with 3 layers of paper reproducibly exhibited slower flow rates than those with 2 layers. To the best of our knowledge, μPADs featuring 3 or more layers have not been previously investigated quantitatively. We hypothesize the slower flow rate in the 3-layer device is due to swelling of the paper fibers between the tape, compressing the paper layers together and thereby reducing the effective channel heights between the layers.[9]

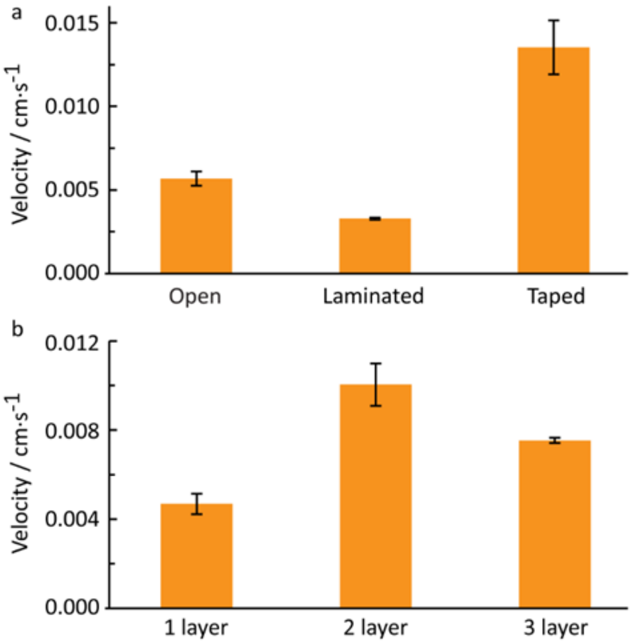

Figure 3.2. a) Open, laminated and taped sealing for straight channel µPADs, average velocity over 4.2 cm, b) Taped µPADs with different numbers of paper layers, average velocity over 6.2 cm, with 150 µL aliquot of red dye, (n = 5).

To probe this non-uniform swelling hypothesis, 2-layer µPADs were fabricated with and without a single layer of 78 µm thick double-sided tape between the paper layers (Figure 3.1a-iii). Devices without tape exhibited faster flow rates (0.035 vs 0.023 cm·s^{-1}) but showed larger variability (39% vs 15% relative standard deviation) in the flow rate (Figure S1, flow rate calculated as time required to transverse 5.55 cm). As hypothesized, the faster yet more variable flow is likely due to variations in the layer separation and manual device fabrication of each device.[9] Therefore, the use of double sided tape was investigated as a means to tune the flow rates in multilayer µPADs through control of the channel height.

3.4.3 Effect of Channel Height and Device Orientation on Flow Rates in Multilayer μPADs

Straight channel μPADs with two layers of paper were designed featuring different numbers of double sided tape layers (each layer added 78 μm) between the paper layers to investigate the effect of channel height on flow rate. Theoretical flow rates for multilayer μPADs have previously been treated through Equation (3.1), using a modified term for the effective pore radius developed by Martinez *et al.*,[10]

$$r = \frac{2r'(hw)+R(gw)}{2hw+gw} \qquad (3.2)$$

where r' is mean capillary radius of the paper, h is the paper thickness, w is the channel width, g is the channel height (gap between the layers) and R = g / 2 is the half channel height, with all measurements in meters. Equation (3.2) treats the gaps between the layers as a row of large circular pores of radius R.

Upon increasing the channel height, the flow rate increases as expected from Equations (3.1) and (3.22) (Figure 3.3a). However, we observe a maximum in the flow rate with a 234 µm gap (3 layers of tape), after which the flow rate decreases for increasing channel heights. This phenomenon is contrary to predictions that anticipate increased flow rates with increased pore radii (Equation 3.2). However, these devices were initially investigated by holding the μPADs vertically (with the channel perpendicular to the workbench), and lowering them into sample wells. Therefore, we attribute this result to the opposing forces of gravity acting on the sample mass and capillary action driven by the hydrophilic paper walls; for large gaps (channel heights), the benefit of increased pore radii is offset by the body force. To test this hypothesis, the experiment was repeated with the μPADs positioned horizontally (i.e. parallel the workbench, orthogonal to

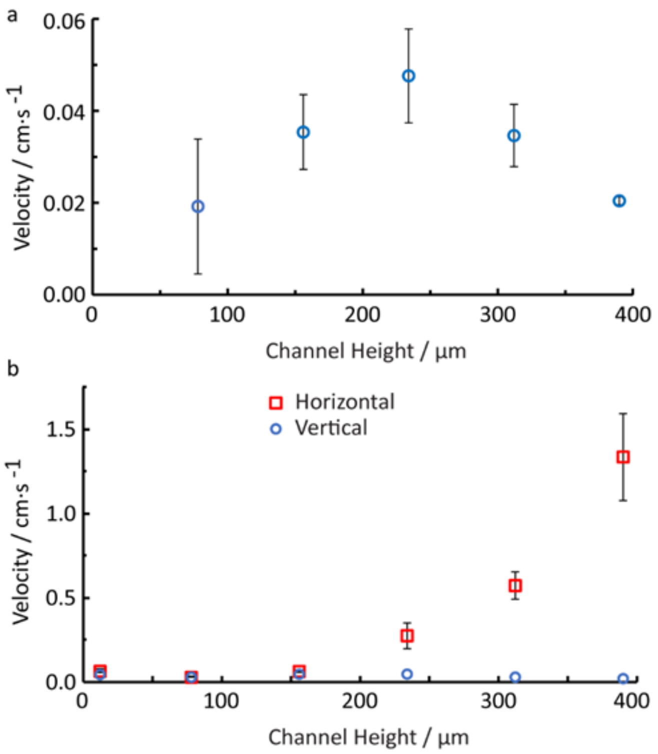

Figure 3.3. Effect of channel height on flow rate for a) vertical (blue circles) and b) horizontal (red squares) 2-layer µPADs (n = 5). Note, these flow rates are calculated based on the time taken for colored dye to flow 6.55 cm down a straight channel µPAD.

gravity). As shown in Figure 3.3b, the horizontal orientation leads to a dramatic increase in flow rate, particularly for large channel height devices. A video showing device operation is provided as supplementary information. In fact, the velocity in horizontal devices with a 390 µm channel height (5 layers of tape) represents a 69× increase (1.85 ± 0.35 cm·s^{-1}) over vertical multilayer devices with the same channel height (0.027 ± 0.002 cm·s 1), and a remarkable 168× increase over single-layer µPADs (0.011 ± 0.001 cm·s^{-1}) for flow over 5.55 cm.

3. 4.4 Analytical Treatments of Multilayer Flow µPADs

Prediction of the observed flow rates using Equations (3.1) and (3.2) proved unreliable, with a large discrepancy between the predicted and experimental flow rates. The theoretical velocity and volumetric flow rate for the fastest device (5 layers of tape, 390 μm channel height, horizontally orientated, velocity and volumetric flow rates are averaged over 6.55 cm device length) are 8.57 cm·s^{-1} and 9.06 mL·min^{-1} respectively based on Equations (3.1) and (3.2). These are significantly faster than our experimental values (1.85 cm·s^{-1} or 1.95 mL·min^{-1}) over the same distance and faster than any flow rates previously reported in μPADs. In fact, based on the observed flow rates, these equations predict significantly smaller channel heights than are present in the devices (Figure S3.3, e.g., 234 μm fabricated height versus 39.7 μm calculated). However, Equation (3.2) was developed for multilayer μPADs with small channel heights (~12 μm).[9, 10] This suggests the source of the rapid flow is more complicated than the presence of large pores between the layers as predicted by Lucas-Washburn flow.

Aside from capillary action, the main factors that could influence the fluid flow in μPADs are gravity, evaporation, pressure-driven flow, and head pressure from the inlet solution. The devices tested within this study are sealed in tape and previous investigations have shown evaporation to be minimal in sealed devices at typical laboratory humidity ranges (25 to 40%).[9]

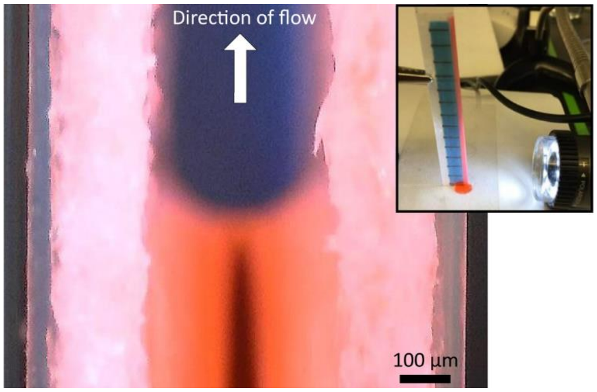

Figure 3.4. Photograph of flow for a red dye within a multilayered μPAD (390 μm channel height i.e. 5 layers of tape) orientated vertically. Devices viewed normal to the direction of flow, as shown in the inset.

Pressure-driven flow could be caused by head pressure as a result of differences in liquid levels at the device inlet and is characterized by a convex (parabolic) fluid front. Conversely, flow driven by capillary action exhibits a concave fluid front. Therefore, a multilayered μPAD (390 μm channel height), was imaged normal to the direction of fluid flow, during flow of a red colored dye (Figure 3.4). For both vertical and horizontal devices (Figure 3.4), a concave fluid front is observed, suggesting head pressure is not the dominant driving force for either orientation. Interestingly, the flow profile is concave across the channel height but convex across the channel width (parallel to the paper). To confirm that gravity is the main cause of the disparity between flow in different device orientations, the change in flow velocity was measured for μPADs held horizontally (red squares), vertically (blue circles) and at a 45° angle (green triangles), (Figure 3.5). Interestingly, the velocities are similar over short distances (within one standard deviation for <2 cm traversed), but diverge dramatically over longer distances. A similar trend is observed for orientation experiments in μPADs using a single layer of paper, although the divergence between the orientations is significantly smaller (Figure S4). These data are in accordance with the

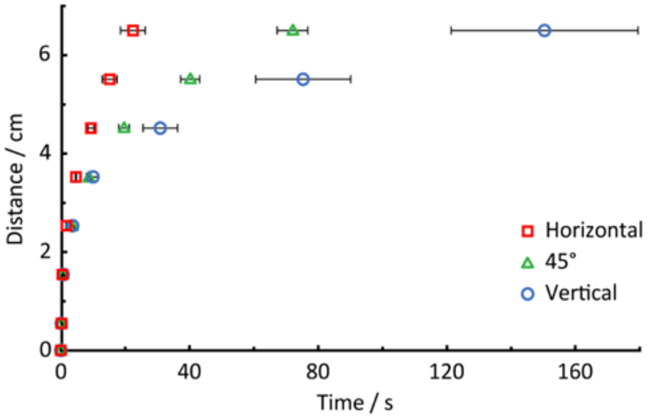

Figure 3.5. Length traversed down straight channel 2-layer μPADs with 234 μm channel height, for horizontal (0°), 45° and vertical (90°) placement above the workbench (n = 5).

hypothesis that gravity retards flow in vertically orientated μPADs, and that this effect is pronounced in multilayer devices.

There are a few literature examples of fast flow μPADs employing different channel formation concepts using either microchannels (150 μm × 50 μm) mechanically cut into the paper,[15, 16] multilayers with unfixed height (12 μm × 5 mm),[9] hollow channels between wax and paper (180 μm × 2.5 mm),[18, 22] or hollow channels between PDMS and paper (160 μm × 1 mm).[52] Unfortunately, the exact mechanism of fast flow in these examples are rarely discussed, though the addition of external forces such as head pressure or syringe pumps are likely a major driving force. To set our fast flow rates in context, Table 3.1 provides velocities and volumetric flow rates for literature examples of fast flow μPADs. These values illustrate the different approaches but do

Table 3.1. Literature examples of fast flow μPADs, where v_x is the velocity, and V_f is the volumetric flow rate. Note channel cross sections are estimated based on the air gap around the paper / between paper layers and assuming negligible flow through the paper itself. This may overestimate v_x and underestimate V_f for devices where significant fluid is transported through the paper, such as the syringe pump driven flow.[12, 33]

Method	v_x / cm·s^{-1}	V_f / mL·min^{-1}	Ref.
2 layer μPAD with controlled channel height (***passive***)	1.85	1.95	This worl
Syringe pump driven flow in blade cut paper channels	22	0.10	1
Hollow channel between paper and wax, *4 mbar inlet pressure*	1.2	0.21	2
Hollow channel between paper and wax, *0.4 mbar inlet pressure*	0.89	3.9×10^{-3}	4
Syringe pump driven flow in hollow channel between paper and PDMS	0.40	3.8×10^{-3}	5
1 layer μPAD (***passive***)	0.19	4.5×10^{-3}	6
2 layer μPAD with unfixed channel height (***passive***)	0.020	7.1×10^{-6}	7

not reflect optimal speeds due to different priorities and levels of optimization in the different studies, as well as different device channel lengths and widths. For example, the velocity for the 5 tape layers device (horizontal) is 15.5 and 5.09 cm·s^{-1} over 1.55 and 3.55 cm, respectively. Note, these alternate methods do not achieve the same velocities and/or volumetric flow rates as the multilayer μPADs, even with the use of more expensive or complex approaches such as using syringe pumps or inlet wells to create pressure-driven flow.

3.4.5 Effect of Paper Type and Sample Volume on Flow Rates

Different paper types were also tested with 3DPNs (3 layers of tape, 234 μm gap, held horizontally), as the paper thickness and porosity are known to affect the flow rate.[54] However, as shown in Table 3.2 (and Figure S3.3), after taking account of pore sizes and paper thicknesses, no significant change was seen in the flow rate based on an unpaired t-test at 95% confidence interval (n = 5 for each paper type). This further supports the hypothesis that the flow between the paper layers is the dominant driving force for the rapid flow rates in these μPADs, rather than flow in the paper alone.

Aside from selecting the best substrate, the optimal sample volume for a device is not often discussed. Equations (3.1) and (3.2) assume an infinite sample volume,[5] which is rarely applicable

Table 3.2. Effect of paper type on flow rate for vertical straight channel μPADs, where 3 layers of tape between the two paper layers (n=5), v_x is the mean velocity, SD is the standard deviation, h is the paper thickness and r is the pore size.[3]

Paper type	v_x / cm·s^{-1}	SD	r / μm	h / μm
Whatman 1 chromatography	0.071	0.012	11	180
Whatman 1 quantitative	0.053	0.004	11	180
Whatman 4 qualitative	0.058	0.009	22.5	205

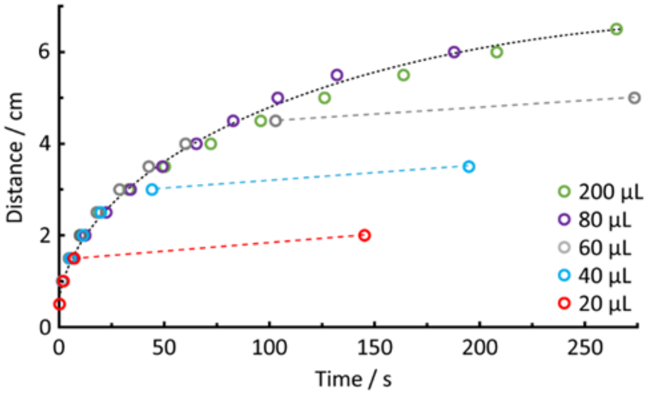

Figure 3.6. Effect of sample volume on flow rate for straight channel 2-layer µPADs with 234 µm channel height (vertical, n = 5). Dashed lines represent best-fit approximations to illustrate the primary flow regime (black dashed curve) and the secondary flow regime upon depletion of the inlet wells (red, blue and grey dashed lines).

to real systems. Practically, sample volume is either finite and controlled (e.g., optimized analytical assays)[33] or an uncontrolled amount exceeding the device capacity (e.g., the pregnancy test). Therefore, the effect of sample volume on the flow rate for vertically orientated single and 2-layer µPADs was investigated. As shown in Figure 3.6, two velocity regimes are evident; while there is liquid within the sample inlet, a Lucas-Washburn type exponential decay in the velocity is observed (black dashed curved line). After the inlet sample is drained, the flow rate abruptly switches to a second slower regime (red, blue and grey dashed lines) likely the result of slow wetting of the paper fibers above the bulk liquid, coupled with surface tension. A picture of the device showing the final positions of the fluid fronts for the different volumes is provided in Figure S3.5).

The effect of the sample volume in a single layer paper device was also investigated using 10, 20, 40, 60, and 80 µL of blue food dye. As expected, devices with larger volumes exhibited faster flow and longer distances traveled. However, over several experiments the 60 µL test consistently showed faster flow than the 80 μL test. We attribute this phenomenon to greater intermolecular forces such as hydrogen bonding in larger sample volumes (e.g., the 80 μL test). As shown in Figure S3.5, with an excess of sample in the reservoir, the cohesive properties of water (solvent) act in opposition to the capillary forces of the paper. This is not observed in the two-layer devices, likely the result of larger capillary forces able to overcome these intermolecular forces. Further studies are underway to investigate if this phenomenon is observed in two-layer devices at larger sample volumes (>200 μL). Based on these results, we envision sample volume is another factor that can be manipulated for controlling the flow rate in 3DPNs.

3.4.6 Development of a Sequential-Injection 3DPN Device

As previously discussed, the controlled addition of reagents in an assay is an important challenge to the μPAD field. Here, we applied the concepts from the multilayer paper device to design a 3DNP device (Figure 3.7a). The device design is similar to that developed by Fu/Lutz/Yager and coworkers.[29, 32, 33, 55] When aliquots are added to the sample inlet legs (Figure 3.7a-ii circles), the liquids reach an equilibrium, then deplete sequentially.[19] A 270° fan geometry is placed at the end of the μPAD channel to ensure generation of a constant flow rate and complete depletion of sample in the inlet wells.[8, 9] Microwire electrodes (Figure 3.7a-iv) are placed across the channel, normal to the direction of flow, positioned in between the bottom layer of wax modified paper (Figure 3.7a-ii) and the double sided tape (Figure 3.7a-iii). To characterize these devices, a flow injection analysis (FIA) experiment was performed using FcTMA+ in 1-layer paper μPAD and 3DPN devices. To initiate flow, 80 μL aliquots of a) KNO_3, b) 1 mM $FcTMA^+$ with 0.1 M KNO_3 spiked with a yellow dye, and finally c) 0.1 M KNO_3 spiked with a green dye were added to the sample wells (right to left, i.e. KNO_3 first). Dyes were used to visually confirm solution mixing but did not contribute to Faradaic signals.

As shown in Figure 3.7b, there is a dramatic reduction in the residence time (time between injection and maximum signal) from 1025 s to 363 s on switching from a 3DPN device with one layer of paper (blue line) to two. A further reduction to 17 s is observed on increasing the channel gap from 1 (black line, channel height = 78 μm) to 3 layers of tape (orange line, channel height = 234 μm). The chronoamperometric profile in the single layer and smaller channel height devices (blue and black) are typical of classical FIA experiments, featuring an asymmetrical peak with a long tailed current decay back to baseline. Larger peak currents are observed in the multilayer devices due to the greater flow rate, which, in turn increases mass transport to the electrode surface. The FIA profiles feature some dispersion indicators, such as the slow initial increase in current for the 1-layer of tape 3DPN (black line). This dispersion can be observed visually from images of this device during flow, which are provided in Figure S3.6. The smaller currents observed in the multilayer 3DPN with 3 layers of tape (orange line) over the 1 layer of tape device (black line) indicate that dispersion is more prevalent in larger-channel devices, however further future device optimization and design should allow a reduction in this effect.

The estimated velocities during the $FcTMA^+$ injections were 0.98, 0.030 and 0.010 $cm \cdot s^{-1}$, respectively, for the 3 and 1 layers of tape 3DPN and single layer of paper devices. These values coupled with the peak currents suggest that the smaller channel height device gives higher collection efficiency as predicted from previously published models of microwire electrochemistry in classical flow cells.[56] Conversely, a significant proportion of the analyte likely flows past the electrode without being oxidized with larger channel heights. The peak currents in both cases are reasonable based on the estimated flow rates, however the experimental currents could not be fit to this model.[56] We hypothesize this is due to the significantly different flow profiles in these multilayer μPADs compared to classical Poiseuille flow in syringe pump driven flow devices. This problem should be treatable through computational modeling of the fluid dynamics, and would allow further optimization of these 3DPN devices. This subject is under currently under investigation. Importantly, the total time for sequential injection in the 3-tape-layer 3DPN μPADs is ~1 min, which compares favorably with previous sequential injection μPADs designs based around 1 layer of paper (~3,[23] 6,[32] 8,[17] 9,[55] 15,[33] and 60 min[29]).

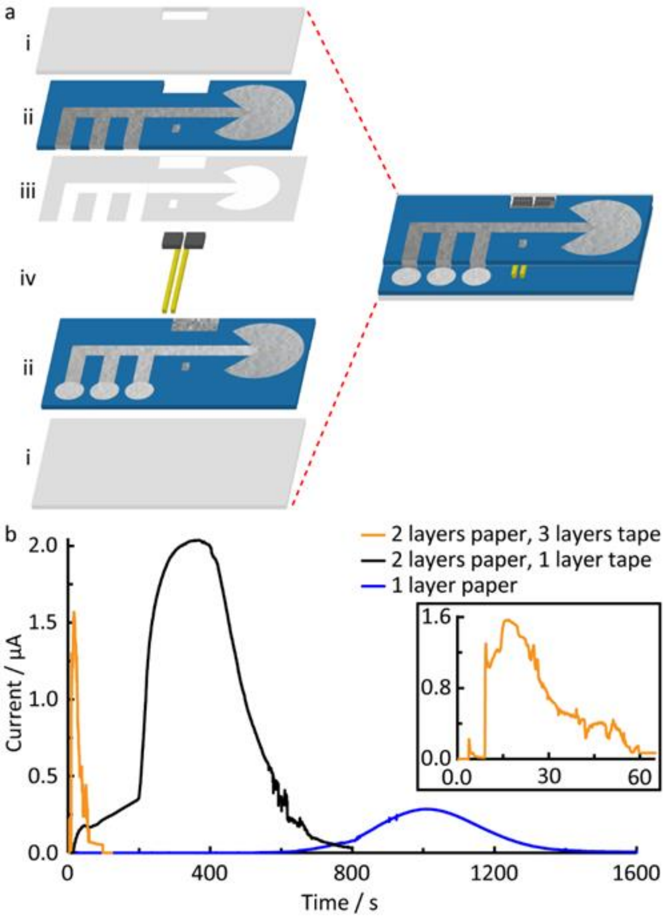

Figure 3.7. a) Illustration 3DPNs, fabricated from i) packing tape, ii) wax-modified Whatman 1 qualitative paper, iii) double sided tape, and iv) microwire electrodes. b) Flow injection analysis with 80 μL of 1 mM FcTMA$^+$ in 0.1 M KNO$_3$ using 3DPN devices with a single layer of paper (blue), 2-layers of paper with 1 layer of tape (black), and 2-layers of paper with 3 layers of tape between the layers (orange, on main plot and inset), potential =

3.4.7 Application of the 3DPN for the Stripping Analysis of Cadmium

Sequential injection μPADs have been applied previously for colorimetric reactions with dyes,[19, 55] involving pH changes,[33] immunoassays of malaria antigens,[29] or pesticide sensors.[17] However, they are yet to be demonstrated for electrochemical reactions. Here we demonstrate the 3DPN device scope for the square-wave anodic stripping analysis of cadmium. Cadmium exposure is linked to kidney failure, skeletal damage and cancer.[57] Therefore, POC detection methods, especially in particulate matter and waste water are of significant importance.[58, 59] Our approach is adapted from a previously reported method where bismuth is used to facilitate adsorption of the cadmium onto a silver electrode.[59] Sequential injections of 640 μg·L-1 bismuth in acetate buffer (40 μL), 400 $\mu g \cdot L^{-1}$ cadmium in acetate buffer (80 μL), and acetate buffer only (pH 5, 80 μL) were applied to different μPADs as shown in Figure 3.8. A deposition potential of –1.6 V is applied during the bismuth and cadmium injection, and square-wave stripping is carried out during the final injection (visualized through addition of non-electroactive dyes to the injections).

For pulsed voltammetry techniques, the peak area is known to be a better indicator of concentration than peak current due to the commonly observed shifting potential of peaks and variability of the background currents.[60] There is a clear increase in the peak area (3.5×) and thus sensitivity when moving from spot test (green) to the flowing μPADs. Additionally, moving from a 1-layer μPAD (blue) to a 3DPN (2 layers of paper, black) with 1 layer of tape and a 3DPN with 3 layers of tape (orange) evoke 1.37× and 1.43× increases in the peak area. We attribute this greater signal in the microfluidic devices compared to the spot test to the increased convective pre-concentration of the bismuth and cadmium onto the microwire electrode. The signal increases from spot test to μPAD, and tailing off of signal enhancement for faster flow (larger channel gap) 3DPN can be rationalized as follows: In the spot test, a deposition time of 360 s used, whereas in the µPADs the deposition time is based upon the time taken for the first two injections to traverse the electrodes. Therefore, deposition times of for the 1 layer of paper, 3DPN (1 layer of tape) and 3DPN (3 layers of tape) devices respectively. During injection, some material is left in the inlet legs, therefore not all 80 µL will be transported to the electrodes. This effect is likely exacerbated for multilayer devices with large channel heights and, thus, more material trapped in the inlet legs between the layers. Depending on the mass transport and fluid mixing between injections, some of the material likely passes the electrodes without being oxidized for the fastest flow rate 3DPN. Ongoing work seeks to optimize these devices through additional modeling and characterization of the flow in these multilayer devices.

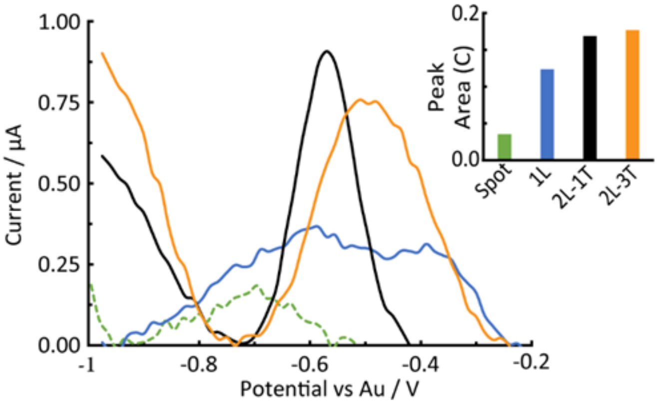

Figure 3.8. Square wave anodic stripping voltammetry of 400 ppm cadmium in a spot test (green, ‘spot’), a 1 layer of paper 3DPN (blue, ‘1L’), a 2 layers of paper 3DPN with 1 layer of tape (black, ‘2L-1T’), and a 2 layers of paper 3DPN with 3 layers of tape (orange, ‘2L-3T’) devices. All electrodes were Au microwires in a 3-electrode format spaced 1 mm apart in the channel between the paper layers or on top of the stationary spot test. Inset, corresponding peak areas from the stripping square wave voltammograms.

3.5 Conclusions

Herein, two-layer µPADs with controlled channel heights have been demonstrated featuring extremely fast flow rates through simple design considerations. Critically, these flow rates are significantly faster than previous µPAD designs from literature, without the need for flow rate enhancement methods such as syringe pumps or head pressure to drive flow. Through our investigations we have observed that rapid flow rates are possible with multi-layered devices using large channel heights (100 – 400 µm), where the height is simply controlled through addition of double sided tape along the channel edge. Velocities and volumetric flow rates of 15.5 $cm \cdot s^{-1}$ (16.3 $mL \cdot min^{-1}$) and 1.34 $cm \cdot s^{-1}$ (1.41 $mL \cdot min^{-1}$), were observed for flow over the first 1.55 and 6.55 cm respectively in a horizontally oriented µPAD (390 µm channel height).

Interestingly, the flow rates do not fit established models of flow within µPADs and analytical and computational treatment of flow within these devices is the subject of ongoing work. The effect of orientation (gravity), channel height, sample volume and paper type are investigated, and compared to classical µPAD designs. These multilayer µPADs have increased the flow rate over two orders of magnitude compared to single layer µPADs over long channel lengths (6.55 cm), without the need for external pumps, mechanical intervention, or external signals (e.g., dielectric switches) with good control.[14] These insights are also applied to a sequential injection 3DPN device, for the flow injection analysis of $FcTMA^+$ and the stripping voltammetry of cadmium. From the rapid injection time, short residence time, and enhanced sensitivity (5×) compared to stationary PADs, 3DPN should be applicable for a wide range of analytes and point-of-care applications.

We envision the flow rates in µPADs could be further enhanced through addition of inlet sample volume (pressure-driven flow),[18, 22] optimization of the slip angle,[17] or control of the channel width or length.[23, 61] Full characterization of the flow profile within these multilayer μPADs would allow for placement of microwires in regions of highest velocity within the cross section. This should enhance the mass transport and increase the device sensitivity compared to classical microfluidic devices with electrodes carefully entrenched into the channel walls.[9, 22, 62, 63] Furthermore, this two-layer format should allow for the optimized transport and detection of larger species such as micron-sized particles,[64] and blood cells in μPADs,[27] through the increased channel gap.

REFERENCES

1. S. K. Vashist, P. B. Luppa, L. Y. Yeo, A. Ozcan and J. H. T. Luong, Trends Biotechnol., 2015, 33, 692-705.
2. A. St John and C. P. Price, Clin. Biochem. Rev., 2014, 35, 155-167.
3. H. Shafiee, S. Wang, F. Inci, M. Toy, T. J. Henrich, D. R. Kuritzkes and U. Demirci, Annu. Rev. Med., 2015, 66, 387-405.
4. A. K. Yetisen, M. S. Akram and C. R. Lowe, Lab Chip, 2013, 13, 2210-2251.
5. D. M. Cate, J. A. Adkins, J. Mettakoonpitak and C. S. Henry, Anal. Chem., 2015, 87, 19-41.
6. Y. Yang, E. Noviana, M. P. Nguyen, B. J. Geiss, D. S. Dandy and C. S. Henry, Anal. Chem., 2017, 89, 71-91.
7. K. Yamada, T. G. Henares, K. Suzuki and D. Citterio, Angew. Chem., Int. Ed., 2015, 54, 5294-5310.
8. S. Mendez, E. M. Fenton, G. R. Gallegos, D. N. Petsev, S. S. Sibbett, H. A. Stone, Y. Zhang and G. P. López, Langmuir, 2010, 26, 1380-1385.
9. J. A. Adkins, E. Noviana and C. S. Henry, Anal. Chem., 2016, 88, 10639-10647.
10. C. K. Camplisson, K. M. Schilling, W. L. Pedrotti, H. A. Stone and A. W. Martinez, Lab Chip, 2015, 15, 4461-4466.
11. M. M. Gong, R. Nosrati, M. C. San Gabriel, A. Zini and D. Sinton, J. Am. Chem. Soc., 2015, 137, 13913-13919.

12. M. P. Nguyen, N. A. Meredith, S. P. Kelly and C. S. Henry, 2017, Simple Design Considerations for Reducing Sample Loss in Microfluidic Paper-Based Analytic Devices Manuscript submitted for publication.

13. C. C. Wang, J. W. Hennek, A. Ainla, A. A. Kumar, W. J. Lan, J. Im, B. S. Smith, M. Zhao and G. M. Whitesides, Anal. Chem., 2016, 88, 6326-6333.

14. E. Fu and C. Downs, Lab Chip, 2017, 17, 614-628.

15. D. L. Giokas, G. Z. Tsogas and A. G. Vlessidis, Anal. Chem., 2014, 86, 6202-6207.

16. A. C. Glavan, R. V. Martinez, E. J. Maxwell, A. B. Subramaniam, R. M. D. Nunes, S. Soh and G. M. Whitesides, Lab Chip, 2013, 13, 2922-2930.

17. S. Jahanshahi-Anbuhi, P. Chavan, C. Sicard, V. Leung, S. M. Z. Hossain, R. Pelton, J. D. Brennan and C. D. M. Filipe, Lab Chip, 2012, 12, 5079-5085.

18. C. Renault, X. Li, S. E. Fosdick and R. M. Crooks, Anal. Chem., 2013, 85, 7976-7979.

19. S. Dharmaraja, L. Lafleur, S. Byrnes, P. Kauffman, J. Buser, B. Toley, E. Fu, P. Yager and B. Lutz, Proc. SPIE, San Francisco, CA, USA, 2013.

20. C. Castro, C. Rosillo and H. Tsutsui, Microfluid. Nanofluid., 2017, 21, 21.

21. C. L. A. Berli and P. A. Kler, Microfluid. Nanofluid., 2016, 20, 104.

22. C. Renault, M. J. Anderson and R. M. Crooks, J. Am. Chem. Soc., 2014, 136, 4616-4623.

23. J. Songok and M. Toivakka, Microfluid. Nanofluid., 2016, 20, 63.

24. C. Bathany, J.-R. Han, K. Abi-Samra, S. Takayama and Y.-K. Cho, Biosens. Bioelectron., 2015, 70, 115-121.

25. M. Santhiago, J. Bettini, S. R. Araújo and C. C. B. Bufon, ACS Appl. Mater. Interfaces, 2016, 8, 10661-10664.

26. K. M. Schilling, A. L. Lepore, J. A. Kurian and A. W. Martinez, Anal. Chem., 2012, 84, 1579-1585.

27. S. C. Fernandes, J. A. Walz, D. J. Wilson, J. C. Brooks and C. R. Mace, Anal. Chem., 2017, 89, 5654-5664.

28. M. M. Gong and D. Sinton, Chem. Rev., 2017, 117, 8447-8480.

29. G. E. Fridley, H. Le and P. Yager, Anal. Chem., 2014, 86, 6447-6453.

30. D. M. Cate, S. D. Noblitt, J. Volckens and C. S. Henry, Lab Chip, 2015, 15, 2808-2818.

31. A. Apilux, Y. Ukita, M. Chikae, O. Chailapakul and Y. Takamura, Lab Chip, 2013, 13, 126-135.

32. E. Fu, P. Kauffman, B. Lutz and P. Yager, Sens. Actuators, B, 2010, 149, 325-328.

33. E. Fu, B. Lutz, P. Kauffman and P. Yager, Lab Chip, 2010, 10, 918-920.

34. K. N. Han, J.-S. Choi and J. Kwon, Sci. Rep., 2016, 6.

35. R. Gerbers, W. Foellscher, H. Chen, C. Anagnostopoulos and M. Faghri, Lab Chip, 2014, 14, 4042-4049.

36. W. Liu, C. L. Cassano, X. Xu and Z. H. Fan, Anal. Chem., 2013, 85, 10270-10276.

37. F. Liu and C. Zhang, Sens. Actuators, B, 2015, 209, 399-406.

38. J. Schoelkopf, P. A. C. Gane, C. J. Ridgway and G. P. Matthews, Colloids Surf., A, 2002, 206, 445-454.

39. S. G. Lemay, D. M. van den Broek, A. J. Storm, D. Krapf, R. M. M. Smeets, H. A. Heering and C. Dekker, Anal. Chem., 2005, 77, 1911-1915.

40. L. M. Fischer, M. Tenje, A. R. Heiskanen, N. Masuda, J. Castillo, A. Bentien, J. Émneus, M. H. Jakobsen and A. Boisen, Microelectron. Eng., 2009, 86, 1282-1285.

41. B. J. Polk, A. Stelzenmuller, G. Mijares, W. MacCrehan and M. Gaitan, Sens. Actuators, B, 2006, 114, 239-247.

42. E. T. S. G. da Silva, M. Santhiago, F. R. de Souza, W. K. T. Coltro and L. T. Kubota, Lab Chip, 2015, 15, 1651-1655.

43. B. Taylor, Philos. Trans., 1710, 27, 538.

44. F. Hauksbee, Philos. Trans., 1710, 27, 539-540.

45. J. Jurin, Philos. Trans., 1717, 30, 739-747.

46. P. S. de Laplace, Traité de mécanique céleste, Chez J.B.M. Duprat, 1805.

47. T. Young, G. Peacock and J. Leitch, Miscellaneous works of the late Thomas Young, J. Murray, 1855.

48. H. Fujita, J. Phys. Chem., 1952, 56, 625-629.

49. F. J. Higuera, A. Medina and A. Liñán, Phys. Fluids, 2008, 20, 102102.

50. C. Luo, X. Heng and M. Xiang, Langmuir, 2014, 30, 8373-8380.

51. G. I. J. Salentijn, H. P. Permentier and E. Verpoorte, Anal. Chem., 2014, 86, 11657-11665.

52. A. Ravi Kumar, P. Nivedita, C. Kaustav, C. Nripen, B. Gautam and C. Suman, J. Micromech. Microeng., 2016, 26, 105008.

53. J.-H. Shin, G.-J. Lee, W. Kim and S. Choi, Sens. Actuators, B, 2016, 230, 380-387.

54. E. Evans, E. F. M. Gabriel, W. K. T. Coltro and C. D. Garcia, Analyst, 2014, 139, 2127-2132.

55. E. Fu, S. A. Ramsey, P. Kauffman, B. Lutz and P. Yager, Microfluid. Nanofluid., 2011, 10, 29-35.

56. Q. Fulian, K. A. Gooch, A. C. Fisher, N. P. Stevens and R. G. Compton, Anal. Chem., 2 000, 72, 3480-3485.

57. L. Järup, Br. Med. Bull., 2003, 68, 167-182.

58. D. Martín-Yerga, I. Álvarez-Martos, M. C. Blanco-López, C. S. Henry and M. T. Fernández-Abedul, Anal. Chim. Acta, 2017, 981, 24-33.

59. J. Mettakoonpitak, J. Mehaffy, J. Volckens and C. S. Henry, Electroanalysis, 2017, 29, 880-889.

60. P. M. S. Monk, Fundamentals of Electro-Analytical Chemistry, Wiley, 2008.

61. S. Hong and W. Kim, Microfluid. Nanofluid., 2015, 19, 845-853.

62. J. Růžička and E. H. Hansen, Flow Injection Analysis, J. Wiley, New York, 2nd edn., 1 988.

63. S. E. Fosdick, M. J. Anderson, C. Renault, P. R. DeGregory, J. A. Loussaert and R. M. C rooks, Anal. Chem., 2014, 86, 3659-3666.

64. J. C. Cunningham, M. R. Kogan, Y.-J. Tsai, L. Luo, I. Richards and R. M. Crooks, ACS Sens., 2016, 1, 40-47.

CHAPTER 4. READ-BY-EYE QUANTIFICATION OF ALUMINUM (III) IN A DISTANCE-BASED MICROFLUIDIC PAPER-BASED ANALYTICAL DEVICE

4.1 Chapter Overview

Herein we report the first two distance-based microfluidic paper-based analytical devices (µPADs) using fluorescence to quantify aluminum. In addition to their read-by-eye quantification, the devices are simple to make, require no sample pretreatment or preconcentration and provide sensitive measurements 5 months after fabrication. The first device is designed in a “chemometer” format where the length of the fluorescent band corresponds to an Al(III) concentration. The second device uses a recently reported radial design where the diameter of a fluorescent response corresponds to an Al(III) concentration. The chemometer device exhibits a detection limit of 2.5 ppm (100 µM) and linear ranges from 2–54 ppm of Al(III) (100 µM–1mM), $R^2 = 0.9898$). The radial device exhibits a detection limit of 0.9 ppm (33 µM) and linear ranges from 2–24 ppm of Al(III) (100–900 µM, $R^2 = 0.9683$). The utility of the µPADs was demonstrated by measuring Al(III) in two water effluent samples from the Gold King Mine near Silverton, CO. Sydney P. Kelly aided in synthesizing the Al(III) detection ligand and helped confirm the calibration plot.

4.1 Introduction

Humans are continually being exposed to harmful pollutants such as metals that can cause oxidative stress.[1] As of 2000, workplace related respiratory disease has resulted in 850,000 deaths.[2] Plants also suffer from being overexposed to metals.[3] Aluminum concentrations as low at 1 ppm significantly decrease root growth, reducing the plant’s ability to uptake essential nutrients.[4] Aluminum is the third most abundant element in the earth’s crust (O: 46.6%, Si: 27.7%, Al: 8.1%, Fe: 5.0%).[5] This is a major problem for farmers in sub-Saharan Africa, more specifically Malawi, where soil pH can reach as low as 4.5 and free Al(III) ions from local minerals.[6] The highly acidic soil can free Al(III) ions for plant uptake, reducing plant yields and the livelihood of those affected. Therefore, quantitatively measuring Al(III) in soil, water, and air is important. Colorimetric reagents, such as those used for transition metals, are limited for Al(III).[7] This may be due to the lack of d-orbitals in Al(III) that allow for vibrant colors as a result of d–d or d–π interactions.[8] Some conjugated ligands, however, can luminesce due to allowed π–π* interactions. When these ligands selectively bind to Al(III), the ligand structure is restricted from rotation and the fluorescence intensity may be increased. One of the earliest fluorescent chemosensors was reported by Goppelsröder in 1867 for Al(III) detection.[9] Since then, many fluorescent chemosensors have been reported and commercialized.[10] Unfortunately, these sensors require large, immobile fluorimeters, reliable power and trained staff. Therefore, monitoring dilute samples in complex matrices in a rapid, quantitative, and easy to use platform in the field is difficult. This difficulty is exacerbated in remote settings such as Malawi where power, centralized laboratories, and trained personnel may be neither accessible nor affordable. Microfluidic paper-based analytical devices (µPADs) are an alternative that have proven effective at reducing costs by increasing the portability, decreasing the cost, and making quantitative analysis user-friendly.[11]

Herein we report the first two distance-based µPADs to quantify Al(III). These two small, inexpensive, and easy-to-use devices are also the first distance-based µPADs to quantify concentrations of Al(III) using a fluorescence detection motif. The first device, referred to as a "chemometer" for its resemblance to a thermometer, uses the length of a fluorescent band to determine concentration. The limit of detection for Al(III) chemometer is 2.5 ppm (100 µM) with a good linear fit of the concentration to the fluorescent band length between 2–54 ppm (100 µM–1 mM, $R^2 = 0.9898$). The second device uses a radial design where the diameter of a fluorescent signal is used to quantify the concentration of Al(III). For radial devices, the LOD is 0.9 ppm (33 µM) and the linear range spans 2–24 ppm (100–900 µM, $R^2 = 0.9683$).

4.2 Experimental Section

4.2.1 Reagents

All of the following commercially available reagents were analytical grade and used as received without further purification: hydroxy-1-naphthaldehye, benzhydrazide, 1,10-phenanthroline, 2,2’-bipyridine, potassium thiocyanate, sodium fluoride, sodium acetate, dithiooxamide, neocuproine, catechol, and ethylenediaminetetracetic acid, iron(III) chloride, copper(II) chloride, aluminum(III) sulfate and acetonitrile, acetonitrile-d_3, and ethanol. Al(III), Fe(III) and Cu(II) solutions were made with ultrapure water (18.2 MΩ·cm) from a Mill-Q system (Merck Millipore Darmstadt, Germany) and used throughout. Whatman Grade 4 Qualitative (W4Qual) filter paper was purchased from GE Healthcare Life Sciences. Scotch™ heavy duty packing tape and 3 mil Scotch™ thermal lamination pouches sealed their respective devices. Gold King Mine samples were collected by Casey Quinn and concentrations of metals were verified with ICP-MS by the Proteomics and Metabolomics facility at Colorado State University.

4.2.2 Ligand Synthesis & Characterization

The synthesis of the ligand (L) used is reported by Liu *et al.*[10c] Following this procedure, we added 0.34 g of 2-hydroxy-1-naphthaldehye, 0.27 g of benzhydrazide, and 32 mL of ethanol in a 125 mL round bottom flask and refluxed the mixture at 70 °C for 2 h. The contents were slowly cooled to room temperature (22 ± 2 °C). The round bottom flask was then further cooled with ice water for 2 h where 0.22 g (40% yield) of the yellow-white colored crystalline precipitate was formed. On one occasion, the sides of the vial were scratched with a glass stir rod to help facilitate crystalline precipitation. These crystals were washed with 3 × 5 mL portions of cold ethanol to

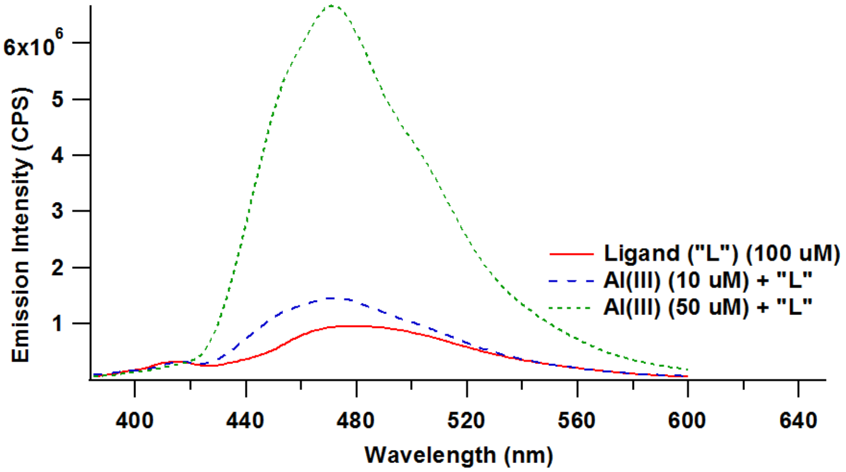

Figure 4.1. Fluorescence spectra of the detection ligand, “L”, and “L” with varying Al(III) concentrations. The emission maxima at 471 nm resulted with a 365 nm excitation in a 1:1, H_2O:CH_3CN mixture.

remove any impurities. A ^{1}H NMR spectrum for the ligand, “L”, was collected in CD_3CN using a 400 MHz Bruker NMR and a 4 T field, with chemical shifts and integrations that indicate a pure product to match what Liu *et al.* reported. The NMR spectrum is found in Figure S4.1. Fluorescence spectra for L and the ligand–metal (L–M) complex were collected on a Horiba fluorimeter that matched what Liu *et al.* reported.[10c] The fluorescence spectra in Figure 4.1 were measured using a 365 nm excitation in a 1:1, H_2O:CH_3CN mixture which resulted in an emission maxima at 472 nm.

4.2.3 Device Fabrication

Chemometer device patterns were designed in CorelDrawX4 and printed on Whatman Grade 4 Qualitative filter paper using a “Sky Blue” (R = 0, G = 124, B = 195) colored wax with a Xerox ColorQube printer. The devices were then laser cut out of the paper using an Epilog Zing CO_2 laser and melted (wax faced down) on a hot plate for 90 s at 150 °C to ensure the wax coated the paper fibers to create a channel for directed fluid transport. In some devices, black tick marks were printed to make quantifying the length of the fluorescent band easier. The sample inlet was 5 mm in diameter, the channel was 3 mm wide, and the device was 30 mm total in length. The fan shaped reservoir at the end of the device was added to increase sample transport to the end of the device as reported by Nguyen *et al*.[12] The bottom of the device was then sealed with packing tape. The L reagent was then pipetted onto the paper channel using four channels in a multichannel pipet. 4×10 µL of L at 190 µM in a 50:50 (v:v) mixture of 2-methoxyethanol:water was added to the device. Once the reagent was dried, packing tape was added to the top of the device to further ensure external contaminants did not interfere with the assay and reduce the impact of evaporation. The radial device was made in a similar fashion, however the paper devices were sealed using a 3 mil lamination sheet with 2 mm diameter laser cut holes in the top of the sheet for sample delivery. The diameter of the wax printed barrier was 50 mm. Additionally, the reagents were printed using a modified Epson R280. The modifications are previously described by Derby.[13]

4.2.4 Device Use & Calibration Curves

12.5 µL of an aqueous Al(III) sample was added to the sample inlet and was allowed to flow to the end of the chemometer using an Eppendorf 20 µL pipette. This volume was optimized for a 30 mm long paper device. Once the solvent front reached the end of the reservoir, a handheld UV-light (385 nm) irradiated the top surface of the device and the length was recorded. If solution wetted the entire device, no difference in the distance was observed with wet and dry devices. Multiple handheld UV-light lamps with reported wavelengths below 400 nm were sufficient to excite the L–M complex. The calibration plot was generated using 8 replicate measurements. An image of the chemometer and the calibration plot are found in Figure 4.2. When using the radial device, 100 µL of the aqueous Al(III) sample was added to the sample inlet. The calibration plot for the radial device were generated using 6 replicates. An image of radial devices with the calibration plot are found in Figure 4.3. Distances were measured with digital calipers to generate calibration plots for both device formats.

4.3 Results & Discussion

4.3.1 Ligand Selection

For µPADs to be useful in resource-limited settings at the point-of-need, the selected detection reagents should be inexpensive, specific to the analyte, widely available or requiring only facile synthetic techniques and demonstrate long-term stability.[14] In addition, the detection reagent should be sparingly water soluble and its reagent–analyte complex should be a precipitate. If the detection reagent is sparingly water soluble or soluble in a water/organic solvent mixture, it will more likely adhere to the paper fibers when aqueous samples are added to the device. This is especially important for designing distance-based µPADs where well-defined color bands are necessary. If the detection reagent's reagent–analyte complex precipitates out of solution, a more uniform signal across a given detection zone will persist. As demonstrated by Nguyen *et al.*, this will improve colorimetric detection where surface-based measurements such as reflectance (i.e. using a camera or flatbed scanner) are employed.[12] With these desired traits to consider, we tested the naphthol system reported by Liu *et al.* as we hypothesized that it would meet the above criteria.[10c]

4.3.2 Chemometer & Ligand Deposition

We designed our first µPAD to be a spot test where the relative fluorescent intensity was expected to be proportional with the Al(III) concentration. However, we found that there was no easily discernible difference in fluorescence between large Al(III) concentration differences (300, 500, 700, 900 µM and 20 mM) by visual inspection. An image of the spot test with replicates of various concentrations irradiated with UV-light is shown in Figure S4.2. The failure of the spot test to enable quantification led us to develop a distance-based sensor or “chemometer” format of the sensor. After testing different ligand deposition techniques and paper types, we used a multichannel pipet to add reagents, which provided the data with the best linear correlation. The data for the reagent deposition methods is shown in Figure S4.3.

4.3.3 Distance-Based Detection with Chemometer µPADs

Here, the chemometer device was adapted to present the first distanced-based µPAD for detecting Al(III). Solutions of Al(III) of 2.7, 5.4, 8.0, 11, 14, 16, 19, 22, 40, 54, 269, 809 ppm (100, 200, 300, 400, 500, 600, 700, 800, 1,500, 2,000, 10,000, and 30,000 µM) were tested to create a calibration curve of Al(III) concentration versus distance. A linear response from 2.7–54 ppm (100–2000 µM) was observed with a linear correlation of $R^2 = 0.9898$. The working range of the device is from 2.7–809 ppm (100 µM–3 M). Due to the very small volume used (12.5 µL), analysis can be completed in 10 min. Analysis is faster here than previous chemometer designs that require longer times prior to quantification.[15] The limit of quantification (LOQ) was found to be 2.7 ppm (100 µM) as anything below this concentration did not show any fluorescent response.

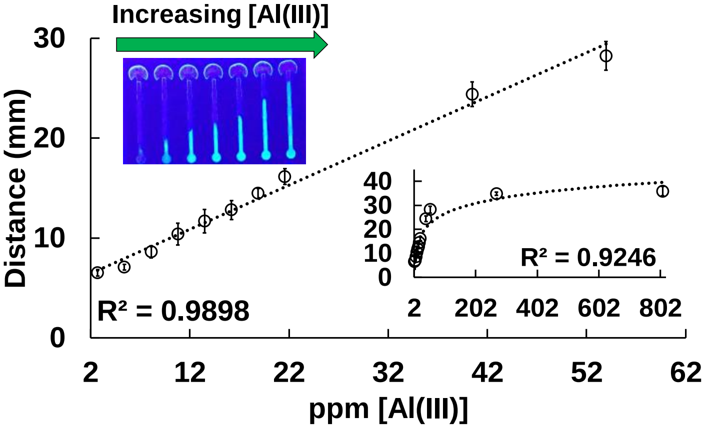

Figure 4.2. Linear range, working range (inset) and image of chemometer devices (n = 8). Inset plot’s axes and units are the same as the enlarged plot.

The limit of detection (LOD) was calculated by multiplying 3.3 by the standard deviation divided by the slope of the line [LOD = 3.3(σ/slope)] and determined to be 2.5 ppm (91 µM).

4.3.4 Diameter-Based Detection with Radial µPADs

Next, the radial µPAD was adapted for detecting Al(III) (Figure 4.3). The reagent printing method for ligand deposition led to clogged nozzles. The clogged nozzles created streaks or striations where the reagent ink did not fully cover the device detection area. Despite the striated devices having less reagent ink covering the surface of the paper, these devices performed surprisingly similar to the fully printed channels. Images of the devices and the data for their distances-concentration values are shown in Figure S4.5. With the radial µPAD, a linear response from 2.7–24 ppm (100–900 µM) was observed with a linear correlation of $R^2 = 0.9683$. The linear range is smaller than that of the chemometer (from 2.7–54 ppm or 100–2000 µM). The working range of the device is from 2.7–67 ppm (100–2500 µM). In the radial device, the limit of the 50 mm diameter device does not allow for measurement of higher concentrations. Due to the larger volume used (100 µL), analysis is completed in 3 min. Analysis here is faster than previous

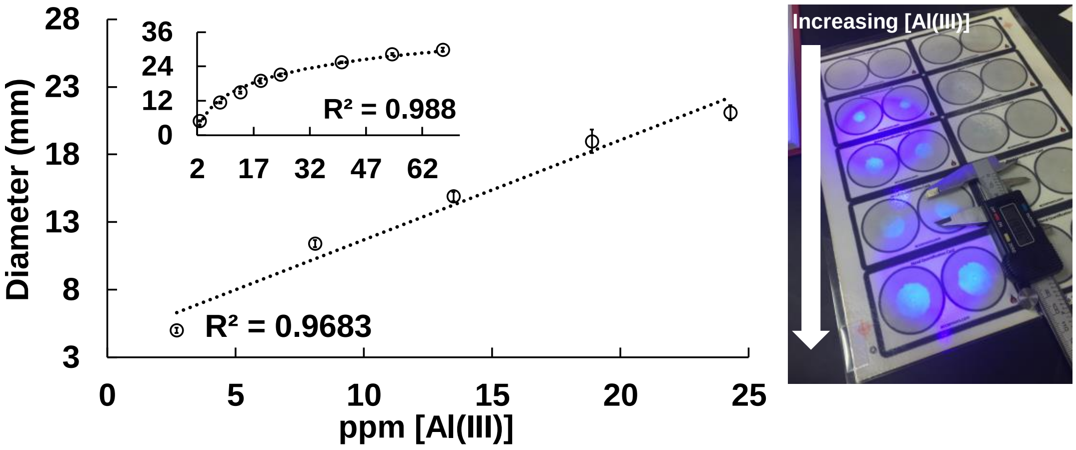

Figure 4.3. Linear range, working range (inset) and photograph of radial devices (n = 4). Inset plot's axes and units are the same as the enlarged plot.

chemometer designs.[15] The limit of quantification (LOQ) was found to be 2.7 ppm (100 µM) as anything below this concentration did not show any fluorescent response. The LOD, calculated as described above, was determined to be 0.9 ppm (33 µM). This LOD is lower than the chemometer (2.5 ppm or 91 µM) and allows for the measurement of Al(III) that is relevant to plant health (1 ppm).

4.3.5 Stability

The stability of the Al(III) assay for radial devices was investigated. Devices were stored in the dark at room temperature (22 ± 2 °C) for ~5 months prior to testing. With the same sample addition procedure and different stock solutions, the diameter responses were recorded for concentrations of 5.4, 8.0, 13, 16, 19, 22, 24, 27 ppm (200, 300, 500, 600, 700, 800, 900 µM). Each concentration was tested (n = 1) and the results agreed well with the calibration plot. The uncertainty in the slope was calculated and verified that there is no statistical difference between the original and the stored devices (Original plot: slope ± uncertainty in slope = 0.0198 ± 0.0021;

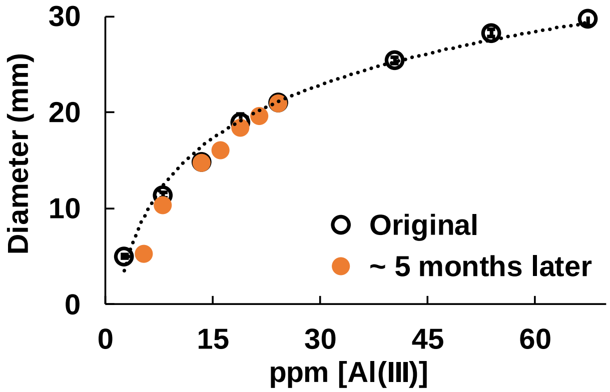

Figure 4.4. Calibration plot for radial devices before (n = 4) and after ~5 months of storage (n = 1) showing the robustness of the assay and the device.

5 months old plot: slope ± uncertainty in slope = 0.0213 ± 0.0020). The results of this stability test are shown in Figure 4.4.

Table 4.1. Tabulated performance metrics comparing the chemometer and radial devices.

	Chemometer	**Radial**
LOD (ppm)	2.5	0.9
LOQ (ppm)	2.7	2.7
Linear Range (ppm) [Correlation]	2.7–54 [0.9898]	2.7–24 [0.9683]
Working Range (ppm)	2.7–809	2.7–67
Volume Needed	12.5 µL	100 µL
Time to Quantification	10 minutes	3 minutes

4.3.6 Interferences & Masking Studies

While this ligand displays a highly selective and robust turn-on fluorescent response with Al(III), Fe(III) and Cu(II) also bind L, turning off the fluorescent response. The ligand L has such a strong preference for Fe(III) and Cu(II) that when the fluorescent Al–L complex encounters Fe(III) or Cu(II) ions, the system undergoes a transmetallation step. This transmetallation step or replacement of Al(III) for Fe(III) or Cu(II), turns off the fluorescent response. Hard-soft acid-base (HSAB) theories supports the similar binding of Fe(III) and Cu(II) to the ligand as Al(III). In agreement with this theory, Fe, Cu and Al are all hard to intermediately hard acids and react strongly with hard bases such as RO^- and N_2H_4 that make up the ligand structure, L. Masking agents were explored to remove the issues of interference. The chelation of Fe(III) and Cu(II) was tested by using 1,10-phenanthroline, 2,2’-bipyridine, potassium thiocyanate, sodium fluoride, sodium acetate, dithiooxamide, neocuproine, catechol, and ethylenediaminetetracetic acid were tested. The addition of these ligands onto the device eliminated fluorescent signal, likely due to the chelation of Al(III). The precipitation of metal hydroxides to remove the interferences was also considered, however the KSP of $Al(OH)_3$ (1.4×10^{-34}) is between that of $Fe(OH)_3$ (6.0×10^{-38}) and $Cu(OH)_2$ (2.2×10^{-20}). Previous assays have described the use of ascorbic acid (+0.34 V) to eliminate Fe(III) by reducing it to Fe(II) (–0.77 V).[16] This was used to also reduce Cu(II)→Cu(0)

(+0.34 V) as the reduction potential is at more positive values than with Fe(III). Unfortunately, the use of ascorbic acid resulted in no fluorescent signal. The same result was observed for citric acid (–0.18 V).[17] Out of Al(III)→Al(0) (–1.66 V), Fe(III) and Cu(II), Al(III) is the hardest ion to reduce and thus a stronger reducing agent will be further explored. However, the loss of fluorescence may also occur a result of ligand reduction or degradation.

4.3.7 Gold King Mine Water Samples

Water samples retrieved from various locations of the Gold King Mine with were tested on the chemometer designs. Two samples, one from the “Mill Lower Tunnel” (Al: 9.8 ppm, Fe: 96 ppm, Cu: 10 ppm) and the other from the “Plant Influent” (Al: 11 ppm, Fe: 32 ppm, Cu: 2.5 ppm) were used. Both samples had significant amounts of Fe(III) and Cu(II) to potentially interfere with the assay. ICP-MS analysis verified metal concentrations in these two samples. The complete list of metal concentrations is reported in Table S4.1. When using the two mine samples, a long, non-

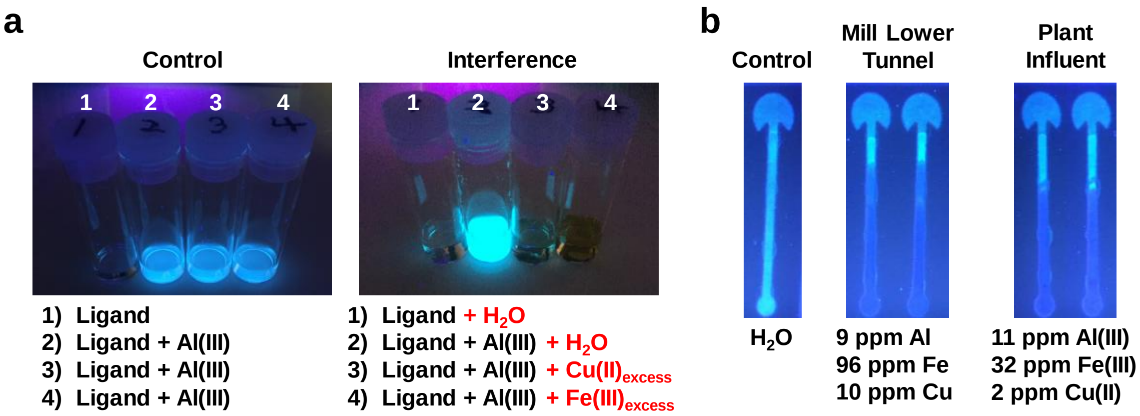

Figure 4.5. a) Photographs of solutions 1–4 before (left) and after the addition of Cu(II) and Fe(III) interferences (right) showing the turn-off of the fluorescent signal due to transmetallation of Al for the interference. **b)** Photographs of devices with blank (left), Mill Lower Tunnel (middle), and Plant Influent (right) from the Gold King Mine added with the resulting fluorescent responses.

fluorescent band is first observed at the inlet of the device, followed by the formation of a short fluorescent band. The assumption is that due to the stronger affinity of the interferences for the ligand, the interferences bind to the ligand first and once consumed, the Al(III) can bind to the ligand further along the device. This interference is shown in Figure 4.5b. It has been considered to use the lack of background fluorescence as a dual colorimetric (turn-off) sensor for Fe(III) or Cu(II). However, this sensor has two analytes that turn-off the fluorescence which make it difficult to understand which interference is responsible.

4.4 Conclusions

Simple distance-based colorimetric responses are ideal for designing user-friendly µPADs. Herein, the first two distance-based µPADs were developed for Al(III) detection using a carefully selected fluorescent detection motif. In addition to their simple readouts, the analytical operation for these two µPADs only requires a one-step sample addition step prior to analysis. The chemometer and radial devices do not require sample preconcentration or pretreatment prior for analysis. Requiring only simple fabrication techniques, these devices are also amenable for roll-to-roll processing manufacturing techniques. Once made, the devices are also air-stable and have a shelf life of at least 5 months. Between these two devices, the LOD for Al(III) is 0.9 ppm with a linear range from 2.7–54 ppm ($R^2 = 0.9898$). The LOD and linear range covers concentrations relevant to plant health. Despite all the benefits of this assay on these devices, a hindrance is that the detection ligand has a stronger affinity for Fe(III) and Cu(II), which also turn-off the fluorescent response. Future work will explore the use of more Fe(III) and Cu(II) specific chelating reagents and redox species to prevent preferential binding of the interferences for the ligand in the assay. Fortunately, when testing real samples from the Gold King Mine with high concentrations of interferences present, the devices managed to maintain distance responses that were proportional to the Al(III) concentration. This evidence provides promise for these devices to one day be commercially available to empower citizen scientists with powerful analytical tools.

REFERENCES

1. Valko, M.; Morris, H.; Cronin, M. T. D., Metals, Toxicity and Oxidative Stress. *Current Medicinal Chemistry* **2005,** *12* (10), 1161-1208.
2. Imel, N. D.; Marisol, C. B.; Timothy, D.; Kyle, S.; Marilyn, F.; Laura, P.; Annette, P. Ü.; James, L.; Carlos, C., The global burden of selected occupational diseases and injury risks: Methodology and summary. *American Journal of Industrial Medicine* **2005,** *48* (6), 400-418.
3. Panda, S. K.; Baluska, F.; Matsumoto, H., Aluminum stress signaling in plants. *Plant Signaling & Behavior* **2009,** *4* (7), 592-597.
4. (a) Murungi, J. I.; Robinson, J. W., Studies on the toxic effects of dissolved aluminum on plant growth alligator grass (alternthera philaxeroides). the modifying effects of pH, Humic substances and small quantities of cations (Ca, Mg, Fe). *Journal of Environmental Science and Health . Part A: Environmental Science and Engineering and Toxicology* **1992,** *27* (3), 735-746; (b) Inc, S. A. Soil Aluminum and Soil Test Interpretation. http://www.spectrumanalytic.com/support/library/ff/Soil_Aluminum_and_test_interpretation.htm (accessed 05/15/2018).
5. Vitorello, V. A.; Capaldi, F. R.; Stefanuto, V. A., Recent advances in aluminum toxicity and resistance in higher plants. *Brazilian Journal of Plant Physiology* **2005,** *17*, 129-143.
6. Joy, E. J. M.; Broadley, M. R.; Young, S. D.; Black, C. R.; Chilimba, A. D. C.; Ander, E. L.; Barlow, T. S.; Watts, M. J., Soil type influences crop mineral composition in Malawi. *Science of The Total Environment* **2015,** *505*, 587-595.

7. (a) Roller, P. S., Colorimetric Determination of Aluminum with Aurintricarboxylic Acid1. *Journal of the American Chemical Society* **1933,** *55* (6), 2437-2438; (b) Jurd, L.; Asen, S., The formation of metal and "co-pigment" complexes of cyanidin 3-glucoside. *Phytochemistry* **1966,** *5* (6), 1263-1271; (c) Moncada, M. C.; Moura, S.; Melo, M. J.; Roque, A.; Lodeiro, C.; Pina, F., Complexation of aluminum(III) by anthocyanins and synthetic flavylium salts: A source for blue and purple color. *Inorganica Chimica Acta* **2003,** *356*, 51-61; (d) Jisha, B.; Resmi, M. R.; Maya, R. J.; Varma, R. L., Colorimetric detection of Al(III) ions based on triethylene glycol appended 8-propyloxy quinoline ester. *Tetrahedron Letters* **2013,** *54* (32), 4232-4236.

8. Mulon, J.-B.; Destandau, É.; Alain, V.; Bardez, É., How can aluminium(III) generate fluorescence? *Journal of Inorganic Biochemistry* **2005,** *99* (9), 1749-1755.

9. Goppelsröder, F., Ueber eine fluorescirende Substanz aus dem Kubaholze. *Journal für Praktische Chemie* **1867,** *101* (1), 408-414.

10. (a) Fan, L.; Li, T.-r.; Wang, B.-d.; Yang, Z.-y.; Liu, C.-j., A colorimetric and turn-on fluorescent chemosensor for Al(III) based on a chromone Schiff-base. *Spectrochimica Acta Part A: Molecular and Biomolecular Spectroscopy* **2014,** *118*, 760-764; (b) Tian, J.; Yan, X.; Yang, H.; Tian, F., A novel turn-on Schiff-base fluorescent sensor for aluminum(iii) ions in living cells. *RSC Advances* **2015,** *5* (129), 107012-107019; (c) Liu, Z.; Xu, H.; Sheng, L.; Chen, S.; Huang, D.; Liu, J., A highly selective colorimetric and fluorescent chemosensor for Al(III) based-on simple naphthol in aqueous solution. *Spectrochimica Acta Part A: Molecular and Biomolecular Spectroscopy* **2016,** *157*, 6-10; (d) Kang, L.; Liu, Y.-T.; Li, N.-N.; Dang, Q.-X.; Xing, Z.-Y.; Li, J.-L.; Zhang, Y., A schiff-base receptor based naphthalimide derivative: Highly selective and colorimetric fluorescent turn-on

sensor for Al3+. *Journal of Luminescence* **2017,** *186,* 48-52; (e) Lashgari, N.; Badiei, A.; Mohammadi Ziarani, G., A Fluorescent Sensor for Al(III) and Colorimetric Sensor for Fe(III) and Fe(II) Based on a Novel 8-Hydroxyquinoline Derivative. *Journal of Fluorescence* **2016,** *26* (5), 1885-1894; (f) Pang, B.-j.; Li, C.-r.; Yang, Z.-y., Design of a colorimetric and turn-on fluorescent probe for the detection of Al(III). *Journal of Photochemistry and Photobiology A: Chemistry* **2018,** *356*, 159-165; (g) Yu, M.-H.; Hu, T.-L.; Bu, X.-H., A metal-organic framework as a "turn on" fluorescent sensor for aluminum ions. *Inorganic Chemistry Frontiers* **2017,** *4* (2), 256-260; (h) Xiao, N.; Xie, L.; Zhi, X.; Fang, C.-J., A naphthol-based highly selective fluorescence turn-on and reversible sensor for Al(III) ion. *Inorganic Chemistry Communications* **2018,** *89,* 13-17.

11. Yang, Y.; Noviana, E.; Nguyen, M. P.; Geiss, B. J.; Dandy, D. S.; Henry, C. S., Paper-Based Microfluidic Devices: Emerging Themes and Applications. *Analytical Chemistry* **2017,** *89* (1), 71-91.

12. Nguyen, M. P.; Meredith, N. A.; Kelly, S. P.; Henry, C. S., Design Considerations for Reducing Sample Loss in Microfluidic Paper-Based Analytical Devices. *Analytica Chimica Acta* **2018**.

13. Derby, B., Bioprinting: inkjet printing proteins and hybrid cell-containing materials and structures. *Journal of Materials Chemistry* **2008,** *18* (47), 5717-5721.

14. Guan, L.; Cao, R.; Tian, J.; McLiesh, H.; Garnier, G.; Shen, W., A preliminary study on the stabilization of blood typing antibodies sorbed into paper. *Cellulose* **2014,** *21* (1), 717-727.

15. Cate, D. M.; Dungchai, W.; Cunningham, J. C.; Volckens, J.; Henry, C. S., Simple, distance-based measurement for paper analytical devices. *Lab on a Chip* **2013,** *13* (12), 2397-2404.

16. Jayman, T. C. Z.; Sivasubramaniam, S., The use of ascorbic acid to eliminate interference from iron in the aluminon method for determining aluminium in plant and soil extracts. *Analyst* **1974,** *99* (1178), 296-301.

17. Jiang, X. C.; Chen, C. Y.; Chen, W. M.; Yu, A. B., Role of Citric Acid in the Formation of Silver Nanoplates through a Synergistic Reduction Approach. *Langmuir* **2010,** *26* (6), 4400-4408.

CHAPTER 5. CONCLUSIONS & PRELIMINARY DATA FOR FUTURE WORK

5.1 Chapter Overview

Criticisms of microfluidic paper-based analytical devices typically question their novelty and analytical performance. Herein this dissertation I identified major issues that contribute to these criticisms and demonstrate how I overcame many of them.

5.2 Sample Loss Implications

The most significant issue within the μPAD field is reaching low enough detection limits and high enough sensitivity to satisfy health and environmental standards. Sometimes simple off/on or high/low concentration distinctions are sufficient, however most often this is not the case. Sample being non-specifically adsorbed to the paper's fibers was identified as a major contributor to high detection limits and low sensitivity. In Chapter 2, I discussed my investigation of how design improvements and manipulations reduce sample loss and improve performance in μPADs.[2] I learned that physical design had a greater impact on device performance than the solution or surface chemistry. This work was not only useful toward my own understanding of how these devices should be designed for a given application, but also proved helpful for designing devices for others in the Henry group. I show how laser cut barrier devices as opposed to wax barriers increase fluid transport and decrease colorimetric signal intensity. The reaction kinetics are slow enough where the flow rate in single layer paper devices reduces reaction efficiency. The method to reduce fluid velocity was implemented in two recent publications from the Henry group where a distance-based format was applied to Cu(II) and K^+ determination.[1, 3] A photograph of the distance-based μPAD for Cu(II) determination that took advantage of the reduced fluid transport is shown in Figure 5.1A. The principles learned from this project were initially only applied to devices measuring inorganic ions. Next, the shorter paper channels and additional waste reservoir significantly improved colorimetric signal in a µPAD developed that detects ampicillin within an antibiotic purity project (unpublished results courtesy of Dr. Katherine Boehle). Improvements in the results are shown in Figure 5.1B.

Further proving this work's utility beyond environmental analysis, the washing manipulation described in Chapter 2, was employed for a coworker's µPAD for nitrite determination in human saliva samples. Here, they developed a µPAD to quantify nitrite as a non-invasive health biomarker for oral health screening. The issue faced was the variability in colorimetric signal caused by differences in salivary viscosity between individuals. Following the

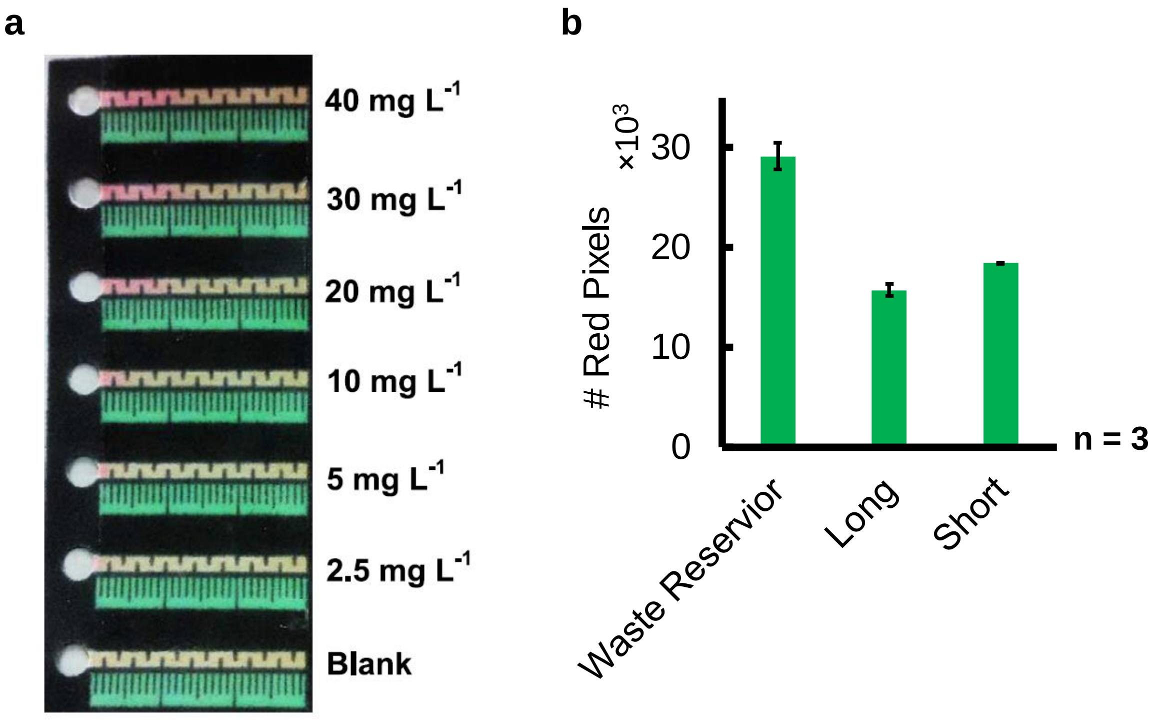

Figure 5.1. (a) Images with varying Cu(II) concentrations on distance-based µPADs[1] (b) Bar graphs showing red pixel intensity with various µPAD designs for detecting ampicillin (unpublished results).

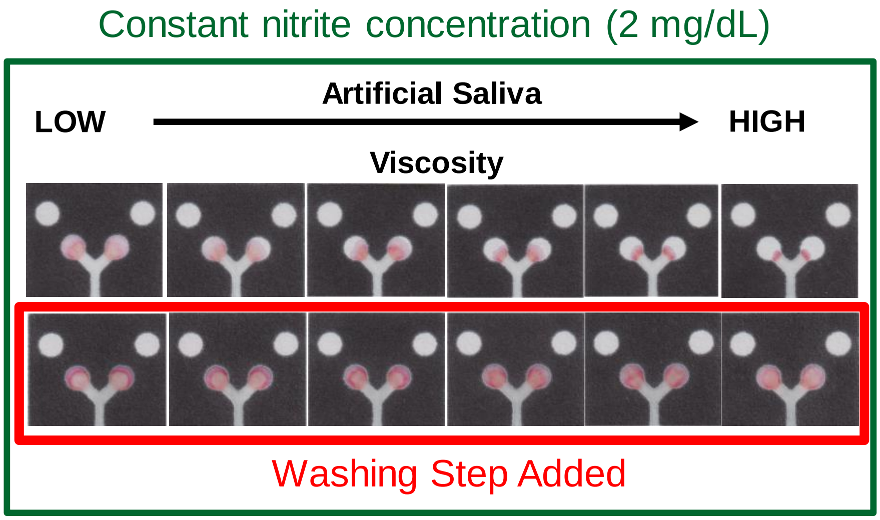

Figure 5.2. (Top) Images of μPADs with 2 mg/dL of nitrite with varying artificial saliva viscosity showing non-uniform color distribution. (Bottom) The same μPADs after the addition of a washing step showing the improved uniformity of color distribution (manuscript accepted in *Theranostics*).

suggestion of implementing a washing step and improving sample delivery to the detection zone, they found that the manipulation removed the variability in colorimetric signal. Photographs of the devices with and without a washing step is shown in Figure 5.2. This work was recently accepted for publication in a high-impact diagnostics journal.[4]

5.3 Al(III) μPAD Implications

As chemists, biologists, and engineers explore various μPAD designs for the detection of a host of analytes, the core to developing a high-performance μPAD is choosing the precise chemical reagents to drive the analysis. In Chapter 4, I demonstrated the performance benefits of careful reagent selection. In developing a simple and high-performance Al(III) measuring device, I explored my μPAD's commercialization and received interest from local sensor company, Access Sensor Technologies, to fund my project. My advisor and I submitted an invention disclosure on the assay to be used in a distance-based format. This work is currently being reviewed by Colorado State University’s intellectual property office, CSU Ventures, on its ability to be licensed to companies such as Access Sensor Technologies.

Aside from commercial applications, this technology is being applied to the development of a handheld absorbance and fluorescence device in collaboration with researchers at Michigan State University. The first generation of this device, the PhotosynQ, was developed for using absorbance to monitor plant health. Combined with a mobile phone application, the measurements can be read and recorded in real time. The second-generation device is currently being developed to quantify fluorescent analytes in addition to their absorbance. In Chapter 4, I described the failed attempt to make a read-by-eye spot test μPAD for the determining Al(III). If successfully developed, the second-generation PhotosynQ will sensitively detect changes in the fluorescence and measure lower detection limits than the current read-by-eye Al(III) μPAD. This technology would be very easily modified to detect luminescence on μPADs where camera phones failed to meet a given application’s sensitivity needs.

Figure 5.3. Photographs of PhotosynQ (left) and mobile phone application to view results in the field (Images from http://photosynq.org/).

5.4 Fast Flow Paper Device Implications

The slow flow rate of fluid transport in μPADs is caused by the capillary action inherent to paper. Slow flow rates increase analysis time and evaporation can limit long and complicated designs. In Chapter 3 I discussed the enhanced flow rate and improved performance metrics when using multilayer paper devices.[5] With the optimized multilayer design, I demonstrated a 168× increase in flow rate compared to single layer device motifs. While critically exploring factors that contributed this fast flow, I also established the ability tune the flow rate as well as improved assay complexity without increasing user input.

I exhibited, with the same sequential injection device, the utility of the multilayer design beyond transporting food dye down straight channels. The chronoamperometric detection of Fe(II) was first employed in the sequential injection device to improve analysis speed 66× compared to single layer paper devices. A Cd(II) assay was then applied to the sequential injection device that included an automatic and *in situ* electrode modification step, a washing step, and a detection step. This design increased the integrated peak current or sensitivity in an anodic stripping voltammetry measurement 5×.

5.5 Hybrid Devices

Previous single-layer μPADs struggled when flowing particles ≥ 5 μm. The new multilayer design proved effective for improving analytical performance metrics and was hypothesized to transport larger particles such as bacteria and microbeads due to the increased channel size (~200-500 μm). To test this hypothesis and image the particles that are being flowed, one layer of paper was replaced with packing tape. The layout is shown in Figure 5.4A. It was unclear if both layers in the device needed to be paper if a large channel height was maintained. Straight channel devices were constructed and tested confirming that fast flow properties were upheld in the new device layout. While maintaining a large, several hundred micron-sized gap with only one layer of paper, the fast flow was preserved. The high velocity fluid transport is shown in Figure 5.4B.

Prior to transporting micron sized particles through the device, laminar flow needed to be determined. In both traditional and paper microfluidics laminar flow is maintained.[6,7] A μPAD with a Y-shaped inlet and outlet was constructed to test if the multilayer device would also exhibit laminar flow properties. The inlet and outlet were connected by a 20 mm straight channel. The design is shown in Figure 5.5. A red and green colored food dye were pipetted into the inlets simultaneously and exhibited laminar flow shown in Figure 5.5A. The next step was testing if this laminar flow was maintained with a suspension of fluorescent microbeads. A microbead suspension and water were simultaneously pipetted on the device. A fluorescence microscopy image of the channel following the fluid transport demonstrated laminar flow just as with the food

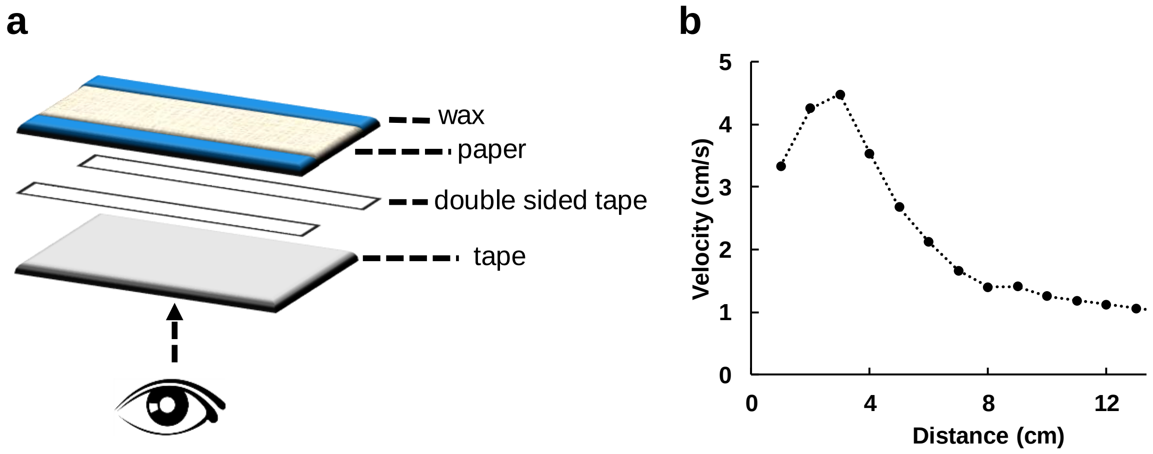

Figure 5.4. (a) Schematic of multilayer paper device with a packing tape layer to replace one of the paper layers (b) Velocity–distance plot showing the fast-flow properties maintained with this device design (unpublished results).

dye. The image in Figure 5.5B shows two distinct fluid paths with very little mixing at the interface where the two solutions met.

Prior to this result, only more traditional microfluidic methods have performed analyses and separations of larger particles.[8] This is particularly useful for situations when detecting sample of a particular size from complex matrices such as bacteria or viruses from blood.[9] Traditional microfluidic chips with the specific designs and phenomenon can separate particles based on size.[10,11] Herringbone and serpentine shaped features have shown to collect and separate particles.[12,13] Dean vortices also demonstrate the ability to separate particles in microfluidic devices.[10,11] These counter-directional vortices form when volumetric flow rates ($< \sim 1$ mL·min^{-1}) are employed in curved channels. With fast volumetric flow properties (~3.9 mL·min^{-1}) and the ability to transport large particles, it is possible to perform the same separations on paper.[5] The

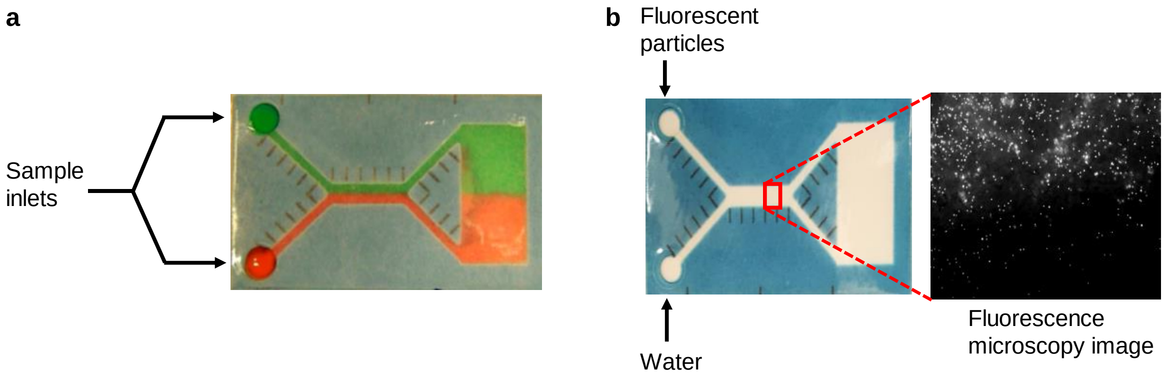

Figure 5.5. (a) Photograph of the Y-shaped μPAD after transporting green and yellow colored food dye (b) (left) Photograph of the Y-shaped μPAD after transporting fluorescent particles and water (right) fluorescence microscopy image of channel (unpublished results).

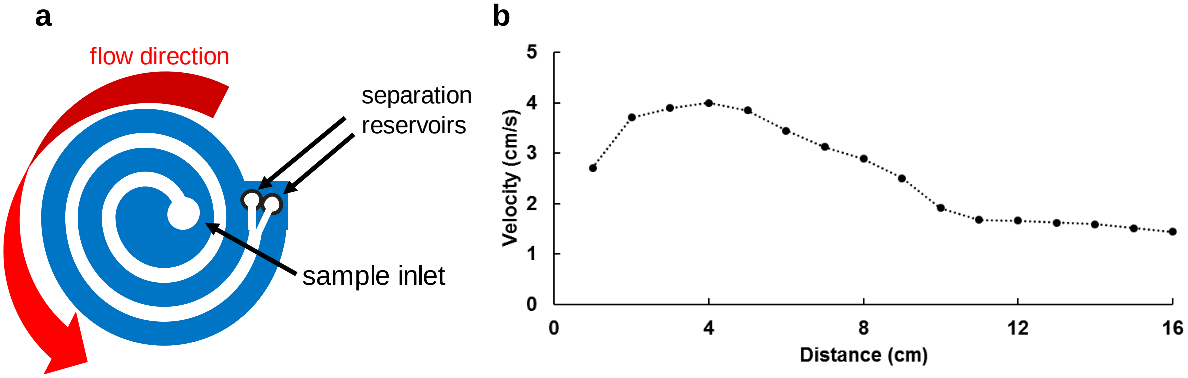

Figure 5.6. (a) Schematic of spiral shaped μPAD for size separation of particles (b) Velocity–distance plot showing the fast flow properties maintained in curved channels (unpublished results).

novelty to using paper-based devices to separate particles of interest is the use of passive flow as opposed to using bulky syringe pumps that require electricity. Therefore, this technology could provide analytical techniques in resource-limited settings. I first emulated the spiral shaped design that demonstrated the use of Dean vortices to separate particles to test if the separation predicted on paper is possible. I first used food dye, similar to the experiments using the Y-channel, demonstrating that the fast flow properties were maintained. In Figure 5.6, the device schematic and a velocity plot exhibiting fast flow in curved channels are provided. A solution containing fluorescent beads were added to the device determining if particles preferred either channel side after being transported 15 cm. Fluorescence microscopy images of the junction between the two microbead detection zones are shown in Figure 5.7. From these images, I counted the microbeads in their respective areas. The microbeads show a slight outer (right) edge channel preference with a particle count of 16 compared to the inner (left) edge of the channel with 6. The microbead concentration used was quite low, therefore I plan to reproduce this experiment with a much higher

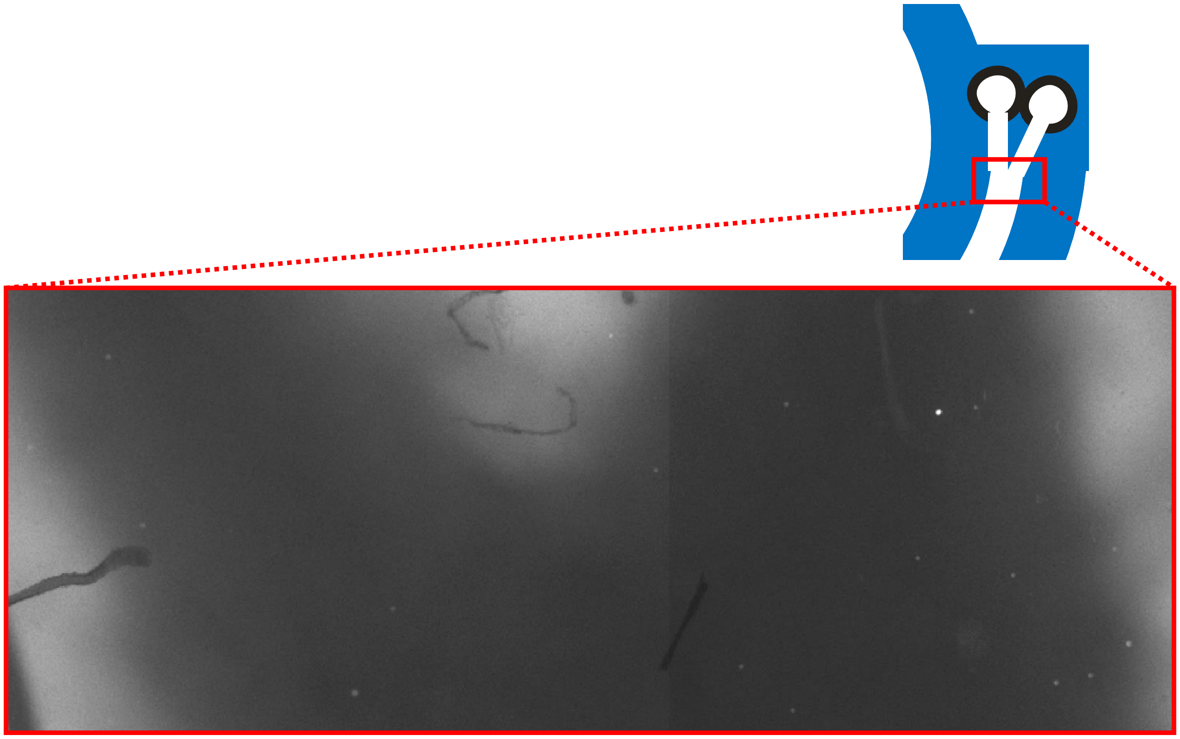

Figure 5.7. Fluorescence microscopy images stitched together at the junction between detection zones in spiral μPAD after fluorescent microbeads have been transported throughout the device (unpublished results).

microbead concentration potentially amplifying any separations that occur. I will also explore the microbead containing suspensions with varying size and emission to visualize if particle size separation occurs.

The last preliminary result that I came across with the multilayered paper devices was the observation that fast flow properties were volume-dependent. When a sample in the fluid reservoir was consumed and dry device segments remained, the fast flow turned-off. This was expected as an assumption of the Lucas-Washburn equation, referenced in Chapter 4, is that the fluid reservoir is unlimited.[7] However, what was unexpected was that when sample was resupplied to the fluid reservoir, the fast flow properties were re-established. The velocity-distance plot, provided in

Figure 5.8, illustrates the "turned-off" portion with a more constant velocity segment and the "turned-on" portion with an increasing slope segment. The implications will be explored for mixing and reaction-based applications. As demonstrated in Chapter 4, the multilayered fast flow devices show little mixing. For some applications this is desired, however, in situations where efficient hydration of dried reagents is required, this is not. Therefore, it is hypothesized that by controlling the volume, one can achieve both fast fluid transport and improved mixing in specific areas across a paper channel.

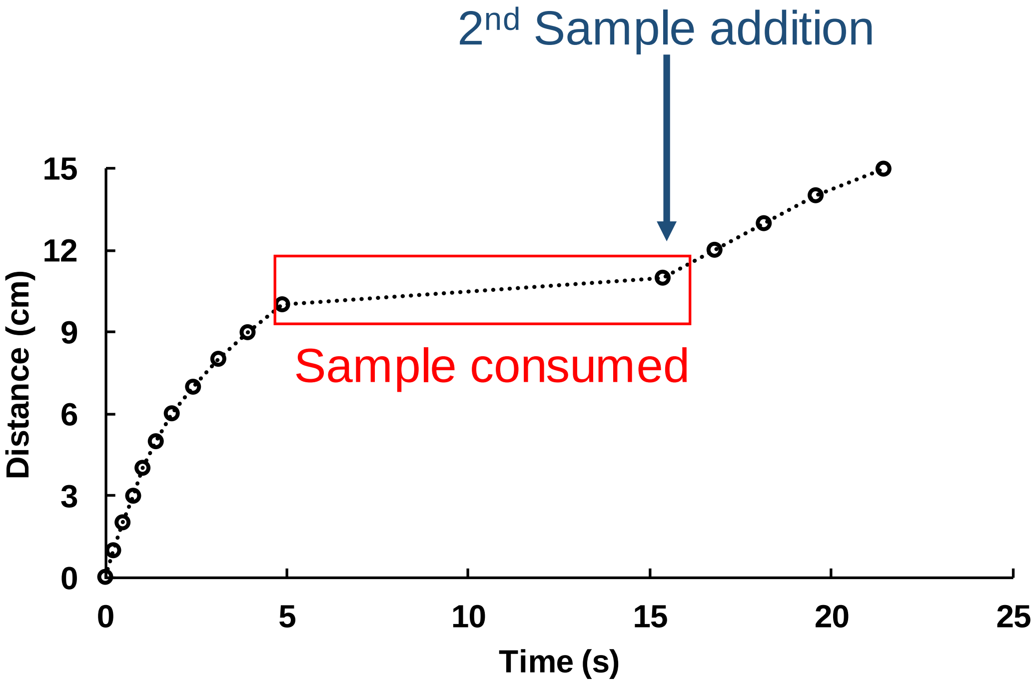

Figure 5.8. The distance–time plot showing the "off/on" fast flow properties related to sample volume (unpublished results).

5.6 Modeling Fluid Dynamics

The initial improvements in analytical performance metrics using multilayered microfluidic paper-based analytical devices is promising for progressing the field. Unfortunately, no current fluid dynamics models predict the fluid transport. Currently we are collaborating with

Professor David S. Dandy in Chemical and Biological Engineering department to model the observed behaviors. We aim to further develop the Martinez-LW equation to accurately model the fast flow properties in the multilayered system that consider variables such as channel width, device orientation, and channel height.[14]

The initial multilayer fast flow paper device project established promise in leaving a lasting impression on the field of microfluidic paper-based analytical devices. Further exploration of the multilayer paper device's design, utility, and mechanisms continue to yield new and exciting results. Each of the new results described above (1. single layer paper fast flow, 2. particle transport, 3. particle separation, 4. on/off fast flow, and 5. fast flow modeling) are all in their infancy stages, however, the preliminary data of each project point toward manuscript worthy endeavors. I am proud of my contributions toward this work and look forward to seeing how it may impact future sensor development.

REFERENCES

1. Pratiwi, R.; Nguyen, M. P.; Ibrahim, S.; Yoshioka, N.; Henry, C. S.; Tjahjono, D. H., A selective distance-based paper analytical device for copper(II) determination using a porphyrin derivative. *Talanta* **2017,** *174*, 493-499.
2. Nguyen, M. P.; Meredith, N. A.; Kelly, S. P.; Henry, C. S., Design Considerations for Reducing Sample Loss in Microfluidic Paper-Based Analytical Devices. *Analytica Chimica Acta* **2018**.
3. Gerold, C. T.; Bakker, E.; Henry, C. S., Selective Distance-Based K+ Quantification on Paper-Based Microfluidics. *Analytical Chemistry* **2018**.
4. Noiphung, J.; Nguyen, M. P.; Punyadeera, C.; Wan, Y.; Laiwattanapaisal, W.; Henry, C. S., Development of paper based analytical devices for minimizing the viscosity effect in human saliva. *Theranostics* **2018**.
5. Nguyen, M. P.; Channon, R. B.; Scorzelli, A. G.; Henry, E. M.; Volckens, J.; Dandy, D. S.; Henry, C. S., Rapid Flow in Multilayer Microfluidic Paper-Based Analytical Devices. *Lab on a Chip* **2018**.
6. Kamholz, A. E.; Weigl, B. H.; Finlayson, B. A.; Yager, P., Quantitative Analysis of Molecular Interaction in a Microfluidic Channel: The T-Sensor. *Analytical Chemistry* **1999,** *71* (23), 5340-5347.
7. Cate, D. M.; Adkins, J. A.; Mettakoonpitak, J.; Henry, C. S., Recent Developments in Paper-Based Microfluidic Devices. *Analytical Chemistry* **2015,** *87* (1), 19-41.
8. Nivedita, N.; Papautsky, I., Continuous separation of blood cells in spiral microfluidic devices. *Biomicrofluidics* **2013,** *7* (5), 054101.

9. Nivedita, N.; Garg, N.; Lee, A. P.; Papautsky, I., A high throughput microfluidic platform for size-selective enrichment of cell populations in tissue and blood samples. *Analyst* **2017,** *142* (14), 2558-2569.

10. Wang, X.; Liedert, C.; Liedert, R.; Papautsky, I., A disposable, roll-to-roll hot-embossed inertial microfluidic device for size-based sorting of microbeads and cells. *Lab on a Chip* **2016,** *16* (10), 1821-1830.

11. Nivedita, N.; Ligrani, P.; Papautsky, I., Dean Flow Dynamics in Low-Aspect Ratio Spiral Microchannels. *Scientific Reports* **2017,** *7*, 44072.

12. Lei, Z.; Zhigang, X.; Yuejun, K.; Peng, X., Three-dimensional microfluidic chip with twin-layer herringbone structure for high efficient tumor cell capture and release via antibody-conjugated magnetic microbeads. *ELECTROPHORESIS 0* (0).

13. Wang, L.; Dandy, D. S., High-Throughput Inertial Focusing of Micrometer- and Sub-Micrometer-Sized Particles Separation. *Advanced Science* **2017,** *4* (10), 1700153-n/a.

14. Camplisson, C. K.; Schilling, K. M.; Pedrotti, W. L.; Stone, H. A.; Martinez, A. W., Two-ply channels for faster wicking in paper-based microfluidic devices. *Lab on a Chip* **2015,** *15* (23), 4461-4466.

APPENDIX 1: EXPLORING SUBSTITUTED POLYPYRIDYL VANADIUM (II) CHROMOPHORES FOR OUTER-SPHERE PHOTOCATALYSIS

A1.1 Overview

Vanadium (II) polypyridyl complexes are being synthesized as chromophores for novel C–C bond forming schemes. Recent work has shown that Cr(III) polypyridyl complexes can photocatalyze Diels-Alder cycloadditions.[1] Toxicological impacts associated with chromium catalysts make the isoelectronic V(II) analogues worth pursuing. A possible advantage to using V(II) analogues to catalyze the same reactions is that they are much better visible light absorbers. Comparison of redox potentials for V(II) polypyridyl complexes points toward the need for strongly electron-withdrawing moieties to shift redox potentials more positive to be comparable with analogous Cr(III) complexes. The introduction of electron withdrawing groups to the ligands also allows for stable ligand radicals when reduced. The syntheses, crystal structures, electronic transitions, redox potentials, spectroelectrochemistry and emission spectra of these complexes will be presented. This work represents my progress while working under the supervision of Professor Matthew P. Shores.

A1.2 Introduction

The prospects for catalyst development aimed to activate small molecules is of interest for a variety of fields including pharmaceuticals and energy.[2] A sustainable way to accomplish this small molecule activation is to utilize photoredox catalysis.[3] Coordination complexes provide an avenue for light harvesting with tunable light absorption to increase molar absorptivity. One may also take advantage of metal to ligand charge transfer (MLCT) bands to promote electron-transfer. Coordination complexes also allow access to many redox states to drive single-electron steps.

These properties, when combined, provide good prospects for photoinduced-electron-transfer (PET). Few catalysts are comprised of first-row metals, are visible light-initiated, and have dual properties of being the chromophore and catalyst.[4] Currently the state of the art photocatalysts exist as Ru(II) and Ir(III) polypyridyl complexes.[3] To compete with second- and third-row molecular catalysts, the electron transfers steps are expected to be photoinduced ligand radical processes based on non-innocent ligands; we also employ various techniques to increase the molar absorptivity and extend the excited state lifetimes.[4]

Our overarching goal is to activate to C=X (X = O or N) substrates. One specific goal of this project is to mimic the work done by Ferreira and coworkers, who use coordinatively saturated Cr(III) complexes to photocatalytically drive Diels-Alder cyclization reactions with isoelectronic V(II) analogues.[1] These coordinatively saturated V(II) polypyridyl complexes are designed to perform outer-sphere electron transfer mechanisms. A variety of accessible oxidation states from −1 to +5 for vanadium allows for both oxidative and reductive chemistry.[5] Vanadium polypyridyl complexes also lend themselves to being great chromophores due to their enhanced visible light absorption from 320−750 nm; the isoelectronic Cr(III) analogues' absorptions, however, are shifted toward the ultraviolet region.[6]

Previous syntheses for $[V(bpy)_3]^{2+}$ and other complexes with substitutions on the 4,4' positions on the bipyridine ligand have been reported.[7,8,9] Herzog explored methods to synthesize $[V(bpy)_3]^X$ (X = −1, 0, +2) complexes beginning in the 1950's however the details in making the $[V(H_2O)_6](SO_4)$ starting material were unclear. The first structural X-ray data for the zero-valent $[V(bpy)_3]$ complex was collected by Albrecht, elucidating the coordination environment around the metal center.[10] The full structure however, could not be resolved.[9,10] Maverick was able to perform anion exchanges with Herzog's $[V(bpy)_3]^{2+}$ perchlorate and iodide salts for triflate anions in 1986.[8] Maverick completed a flash photolysis study of the complex displaying a 500 ps excited state lifetime. No static emission data was reported. Kinetic arguments have been made that excited state lifetimes must surpass 10^{-9} s to interact with substrates.[11] The $[V(H_2O)_6](SO_4)$ synthesis was later revisited and a better synthesis description developed by Cotton.[12] This allowed for the successful synthesis of the starting material however, the synthesis for the $[V(bpy)_3](O_3SCF_3)_2$ complex has not been attempted. The di-valent complex was again studied in 2012 by Wieghardt who used a sodium amalgam reduction of $[V(^{t}bpy)_3]^{3+}$ (^{t}bpy = 4,4'-di-tert-butyl-2,2'-bipyridine) to the zero-valent analogue and selectively oxidized the di-valent analogue.[9] Failed attempts to reproduce the same results caused me to discontinue work on this synthetic method. As a result, I explored two other vanadium (II) starting materials, $[V(CH_3CN)_6](BPh_4)_2$ and $[VCl_2(TMEDA)_2]$ (TMEDA = *N*,*N*,*N′*,*N′*-tetramethylethane-1,2-diamine) that were employed to carry out the synthesis discussed below.[13,14]

A1.3 Experimental Section

A1.3.1 Preparation of Compounds

Unless otherwise noted, compound manipulations and syntheses were performed either inside an argon-filled glovebox (MBRAUN Labmaster SP) or via Schlenk techniques under an inert atmosphere (N_2 or argon). All solvents were sparged with dinitrogen, passed over molecular sieves, and degassed prior to use. All of the following commercially available reagents were used as received without further purification: 2,2' bipyridine (bpy), 4,4'-dimethyl-2,2'-bipyridine (dmb), VCl_3, $VO(SO_4)$, and $NaBPh_4$. The following compounds were synthesized according to literature methods: dimethyl 2,2'-bipyridine-4,4'-dicarboxylate (4-dmcbpy), $[VCl_2(TMEDA)_2]$, $[V(H_2O)_6](SO_4)$, $[V(CH_3CN)_6](BPh_4)_2$ and $[V(bpy)_2SO_4]$.[12,13,14,15,16]

$[V(dmb)_3](BPh_4)_2$ (**1**). A suspension of $[V(CH_3CN)_6](BPh_4)_2$ (17 mg, 0.018 mmol) in 5 mL of acetonitrile was added to a solution of 4,4’-dimethyl-2,2’-bipyridine (dmb) (11 mg, 0.060 mmol) in 1 mL of acetonitrile. The reaction mixture color turned dark blue-green within a few minutes and was stirred for seven hours to complete the reaction. The reaction mixture was then filtered with a 2 μm pore sized syringe filter and a slow-vapor diffusion with diethyl ether was used to crystallize out very thin dark blue needle-like crystals of the complex. The crystals were washed with three portions (3 x 5 mL) of diethyl ether and then dried in vacuo. The crystallization afforded 19 mg (84 %) of product. Absorption spectrum (CH_3CN): 653 nm (λ_{max}) and 411 nm. Anal. Calcd for $VB_2C_{84}H_{76}N_6$: C, 81.20; H, 6.17; N, 6.77. Found: C, 80.42; H, 6.06; N, 6.41. Calcd for **1**·Et_2O: C, 80.30; H, 6.59; N, 6.38.

$[V(bpy)_3](BPh_4)_2$ (**2**). A suspension of $[V(CH_3CN)_6](BPh_4)_2$ (17 mg, 0.018 mmol) in 5 mL of acetonitrile was added to a solution of 2,2’-bipyridine (bpy) (9 mg, 0.06 mmol) in 1 mL of acetonitrile. The reaction mixture color turned dark blue-green within a few minutes and was stirred for seven hours to ensure completeness of the reaction. The reaction mixture was then filtered with a 2 μm pore sized syringe filter and a slow-vapor diffusion with diethyl ether was used to crystallize out very thin dark blue needle-like crystals of the complex. The crystals were washed with three portions (3 x 5 mL) of diethyl ether and then dried in vacuo. The crystallization afforded 10 mg (47 %) of product. Absorption spectrum (CH_3CN): 642 nm (11,387 $M^{-1}cm^{-1}$, λ_{max}) and 401 nm. Anal. Calcd for $VB_2C_{78}H_{64}N_6$: C, 80.90; H, 5.57; N, 7.26. Found: C, 80.19; H, 5.57; N, 7.20. Calcd for **2**·Et_2O: C, 79.94; H, 6.05; N, 6.82. Calcd for **2**·CH_3CN: C, 80.14; H, 5.63; N, 8.18.

[V(4-dmcbpy)$_3$](BPh$_4$)$_2$ (**3**). A solution of [V(CH$_3$CN)$_6$](BPh$_4$)$_2$ (58 mg, 0.062 mmol) in 12 mL of dichloromethane was added to a suspension of dimethyl 2,2'-bipyridine-4,4'-dicarboxylate (4-dmcbpy) (52 mg, 0.19 mmol) in 2 mL of dichloromethane. The reaction mixture color turned dark blue-green within a few minutes and was stirred for seven hours to ensure completeness of the reaction. The reaction mixture was then filtered through a 2 μm sized nylon filter and dried in vacuo. The solid was dissolved with acetonitrile and filtered with a 2 μm pore sized syringe filter to remove excess ligand. The product was dried in vacuo to collect 31 mg (33 %) of a green powder. Absorption spectrum (CH$_3$CN): 699 nm (λ_{max}) and 451 nm. Anal. Calcd for VB$_2$O$_{12}$C$_{90}$H$_{76}$N$_6$: C, 71.77; H, 5.09; N, 5.58. Found: C, 68.15; H, 4.98; N, 6.83. Calcd for **2**·2 CH$_3$CN•CH$_2$Cl$_2$: C, 68.19; H, 5.06; N, 6.70.

[V(4-dmcbpy)$_3$](BPh$_4$) (**4**). A solution of [VCl$_2$(TMEDA)$_2$] (56 mg, 0.16 mmol) in 10 mL of dichloromethane was added to a suspension of 4-dmcbpy (149 mg, 0.547 mmol) in 8 mL of dichloromethane. The reaction mixture color turned dark blue within a minute and was stirred for 18 hours to ensure completeness of the reaction. The mixture was filtered through a 2 μm pore sized nylon filter and dried in vacuo to collect a bright blue colored [V(4-dmcbpy)$_3$]Cl (204 mg, 0.226 mmol). A solution of the assumed [V(4-dmcbpy)$_3$]Cl complex in methanol was dropwise added to a solution of NaBPh$_4$ (300 mg, 0.877 mmol) in methanol to precipitate [V(4-dmcbpy)$_3$](BPh$_4$) (105 mg, 0.0885 mmol). The product was dissolved in 6 mL of dichloromethane and placed into a petroleum ether vapor diffusion to afford 66 mg (35 %) crystals of [V(4-dmcbpy)$_3$](BPh$_4$). Absorption spectrum (CH$_2$Cl$_2$): 890nm (λ_{max}) and 616 nm.

A1.3.2 X-Ray Structure Determinations

Crystals of **2** and **4** were suitable for X-ray analysis; the crystals were coated with Paratone-N oil and supported on a Cryoloop before being mounted on a *Bruker Kappa Apex II CCD* diffractometer under a stream of dinitrogen. Data collection was performed at 120 K with Mo Kα radiation and a graphite monochromator, targeting complete coverage and four-fold redundancy. Initial lattice parameters were determined from a minimum of 112 reflections harvested from 36 frames; these parameters were later refined against all data. The data was integrated and corrected for absorption effects with the Apex 2 software.[17] Structures were solved by direct methods and refined against F^2 with the SHELXTL Version 6.14 software package.[18] Thermal parameters for all non-hydrogen atoms were refined anisotropically. Hydrogen atoms were added at the ideal positions and refined using a riding model in which the isotropic displacement parameters were set at 1.2× those of the attached carbon atom (1.5× for the methyl carbons).

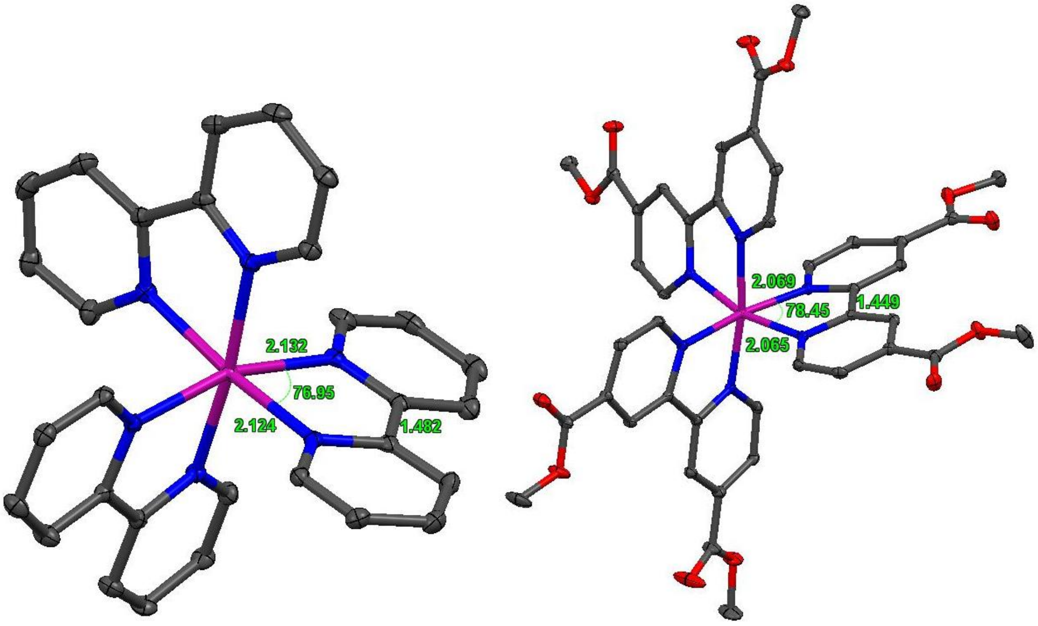

Figure A1.1. The crystal structure of **2**, [V(bpy)$_3$](BPh$_4$)$_2$ and **4**, [V(4-dmcbpy)$_3$](BPh$_4$). Thermal ellipsoids shown with 30% probability. The (BPh$_4$)$^-$ anions and hydrogen atoms were removed for clarity. Purple, blue, grey, and red colored atoms are vanadium, nitrogen, carbon and oxygen, respectively.

Table 1. Crystallographic data for **2** and **4.**

	2	**4**
formula	$VB_2C_{78}H_{64}N_6$	$VBO_{12}C_{66}H_{56}N_6$
fw	1157.97	1186.96
color, habit	dark blue rhombuses	dark blue needles
T, K	120(2)	120(2)
space group	$P2_1c$	$P\bar{1}$
Z	4	1
a, Å	12.3773(7)	11.0725(13)
b, Å	14.6602(9)	16.0641(17)
c, Å	34.086(2)	16.5649(19)
α, deg	90	79.306(6)
β, deg	98.180(2)	79.154(6)
γ, deg	90	84.336(6)
V, $Å^3$	6122.09	2837.29
GOOF	1.139	0.901
R_1 (wR_2)	0.0375 (0.1491)	0.0437 (0.1091)

A1.3.3 Photophysical Methods

The static emission of the complexes were compared to that of a known concentration of $[Ru(bpy)_3]Cl_2$ in room temperature acetonitrile with a *Horiba Fluorolog* fluorimeter. This was done to compare how scanning the excitation wavelength while monitoring a single emission wavelength should match the absorption spectrum shown in Figure A1.2. Slit widths for the excitation radiation are typically 5 nm while the slit widths for the emission radiation range from 5−15 nm. To check that the emission profiles were not artifacts of scattering events, the solutions were first filtered through a 2 µm filter to remove any undissolved particles. In order to show the emission signals were not features of Raman scattering the excitation wavelengths were also varied 10 nm on both sides of the excitation wavelength and checked that the emission maxima did not shift linearly.[19] Both the solvents and ligands were screened to check that the emission came from the vanadium complexes. The Stern-Volmer quenching study was completed first by taking the emission of **2**, and then the air-tight cuvette was brought into a glove box where a standardized

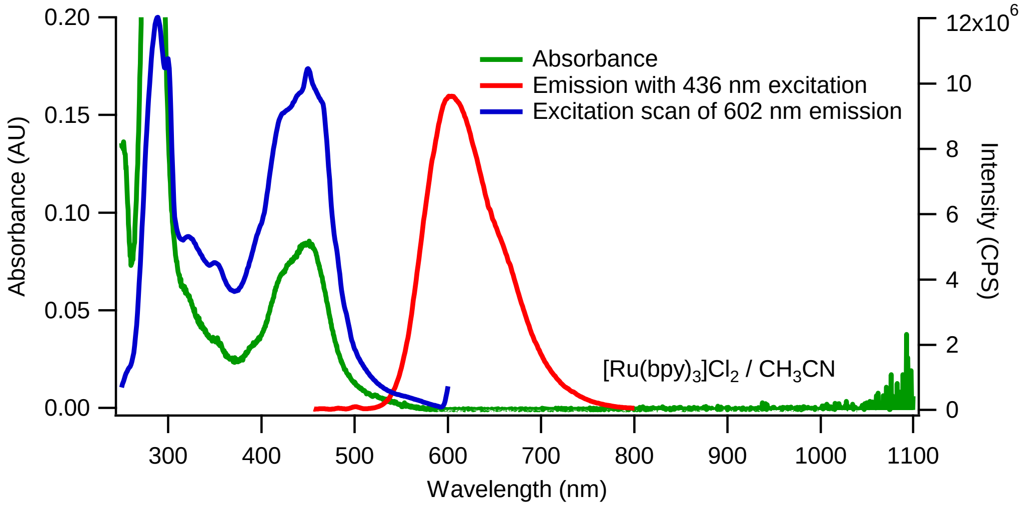

Figure A1.2. The absorbance spectrum, emission spectrum, and the excitation scan of $[Ru(bpy)_3]Cl_2$ in acetonitrile.

solution of bipyridine was added to the sample and the emission was re-measured. This titration process was repeated until the emission profile stopped changing.

A1.3.4 Other Physical Methods

Absorption spectra were obtained with either an *Agilent 8453* spectrophotometer in air-free quartz cuvette with a 1 cm path length or with an *Ocean Optics DH-2000-BAL* dip-probe spectrophotometer with a 1 cm path length under an argon atmosphere; all experiments were performed at room temperature. Cyclic voltammetry (CV) experiments were carried out inside an argon filled glovebox at 0.1 M solutions of electrochemistry grade $(Bu_4N)PF_6$ in acetonitrile. The voltammograms were recorded with a *Gamry Reference 600* potentiostat using a 1 mm diameter disc glassy carbon working electrode, a platinum coated titanium rod counter electrode and a Ag/AgCl leakless reference electrode all purchased from *eDAQ*. Reported potentials are referenced to the ferrocenium/ferrocene (Fc^+/Fc) redox couple. All of these cyclic voltammograms were recorded by first scanning cathodically from a potential more positive than the first reduction. Elemental analyses were performed by *Robertson Microlit Laboratories, Inc.* in Madison, NJ. To accomplish the spectroelectrochemistry measurements, a gold honeycomb electrode served as the working electrode while still allowing for light to pass through the sample to collect absorption data with the dip-probe spectrophotometer described above. The absorption data was first collected by taking an absorption spectrum of $[V(bpy)_3]^{2+}$ prior to applying a potential. The absorptions of the reduced species were collected by holding cathodic potentials more negative than the reduction maxima; the spectra were collected once the absorption stopped changing.

A1.4. Results and Discussion

A1.4.1 Synthesis of V(II) Complexes

The syntheses for **1−3,** described in Scheme 1, are completed under an argon atmosphere in acetonitrile or dichloromethane where a solution of the vanadium starting material is dropwise added to a stirred solution of the appropriate ligand. The 4-dmcbpy ligand is less soluble in acetonitrile as the bpy and dmb ligands therefore dichloromethane was used as the solvent. Although there is literature precedence for synthesizing $[V(bpy)_3]^{2+}$, the tetraphenylborate salts have not been studied and this salt has allowed for the first single-crystal X-ray structural data being collected for a $[V(bpy)_3]^{2+}$ complex; the structure can be seen in Figure A1.1 and the X-ray data can be seen in Tables 1 and 2. The crystals of **2** are grown by the slow diffusion of diethyl ether into an acetonitrile solution of the complex. Complex **1** can be crystallized in the same fashion however the crystals are not X-ray diffraction quality. Complex **3** will precipitate out of solution in these conditions but crystals have not yet formed. The synthesis of **4**, shown in Scheme 2, was performed with $[VCl_2(TMEDA)_2]$. The reduced species formation is believed to undergo reductive quenching after a photoexcitation event. This reductive quenching mechanism believed to occur, however, the reduction potential of triethylamine (0.7 V vs Fc^+/Fc) does not have enough reducing potential on its own to reduce the ligand (−0.985 V vs Fc^+/Fc) on its own.[20] This suggests

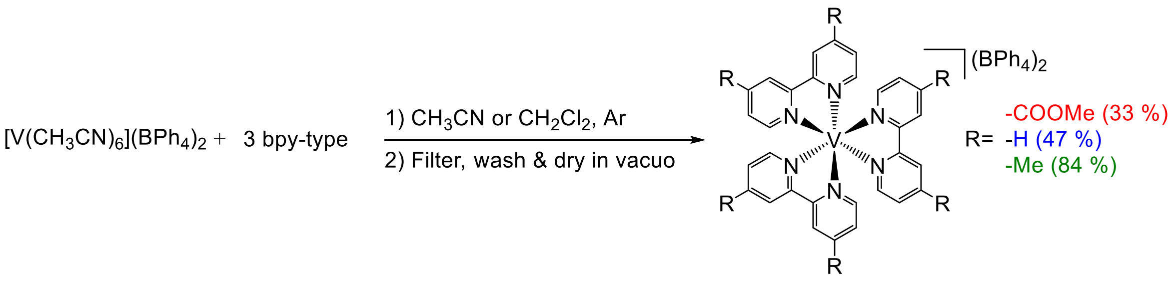

Scheme A1.1. The synthesis of **1**–**3** with the $[V(CH_3CN)_6](BPh_4)_2$ starting material and their respective percent yields.

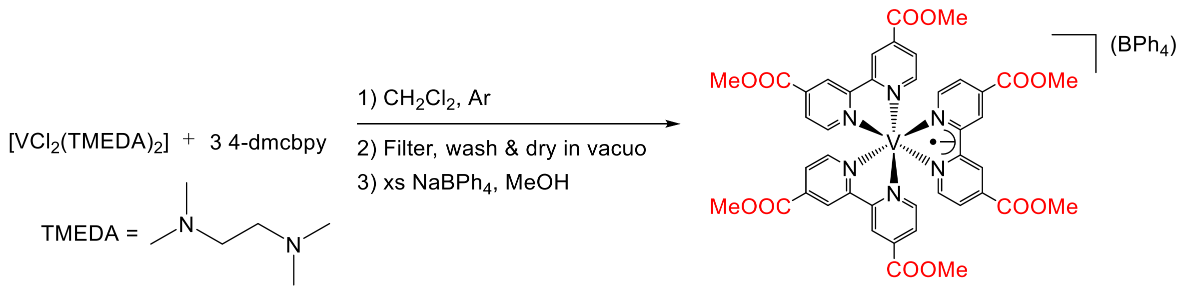

Scheme A1.2. The synthesis of **4** with the [VCl$_2$(TMEDA)$_2$] starting material.

that some external energy such as light is needed to promote this reduction. This type of reductive quenching is seen with [Ru(bpy)$_3$]$^{2+}$ photochemistry.[19] At this point, this is just a hypothesis that needs more experiments to test. The synthesis of **4** is not reproducible in acetonitrile possibly due to decomposition of the product during the reaction. It should be noted that in solution, **1** and **2** can also be made from this same starting material as observed by the absorption spectra and the cyclic voltammetry experiments however crystalline product has not been isolated. X-ray quality crystals of complex 4 were produced from a slow-evaporation of dichloromethane with petroleum ether but co-crystallization of an unknown colorless side-product. More experiments are necessary to identify this unknown product.

A1.4.2 Structural X-Ray Analysis

The crystal structures of **2** and **4** were both determined by single-crystal X-ray crystallography at cryogenic (120 K) temperature. Table 2 shows the average V−N and C$_{\text{pyridine}}$−C$_{\text{pyridine}}$ bond distances for both **2** and **4**. For **2**, the oxidation state of the ligands are neutral with a V(II) metal center. This is shown by the two (BPh$_4$)$^-$ anions in the structure. The ligands were determined to be neutral by observing that the V−N bond distances average to 2.13 Å with a standard deviation of 0.006 Å. Evidence for neutral ligands is also in the C$_{\text{pyridine}}$−C$_{\text{pyridine}}$ bond distance average of 1.48 Å with a standard deviation of 0.004 Å. The crystal structure of **4** is more unique. The average V−N bond distance is 2.09 Å but the standard deviation is 0.018 Å. The average $C_{pyridine}$−$C_{pyridine}$ bond distance is 1.46 Å with a standard deviation of 0.015 Å. The high standard deviations for the bond distance of **4** when compared to **2** were telling that something was unique. On closer inspection, there is a unique 4-dmcbpy ligand where the V−N and C−C bond distances are shorter than the other ligands. The bonds on this unique ligand are also much shorter than the averages for **2**. In the structure of **4**, only one $(BPh_4)^-$ is observed suggesting either a reduced V(I) center or a V(II) center with a ligand radical. Based on the unique ligand, the latter is assumed to be the culprit.

Wieghardt has shown that a difference between a Cr(III)−N bond distances outside the 3σ limit (≥ 0.056 Å), there is more electron density between the nitrogen atoms of the bipyridine unit.[21] The average V−N bond distance of the unique ligand on **4** is 0.061 Å different than that of the **2** providing evidence for a stable ligand radical on the ligand. Wieghardt also calculated that the radical is likely to reside between the nitrogen atoms between the pyridine rings.[21] While **2** and **4** are the first tris-bpy V(II) complexes to have fully solved structures, the structure of **4** is the first

Table 2. Selected bond length averages for **2** and **4**.

	$[V(4dmcbpy)_3](BPh_4)$	**$[V(bpy)_3](BPh_4)_2$**
Avg. V–N (Å)	2.090	2.132
Std. Dev N–N (Å)	0.019	0.006
Avg.$C_{pyridine}$–$C_{pyridine}$ (Å)	1.464	1.478
Std. Dev. $C_{pyridine}$–$C_{pyridine}$ (Å)	0.015	0.004

to show stable ligand radicals. In **4**’s ligands, the electron-withdrawing methyl-ester groups placed in the 4 and 4’ positions on the bipyridine unit appear to be sufficiently electron-withdrawing to stabilize ligand radicals.

A1.4.3 Electrochemistry

Cyclic voltammograms (CVs) for **1**−**4** are shown in Figure A1.3. Each of the V(II) complexes undergoes at least three ligand-based reductions in the acetonitrile solvent window. Tables of these redox potentials are shown in Table 3. In the case of **3** and **4**, six redox events appear but the $2^+/1^+$ and $1^+/0$ couple seem to be occurring so closely that they are less resolved

Table A1.3. Redox couples for **1**–**3** and other related complexes (irr = irreversible).

	$3^+/2^+$ (V)	**$2^+/1^+$ (V)**	**$1^+/0$ (V)**	**$0/1^-$ (V)**	**$1^-/2^-$ (V)**	**$2^-/3^-$ (V)**	**$3^-/4^-$ (V)**
$[V(4\text{-dmcbpy})_3]^{2+}$	–	–0.985	–1.09	–1.47	–1.91	–2.19	-2.47
$[V(bpy)_3]^{2+}$	–	–1.51	–1.63	–2.07	–	–	–
$[V(dmb)_3]^{2+}$	–	–1.63	–1.77	–2.13	–	–	–
(9) $[V(bpy)_3]$	0.077	–1.41	–1.51	–2.05	–2.73	–	–
(9) $[V(^t\text{bpy})_3]$	0.80_{irr}	–1.66	–1.78	–2.38	-2.79_{irr}	–	–
(6) $[Cr(bpy)_3]^{3+}$	– 0.529	–1.02	–1.52	–2.15	–2.51	–2.75	–
(22) $[Ru(bpy)_3]^{2+}$	–	–1.61	–	–2.07	–	–	–

when first reducing. The extra three reductions are shown to be ligand based for Ru(II) and Cr(III) analogues containing three 4-dmcbpy ligands and Cr(III).[6,22] The methyl-ester groups of **3** and **4** on the 4,4'-positions of the bipyridine unit shift the first reduction 500 mV to more positive potentials than the non-substituted **2.** The analogous Cr(III) comparison only observes a 270 mV shift to more positive potentials.[6] This ability to significantly tune the $2^+/1^+$ redox couple by placing electron-withdrawing groups in the para-positons of the pyridine in V(II) complexes shows good prospects for also their tuning excited state potentials with applications for photoredox catalysis. The effect of the electron-donating methyl groups in the same positions on the ligand in **1** shift the first reduction 120 mV to more negative potentials than **2.** The analogous Cr(III)

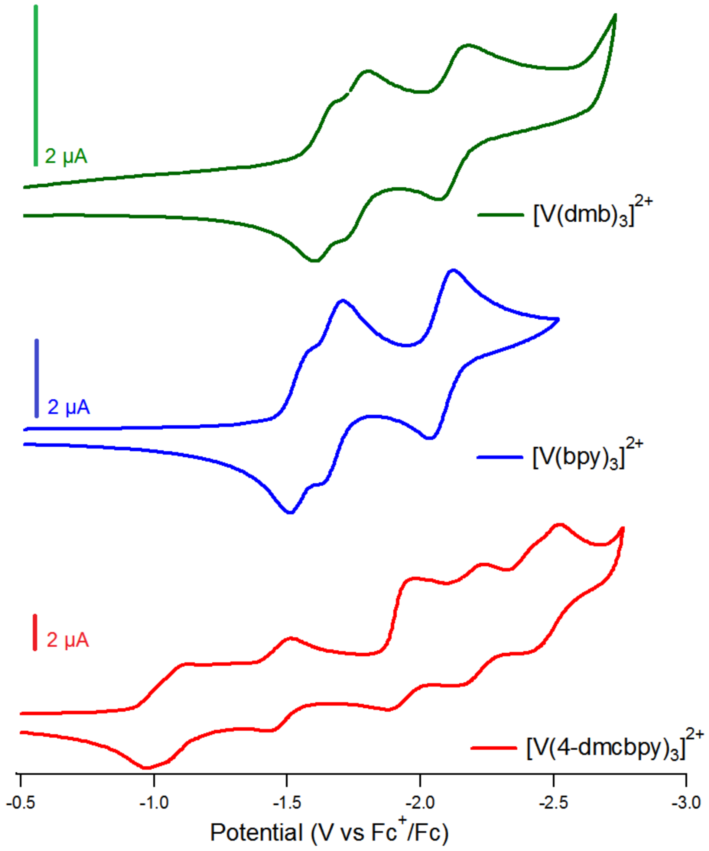

Figure A1.3. The cyclic voltammograms for **1**–**3** in acetonitrile.

comparison observes a 140 mV shift to more negative potentials.[6] The comparison for tuning the $2^+/1^+$ redox couple with electron-withdrawing groups in V(II) complexes does not show an enhancement over Cr(III) complexes. It should be noted that the redox potentials for the $(BPh_4)^-$ salts do not match the zero-valent parent complexes. The substitutions of electron-withdrawing and electron donating groups in the 4,4'-positions of the bipyridine unit, however, do agree with Cr(III) trends.[6] Each of these redox processes also appear to be one-electron processes based on the reduction and corresponding oxidation peak separation.

A1.4.4 Electronic Absorption

The electronic absorption spectra for the discussed complexes in acetonitrile are given in Figure A1.4. For complex **2**, the molar absorptivity is 11,387 $M^{-1}cm^{-1}$ (646 nm, CH_3CN) which does not agree with literature where the molar absorptivity for $[V(bpy)_3](O_3SCF_3)_2$ is 5700 $M^{-1}cm^{-1}$ (660 nm, CH_3CN).[8] The effect of the $(BPh_4)^-$ anion on the absorption appears to be significant by nearly doubling the molar absorptivity. The larger molar absorptivity is comparable with that of $[Ru(bpy)_3]Cl_2$ which is 14,600 $M^{-1}cm^{-1}$ (452 nm, CH_3CN).[23] The molar absorptivity value for the 646 nm transition in **2** indicates this transition is likely due to a charge transfer band versus a d–d transition which would have a much lower value. The methyl group substitution in **1** does not play a large role in the absorption peak positions when compared to **2**. However, with the methyl ester groups in the 4,4'- positions in complex **3**, the absorptions are red-shifted ~50 nm but still maintain the same shape. More evidence for a ligand radical but in solution is observed in **4**, with a new broad absorption feature that extends past 1000 nm. This is most likely due to a ligand radical on the bpy ligand similar to the growth of a broad absorbance in Cr(III) complexes demonstrated by our group.[24]

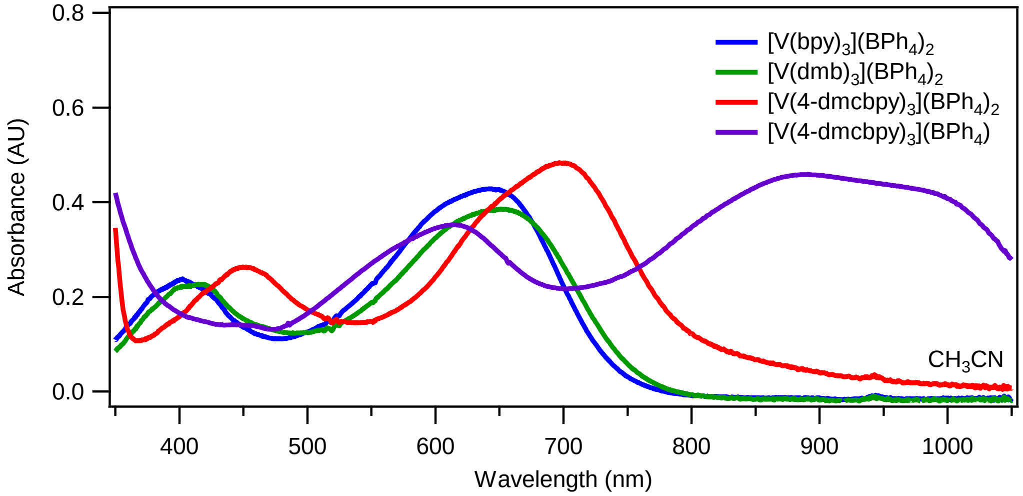

Figure A1.4. The electronic absorption spectra of **1**–**4** in acetonitrile.

A1.4.5 Spectroelectrochemistry

Our spectroelectrochemistry experiment shown in Figure A1.5, allow us to probe the electronic absorption of the electrochemically reduced or oxidized species. Using **2**, we were able to compare how the different absorbance spectra of the 2^+, 1^+, 0 and 1^- species change and compare to the absorbance of the chemically reduced complex, **4**. The original 461 and 641 nm absorption features of $[V(bpy)_3]^{2+}$species show a decreased absorbance when the complex is singly reduced; an in increase in the absorption at 476 and 815 nm is observed for the singly reduced species. These new absorption features are much broader than the di-valent species. The doubly reduced species shows an increase in the original 461 nm feature along with new 588 and 938 nm features that are observed. The absorption of the doubly reduced species, $[V(bpy)_3]^0$, species agrees much better with the absorption of **4** than the singly reduced species, $[V(bpy)_3]^{1+}$. Finally in the triply reduced species, the absorptions show slight similarity to the di-valent species but with a much lower intensity of absorption.

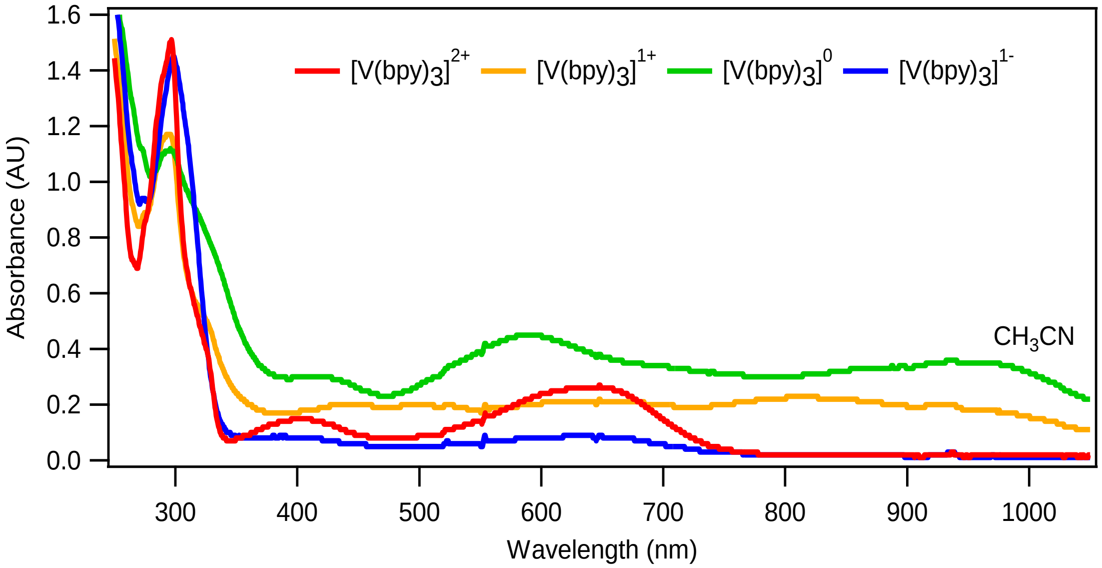

Figure A1.5. The absorbance spectra of **1** from various electrochemically produced oxidation states.

A1.4.6 Static Emission

Complexes **1**–**4** are emissive at room temperature when excited by visible light. However the focus of this emission study was on the emission profiles of **1** and **2**. In the case of **1**, the excitation of 528 nm produced an emission at 622 nm shown in Figure A1.6. For **2**, a similar excitation of 530 nm allowed for a 626 nm emission Figure A1.7. What was not expected is that the most intense emissions for complexes **1** and **2** lie within the maxima of the absorption bands while the excitations lie in the minima of the absorption band.

To probe the source of the emission, excitation scans of complexes were measured. In **1** and **2**, neither of the excitation scans matched the absorption spectra for their respective complex. This suggests that the emissive species is not the same as the species being measured in the absorption spectrum. To further probe the emission origin, the solution was first diluted by a half but a proportional loss of the emission intensity was also lost. This reduced some suspicions of some intermolecular processes occurring that would have caused the emission. A quenching study was then employed by the titration of bpy into the sample solution to test whether or not ligands could be dissociating in solution is shown in Figure A1.8. From this quenching study, a Stern-Volmer plot was constructed showing a linear dependence of the emission loss on the ligand concentration shown in Figure A1.9. This linear dependence is evidence for the bpy ligand quenching the emission. What is still unclear is whether the bpy ligand is quenching staticly or dynamically. In a static quenching model, the bpy ligand in solution may bind to a presumed $[V(bpy)_2X_2]^{2+}$ (X = solvent) molecule where the true $[V(bpy)_3]^{2+}$ species is not emissive. In a dynamic quenching model, the excited state of the believed $[V(bpy)_3]^{2+}$ can undergo an electron or energy transfer to the bpy ligand after collision also causing for a loss of the emission signal. To support a static quenching model, a heteroleptic system is needed to probe the emission. To the best of my knowledge, the only $[V(II)(bpy)_2X]^{Y,Z}$ (X = two solvent molecules or $(SO_4)^{2-}$, Y = +2 or Z = 0 with sulfate) complex exists as a $[V(bpy)_2(SO_4)]$•MeOH.[16] The heteroleptic complex's fluorescence, which had previously not been studied, was measured in methanol as it could

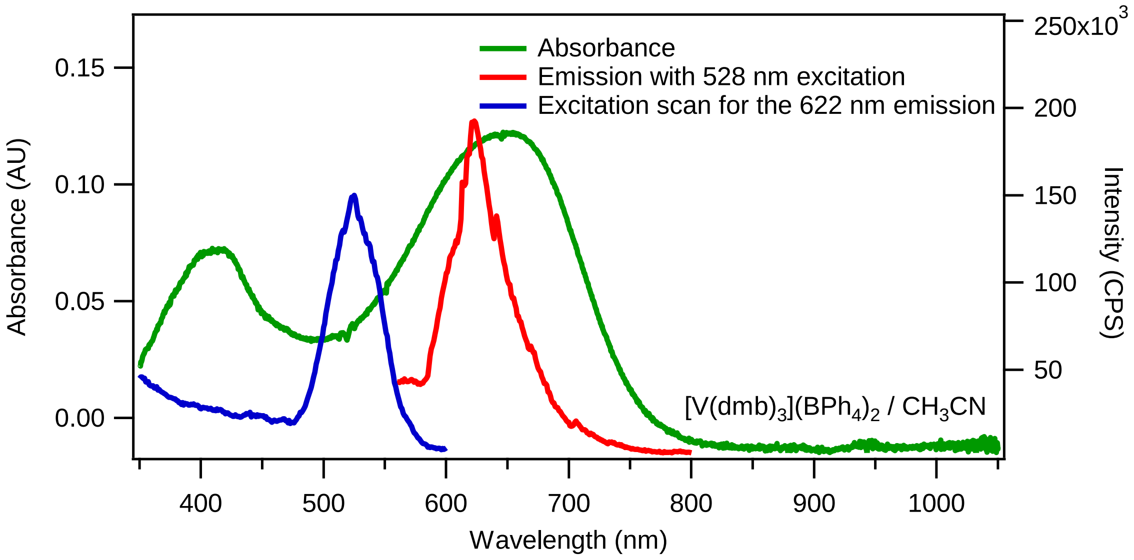

Figure A1.6. The absorbance spectrum, emission spectrum and excitation scan for **1** in acetonitrile.

therefore be manipulated in the glove box. Methanol was also the only solvent where both **2** and the heteroleptic complex were soluble. The [V(bpy)$_2$(SO$_4$)]•MeOH complex's most intense emission occurs at 610 nm when excited at 516 nm in methanol shown in Figure A10. This is very similar to that of **2**, where the 626 nm emission is most intense when excited at 530 nm. The Stokes shift is ~95 nm for both species. This data points toward the possibility that the anion doesn't play a large role in the emission. It should be noted, however, that the excitation scan for this complex also does not match the absorption spectrum for the complex and thusly is not responsible for the emission either. The only commonality that exist between the two complexes are that a V(II) center exists bound to bpy ligands. It should also be noted that the absorption spectrum of [V(bpy)$_2$(SO$_4$)]·MeOH in water agrees very well with the absorption spectrum of **2** in acetonitrile shown in Figure A11. While these are two different complexes in different solvents, the absorption profile coincidence is not expected. The authors for the synthesis of [V(bpy)$_2$(SO$_4$)]·MeOH comment that the attempts to synthesize [V(bpy)$_3$](SO$_4$) was unsuccessful due to binding of the

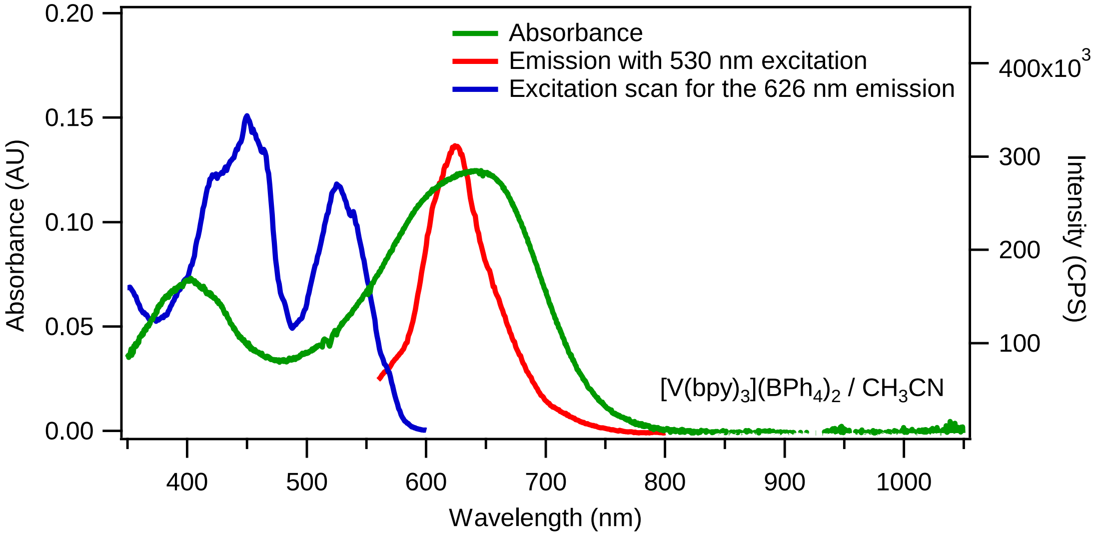

Figure A1.7. The absorbance spectrum, emission spectrum and excitation scan for **2** in acetonitrile.

sulfate.[16] At first this seems reasonable, however Herzog's method uses the same method to make $[V(bpy)_3]^{2+}$, but adds in either KI or NH_4ClO_4 to make the appropriate salt.[7] Herzog however does not comment on the formation of the $[V(bpy)_3](SO_4)$.

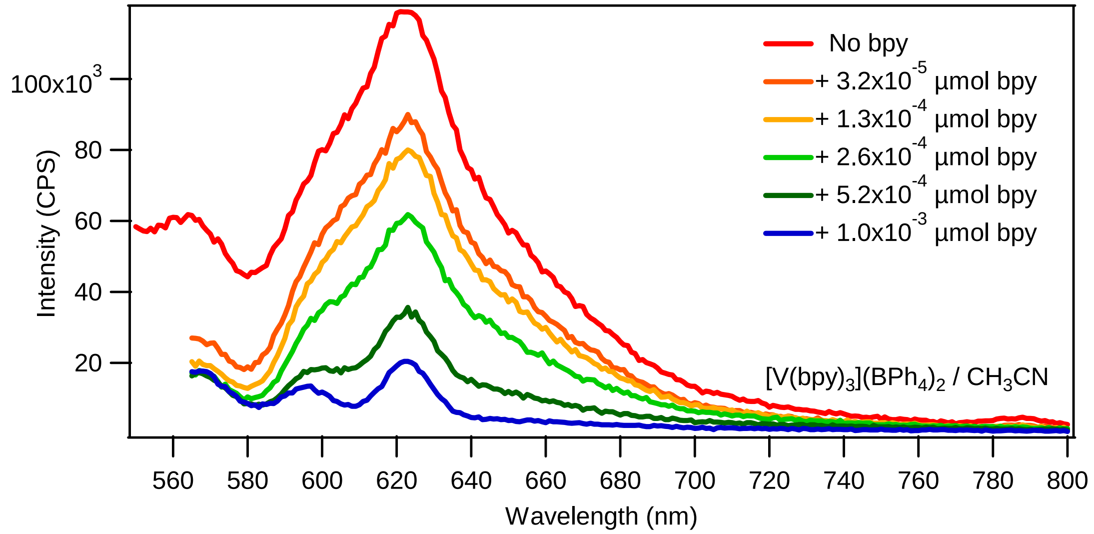

Figure A1.8. The titration of 2,2-bipyradine in a solution of **2** in acetonitrile.

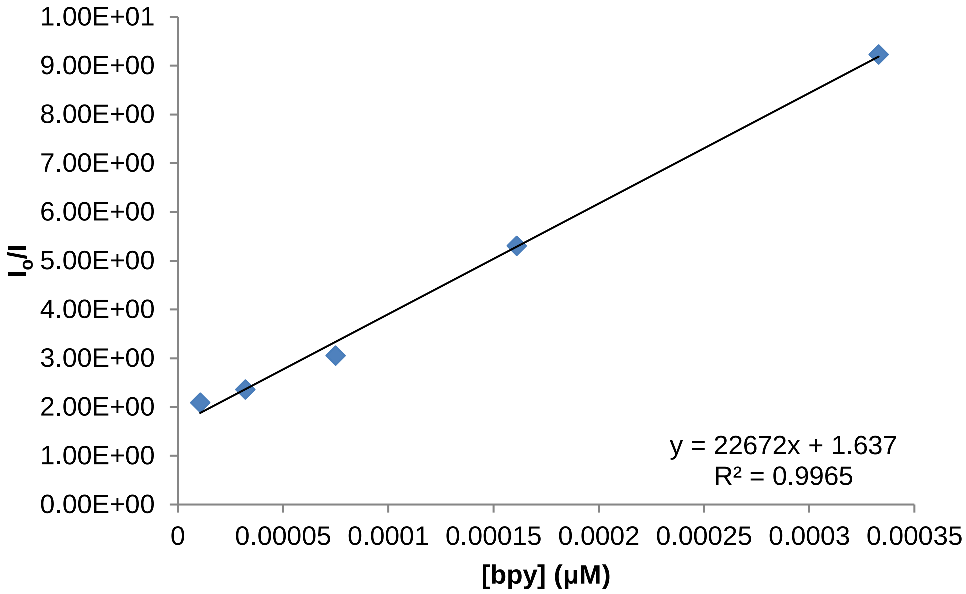

Figure A1.9. The Stern-Volmer plot showing the quenching of **2** with 2,2'-bipyridine in acetonitrile.

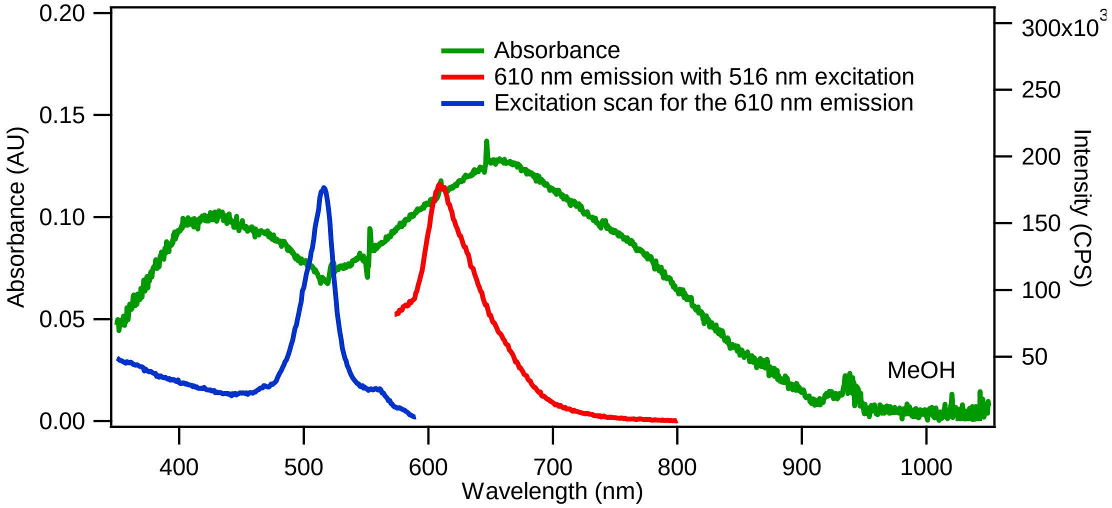

Figure A10. The absorbance spectrum, emission spectrum and excitation scan for $[V(bpy)_2SO_4]\cdot MeOH$ in methanol.

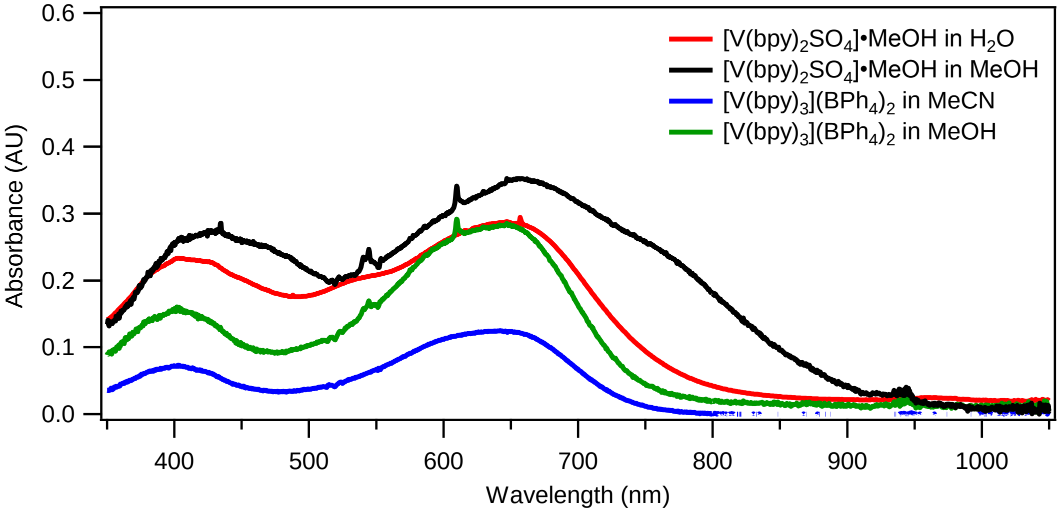

Figure A11. The absorption spectra comparing **2** in both acetonitrile and methanol to $[V(bpy)_2(SO_4)]\cdot MeOH$ in both water and methanol.

A1.5. Conclusions

This study has shown four new syntheses where the complexes show reversible redox events that respond as expected with the addition of electron-withdrawing or electron-donating groups in the 4,4'-postions of the bipyridine unit. The absorption spectra for **1**−**4** also match the trends or spectra in previous reports.[8,9] The elemental analysis for **2** agreed well with the expected composition. The elemental analyses for **1** and **3** may include solvent molecules in the sample but thermogravimetric analyses will be needed to confirm this. Complex **4** has been crystallized however co-crystallization of an impurity was found and is possibly related to decomposition products from a reduction event. The first two crystal structures of any tris-bpy vanadium (II) complex or its substituted derivatives have also been elucidated for complexes **2** and **4,** where **4** is the first to exhibit a stable ligand radical on the ligand. This ligand radical is also supported by the added low-energy, broadband absorption feature not found in **1**−**3**. Using the spectroelectrochemistry data, I was able to electrochemically simulate the absorption of the chemically reduced species, **4**.

The identity of the true emissive species has not yet been found but the best clue seems to come from the quenching study with the bipyridine ligand. To determine whether static or dynamic quenching may be occurring, one may either calculate the rate of quenching (k_q) or repeat a similar titration experiment as done as described earlier but with 4,4'-bipyridine and/or methylviologen to remove any possible bidentate binding modes of quenching (static). An emission spectrum of **2** in methanol would allow for a more relatable comparison between with the [V(bpy)$_2$(SO$_4$)]•MeOH data. It would also be helpful to monitor the emission data of [V(bpy)$_2$(SO$_4$)]•MeOH in water to correlate whether the change in absorption in methanol versus water was an artifact of solvatochromism or a possible complex decomposition. It would also be interesting to obtain the diffuse reflectance spectra of the complexes to know how the tris- or bis-ligated species' absorptions are affected with respect to the solution measurement. If these complexes are simply susceptible to ligand dissociation in solution, one may envision using organometallic ligands with similar electronics as bpy to combat ligand lability. To the best of my knowledge, these organometallic V(II) complexes do not exist in the literature and their syntheses may be difficult. Tridentate ligands like terpyridine may also be employed in the hopes to retain a stronger bond between the ligand and the metal center. Whether the fluorescence emission that occurs is due to another complex or through some dynamic process in solution, learning where the emission comes from will be telling in what the excited state potentials are providing information to screen for reactions to target for photocatalytic schemes.

REFERENCES

1. Stevenson, S. M.; Shores, M. P.; Ferreira, E. M. *Angew. Chem. Int. Ed.* **2015**, *54,* 6506.
2. Narayanam, J. M. R.; Stephenson, C. R. J. *Chem. Soc. Rev.* **2011**, *40*, 102.
3. Prier, C. K.; Rankic, D. A.; MacMillan, D. W. C. *Chem. Rev.* **2013**, *113,* 5322.
4. Appel, A. M; Bercaw, J. E.; Bocarsly, A. B.; Dobek, H.; Dubois, D. L.; Dupuis, M.; Ferry, J. G.; Fujita, E.; Hille, R.; Kenis, P. J. A.; Kerfeld, C. A.; Morris, R. H.; Peden, C. H. F.; Portis, A. R.; Ragsdale, S. W.; Rauchfuss, T. B.; Reek, J. N. H.; Seefeldt, L. C.; Thauer, R. K.; Waldrop, G. L. *Chem. Rev.* **2013**, *113*, 6621.
5. Galloni, P.; Conte, V.; Floris, B. *Coord. Chem. Rev.* **2015** in press, http://dx.doi.org/10.1016/j.ccr.2015.02.022.
6. McDaniel, A. M.; Tseng, H. W.; Damrauer, N. H.; Shores, M. P. *Inorg. Chem.* **2010**, *49*, 7981.
7. Herzog, V. *Anorg. Allg. Chem.* **1958**, *294*, 155.
8. Shah, S. S.; Maverick, A. W. *Inorg. Chem.* **1986**, *25*, 1867.
9. Bowman, A. C.; Sproules, S.; Wieghardt, K. *Inorg. Chem.* **2012**, *51*, 3707.
10. Albrecht, G. *Z. Chem.* **1963**, *3*, 182.
11. Ceroni, P.; Balzani, V. Ch. 2: Photoinduced Energy and Electron Transfer Processes, P. Ceroni (ed.), The Exploration of Supramolecular Systems and Nanostructures by Photochemical Techniques, Lecture Notes in Chemistry 78.
12. Cotton, F. A.; Falvello, L. R.; Llusar, R.; Libby, E.; Murillo, C. A.; Schwotzer, W. *Inorg. Chem.* **1986**, *25*, 3423.
13. Anderson, S. J.; Wells, F. J.; Wilkinson, G. *Polyhedron* **1988**, *7*, 2615.

14. Edema, J. J. H.; Stauthamer, W.; Bolhuis, F. V.; Gambarotta, S.; Smeets, W. J. J.; Spek, A. L. *Inorg. Chem.* **1989**, *29*, 1302.

15. Garelli, N.; Vierling, P. *J. Org. Chem.* **1992**, *16*, 3046.

16. Daniels, L. M.; Murillo, C. A.; Rodríguez, K. G. *Inorg. Chim. Acta* **1995**, *229*, 27.

17. *APEX 2*; Bruker Analytical X-Ray Systems, Inc.: Madison, WI, 2009.

18. Sheldrick, G. M. *SHELXTL* Version 6.14; Bruker Analytical X-Ray Systems, Inc.: Madison, WI, 2000.

19. Durham, B.; Caspar, J. V.; Nagle, J. K.; Meyer, T. J. *J. Am. Chem. Soc.* **1982**, *104*, 4803.

20. Wayner, D. D. M.; Dannenberg, J. J.; Griller, D. *Chem. Phys. Lett.* **1986**, *131*, 189.

21. Scarborough, C. C.; Sproules, S.; Weyhermüller, T.; DeBeer, S.; Wieghardt, K. *Inorg. Chem.* **2011**, *50*, 12446.

22. Schwalbe, M.; Schäfer, B.; Görls, H.; Rau, S; Tschierlei, S.; Schmitt, M.; Popp, J.; Vaughn, G.; Henry, W.; Vos, J. G. *Eur. J. Inorg. Chem.* **2008**, 3310.

23. Balzani, V.; Bergamini, G.; Marchioni, F.; Ceroni, P. *Coord. Chem. Rev.* **2006**, *250*, 1254.

24. McDaniel, A. M.; Rappé, A. K.; Shores, M. P. *Inorg. Chem.* **2012**, *51*, 12493.

APPENDIX 2: DEVELOPING HYBRID PAPER-BASED ANALYTICAL DEVICES FOR BIOANALYSIS

A2.1 Abstract

Following my fast flow project, I came across several results related to the multilayer paper devices that were worth pursuing. This work was submitted and accepted for use as my independent proposal.

A2.2 Introduction

As a consequence of increasing healthcare costs, physicians often deny potentially beneficial treatments to patients as a method to cut costs.[1] Alternatives, however, exist. Traditional microfluidics have proven effective at reducing costs by increasing the portability of diagnostic devices.[2] In addition to increasing portability, groups have demonstrated the ability for microfluidics to separate, sort, and analyze micron-sized particles such as single cells.[3] Paper-based analytical devices (PADs) have also proven to be cost-effective while remaining disposable, possessing the capacity to store reagents, and producing quantitative diagnostic results.[4] Instead of using bulky syringe pumps to promote pressure-driven flow in traditional microfluidics, these

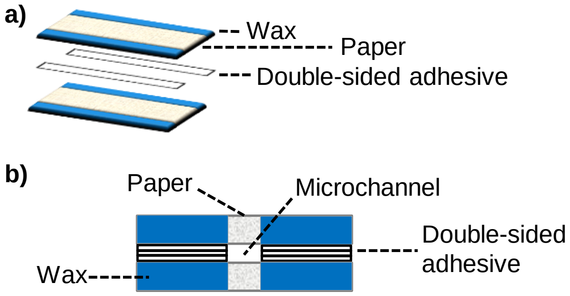

Figure A2.1. a) Schematic of fast-flow PAD with 2-layers of paper b) Cross-sectional view of fast-flow PAD highlighting the microchannel.

PADs distinctly self-transport fluids via capillary action making them ideal for point-of-care circumstances. Unfortunately, PADs are also characterized by 1) large sample loss resulting in high limits of detection, 2) slow fluid transport, and 3) the inability to mobilize large particles due to small pore sizes (~0.11 µm) in the paper.[5]

A2.3 Preliminary Results Improving PAD Performance

1) Geometry changes have led to a 94% increase in signal when compared to standard designs**, reducing sample loss**.[6]
2) Multilayer devices can flow fluids as fast as 15 $\text{cm}\cdot\text{s}^{-1}$ (**168× increase in flow rate**) with a volumetric flow rate of 16.3 $\text{mL}\cdot\text{min}^{-1}$ (Fig. 1).[7]
3) Spiral device devices maintain fast flow (Fig. 3a)
4) New hybrid paper-based analytical devices (H-PADs) **can transport and visualize micron-sized particles** that would previously be entrapped in the small pores of paper in traditional PADs. (Fig. 2).

A2.4 Project Goals

The ability to flow, separate and analyze particles in these new H-PADs provides precedence for exploring their fabrication with patternable materials such quartz, glass, polydimethylsiloxane (PDMS), poly(methyl methacrylate) (PMMA), and 3D printed materials (methacrylate-based, proprietary material). To date, no one has sandwiched these materials to paper with or without patterned channels into these materials, and examined the fluid dynamics as a function of their physical and chemical differences. I plan to examine flow rate changes due to differences in the wettability, surface roughness, surface charge, and chemical functionalities of these patternable materials.[8] I will then explore how changes in the shape/geometry of the channel (circular, square, triangular, height, width, etc.) impact the fluid dynamics.[9]

After better understanding the flow rate in these devices, I will catalog the motion of particles and how relative particle size changes affect this motion. Then I will explore how patterned microstructures further affect the movement of particles. This will be done in straight and spiral shaped channels. The use of microstructures and spiral channels have been demonstrated by others to separate particles, however, no one has integrated these into self-pumping devices created by the proposed H-PADs.[10] The utility of this technology for point-of-care diagnostics will be explored through the size separation of biologically relevant particles such as red and white blood cells.

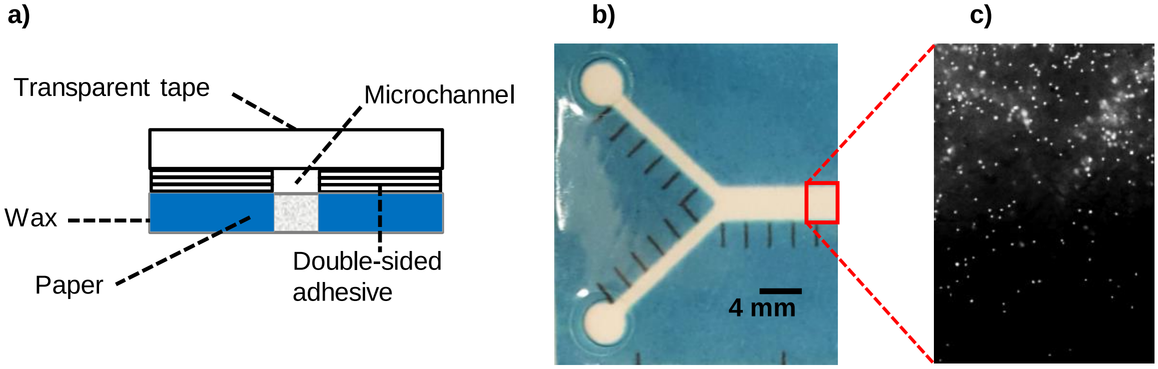

Figure A2.2. a) Cross-sectional view of microchannel-containing, H-PAD with 1-layer of paper. b) Photograph of this device with two circular inlets. The top inlet transported fluorescent beads suspended in water; at the same time, the bottom inlet transported only water. c) Fluorescence microscopy image of the channel after the two fluids were added to their respective inlets and were transported down the channel.

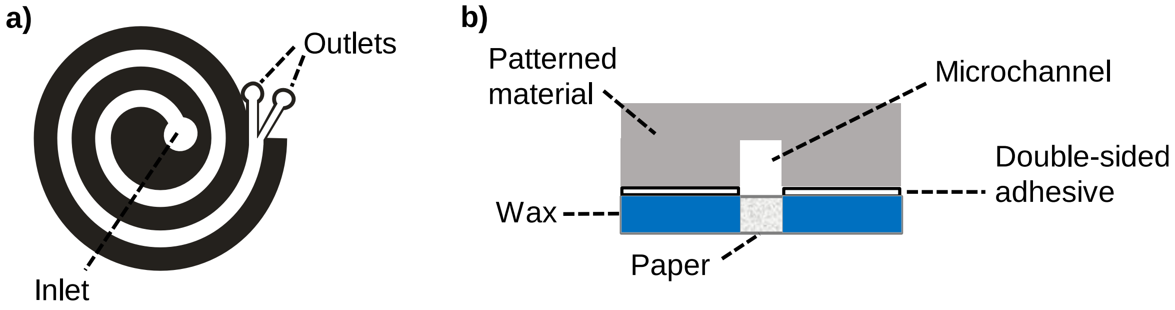

Figure A2.3. a) Spiral device design for size separation of particles. b) Cross-sectional view of proposed patterned hybrid paper-based microfluidic device (H-PAD).

A2.5 Research Question

How does varying the device material and architecture affect the flow rate and path of micron-sized particles in H-PADs?

A2.6 Specific Aims

1) Establish understanding of how the flow rate changes as a function of surface chemistry (wettability, roughness, surface charge) between materials in H-PADs.
2) Explore the effect of channel geometry (shape, channel height, channel width) on the fluid dynamics with the patterned materials.
3) Catalog the motion of particles of various sizes in H-PADs.
4) Implement microstructures and spiral channels to passively sort particles and cells by size.

A2.7 Research Aim Details

Aim 1: *Establish understanding of how the flow rate changes as a function of surface wettability between materials in H-PADs.*

The hydrophilic pores of paper drive the transport of water in PADs. I recently demonstrated that multilayered PADs (Figure A2.1a) have exhibited significantly (168×) faster transport of solutions than single layered PADs. However preliminary work has demonstrated that fast flow properties are maintained when replacing one of the paper layers in the multilayered devices with packing tape (Figure A2.2b,c). Packing tape is transparent which makes it amenable to observing particle transport and is expected to allow for less sample loss associated with paper. Despite packing tape's transparency and low-cost, it is quite flexible and can sag, changing the microfluidic channel geometry thus affecting the fluid dynamics. The adhesive of the packing tape may even interfere with a given assay on paper. Thus, stiff and inert materials common to microfluidics will be explored to replace the packing tape. The non-paper materials proposed for this comparison will be quartz, glass, polydimethylsiloxane (PDMS), poly(methyl methacrylate) (PMMA), and 3D printed materials (methacrylate-based, proprietary material).

As paper's hydrophilic surface allows for fluid transport, it is also presumed that non-porous hydrophilic materials will also allow for fluid transport. Capillary rise in glass tubing was first documented by Leonardo da Vinci, however these all-glass systems are not suited for reagent storage, an advantage to using PADs for performing point-of-need analyses. Therefore, it is important to construct multilayered H-PADs to balance reagent storage with fast flow properties and optical transparency. Contact angle measurements can probe the hydrophilicity or hydrophobicity of surfaces such as the ones proposed to build H-PADs. These measurements are completed by measuring the angle at which a droplet interacts with a surface. A surface is

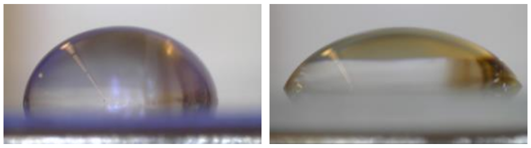

PMMA (90°) Glass (61°)

Figure A2.4. Photographs showing the contact angle of water on PMMA and glass substrates.

described as hydrophobic if its contact angle is >90° and hydrophilic if the contact angle is less than <90°. These materials' contact angles will thus first be measured as shown in Figure A2.4. It is expected that more hydrophilic materials will transport fluids faster in H-PADs than more hydrophobic ones. It is also expected that as a result of the varying contact angles inherent to varying materials, I will be able to tune the velocity of fluid velocity simply by substituting the materials. The velocity will also be tuned by varying the number of double-sided tape layers in my devices. This additional method to tune the fluid velocity is convenient when a given material may be preferred for a given analytical technique (infrared spectroscopy, electronic absorbance spectroscopy, fluorescence spectroscopy, chemiluminescence etc.).

The devices to measure the flow rate as a function of material and number of double-sided tape layers will be designed with simple straight channels. For these H-PADs, a simple straight channel design with tick marks to quantify the velocity will be printed on Whatman Grade 1 Chromatography paper with a wax printer (Xerox ColorQube). These paper layers will then be sandwiched to the materials mentioned above with double-sided tape to adhere them together. Once the devices are fabricated, a fixed volume of food dye will be added to the inlet. A video of the dye moving through the device will be recorded with a digital camera. Distance-time plots will then be constructed from the data collected with the digital camera.

Preliminary work comparing flow rates of H-PADs with glass and PMMA has shown that the more hydrophilic glass (61°) moves water faster than the PMMA (90°) device. With this first evidence, I am confident that devices made from more hydrophilic materials will show faster flow rates than the devices made from more hydrophobic ones. However, I also believe that the surface roughness will play a role in tuning the flow rates. My intuition is that rougher materials will exhibit higher contact angles with water and thus provide slower flow rates. This hypothesis is consistent with literature as rougher surfaces can improve hydrophobicity in superhydrophobic materials, materials with contact angles >150°.[11] Fortunately, most of the proposed materials' surfaces can be roughened through mechanical abrasion or chemical treatment. The surface roughness will be measured with atomic force microscopy or optical profilometry to observe how rough and how conformal features on the surface are at different areas of the material.

Currently, issues such as slow flow rates, sample loss and high detection limits hinder PADs from becoming more widely adopted in point-of-need analysis. Unfortunately, the field does not regularly address these issues. With strong foundations for understanding the fluid dynamics (ex. tuning the fast flow rate) of these proposed H-PADs, I can address the fore mentioned issues as well as expand the types of analytes to cells and other micron-sized particles, which have remained elusive to this class of analytical devices due to the small pore size of paper. Understanding how the surface chemistry and surface morphology effects the fluid dynamics in PADs allows for better design of these devices for the needs of a specific assay and to improve analysis. Therefore, these studies will help develop high performance and user-friendly analytical devices to empower citizen scientists.

A2.8 Potential Challenges & Solutions

Sample loss and slow fluid velocity are inherent challenges in PADs, however I previously demonstrated methods to solve both challenges. Another potential pitfall is that the fluid dynamics of pressure-driven flow in traditional microfluidics will likely differ from H-PADs. However, I expect that these differences will open new possibilities for diagnostics and add to the fluid dynamics narrative.

A2.9 Summary & Outlook

The research proposed seeks to grow and combine traditional and paper-based microfluidics with the careful construction of H-PADs. This approach will be applied to biomedical analysis and is distinct in that the fluid flow is generated though the hydrophilic paper networks which eliminates the need for bulky syringe pumps. This self-pumping property makes H-PADs particularly desirable for analysis in resource-limited settings. The concepts learned in this study will benefit both those in the fluid dynamics and diagnostics communities. Development of these proposed H-PADs offer customizable point-of-care analysis by the facile integration of wires (impedance spectroscopy, amperometry, etc.) and optically transparent materials (infrared spectroscopy, electronic absorbance spectroscopy, fluorescence spectroscopy, chemiluminescence, etc.). I am confident that this technology has the capability to produce a practical product that can lower healthcare costs.

REFERENCES

1. (a) Peter, A. U., Physicians, Thou Shalt Ration: The Necessary Role of Bedside Rationing in Controlling Healthcare Costs. *HealthcarePapers* **2002,** *2* (2), 10-21; (b) Scheunemann, L. P.; White, D. B., The Ethics and Reality of Rationing in Medicine. *Chest* **2011,** *140* (6), 1625-1632.
2. Sackmann, E. K.; Fulton, A. L.; Beebe, D. J., The present and future role of microfluidics in biomedical research. *Nature* **2014,** *507*, 181.
3. (a) Nivedita, N.; Garg, N.; Lee, A. P.; Papautsky, I., A high throughput microfluidic platform for size-selective enrichment of cell populations in tissue and blood samples. *Analyst* **2017,** *142* (14), 2558-2569; (b) Kang, C.-C.; Yamauchi, K. A.; Vlassakis, J.; Sinkala, E.; Duncombe, T. A.; Herr, A. E., Single cell–resolution western blotting. *Nature Protocols* **2016,** *11*, 1508; (c) Nivedita, N.; Ligrani, P.; Papautsky, I., Dean Flow Dynamics in Low-Aspect Ratio Spiral Microchannels. *Scientific Reports* **2017,** *7*, 44072.
4. Yang, Y.; Noviana, E.; Nguyen, M. P.; Geiss, B. J.; Dandy, D. S.; Henry, C. S., Paper-Based Microfluidic Devices: Emerging Themes and Applications. *Analytical Chemistry* **2017,** *89* (1), 71-91.
5. Cate, D. M.; Adkins, J. A.; Mettakoonpitak, J.; Henry, C. S., Recent Developments in Paper-Based Microfluidic Devices. *Analytical Chemistry* **2015,** *87* (1), 19-41.
6. Nguyen, M. P.; Meredith, N. A.; Kelly, S. P.; Henry, C. S., Design Considerations for Reducing Sample Loss in Microfluidic Paper-Based Analytical Devices. *Analytica Chimica Acta* **2018**.

7. Channon, R. B.; Nguyen, M.; Scorzelli, A.; Henry, E.; Volckens, J.; Dandy, D.; Henry, C., Rapid Flow in Multilayer Microfluidic Paper-Based Analytical Devices. *Lab on a Chip* **2018**.

8. da Silva, E.; Santhiago, M.; de Souza, F. R.; Coltro, W. K. T.; Kubota, L. T., Triboelectric effect as a new strategy for sealing and controlling the flow in paper-based devices. *Lab on a Chip* **2015,** *15* (7), 1651-1655.

9. Abdelgawad, M.; Wu, C.; Chien, W.-Y.; Geddie, W. R.; Jewett, M. A. S.; Sun, Y., A fast and simple method to fabricate circular microchannels in polydimethylsiloxane (PDMS). *Lab on a Chip* **2011,** *11* (3), 545-551.

10. (a) Wang, L.; Dandy, D. S., High-Throughput Inertial Focusing of Micrometer- and Sub-Micrometer-Sized Particles Separation. *Advanced Science* **2017,** *4* (10), 1700153-n/a; (b) Patel, M. V.; Nanayakkara, I. A.; Simon, M. G.; Lee, A. P., Cavity-induced microstreaming for simultaneous on-chip pumping and size-based separation of cells and particles. *Lab on a Chip* **2014,** *14* (19), 3860-3872; (c) Wang, X.; Liedert, C.; Liedert, R.; Papautsky, I., A disposable, roll-to-roll hot-embossed inertial microfluidic device for size-based sorting of microbeads and cells. *Lab on a Chip* **2016,** *16* (10), 1821-1830.

11. Zhang, X.; Shi, F.; Niu, J.; Jiang, Y.; Wang, Z., Superhydrophobic surfaces: from structural control to functional application. *Journal of Materials Chemistry* **2008,** *18* (6), 621-633.

APPENDIX 3. ELECTRONIC SUPPORTING INFORMATION: DESIGN CONSIDERATIONS FOR REDUCING SAMPLE LOSS IN MICROFLUIDIC PAPER-BASED ANALYTICAL DEVICES

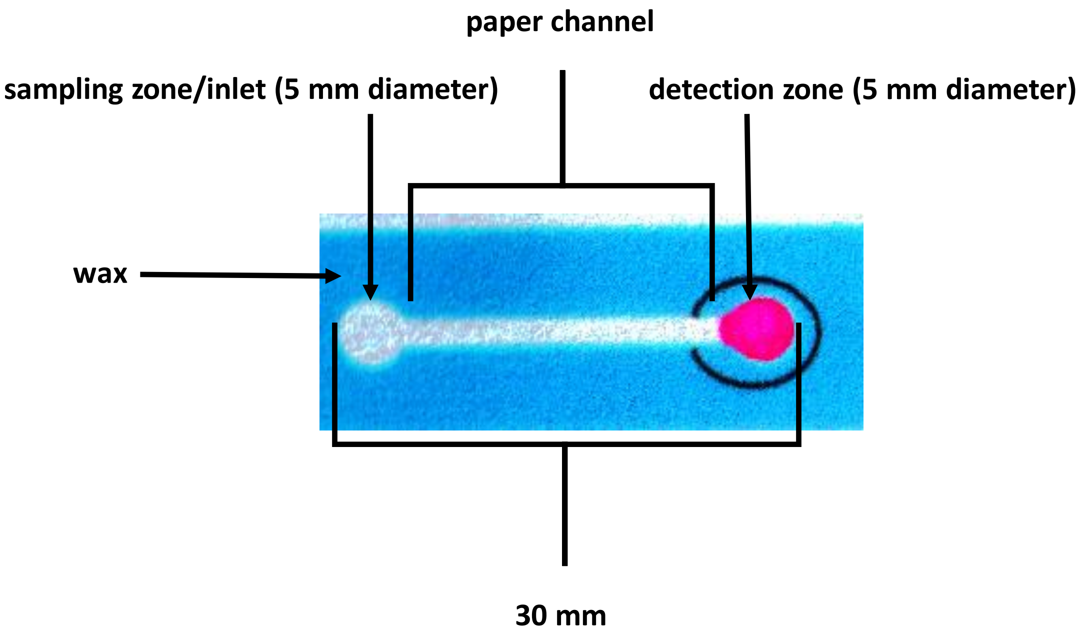

Figure S2.2.1. Diagram of paper device.

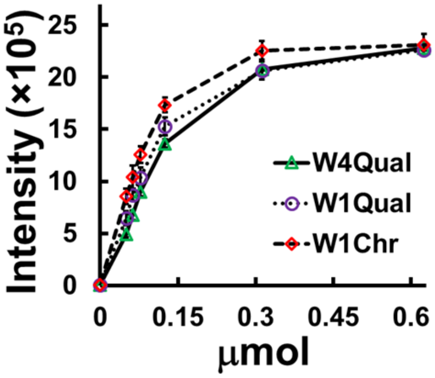

Figure S2.2. Plot comparing intensity of Ni(dmg)$_2$ on the standard channel with three different paper types: W4Qual, W1Qual, and W1Chr.

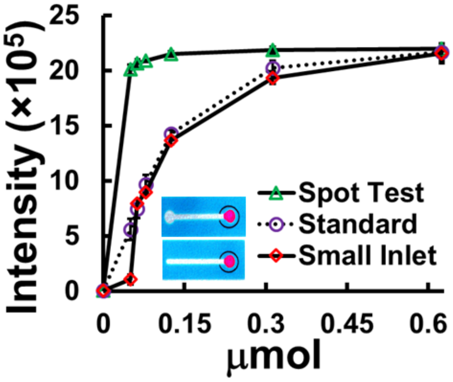

Figure S2.3. Comparison of the small inlet design to the circular inlet of the standard device.

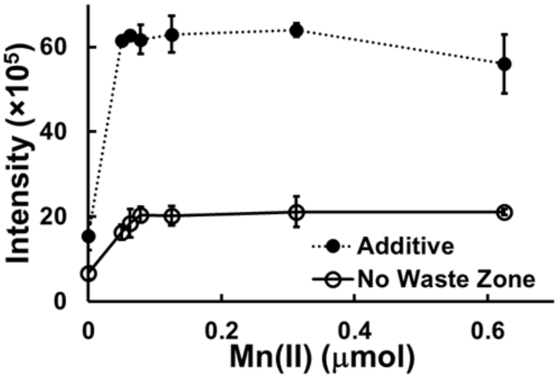

Figure S2.4. The comparison of the standard test versus the additive test with $Mn(PAR)_2$.

APPENDIX 4. ELECTRONIC SUPPORTING INFORMATION: RAPID FLOW IN MULTILAYER MICROFLUIDIC PAPER-BASED ANALYTICAL DEVICES

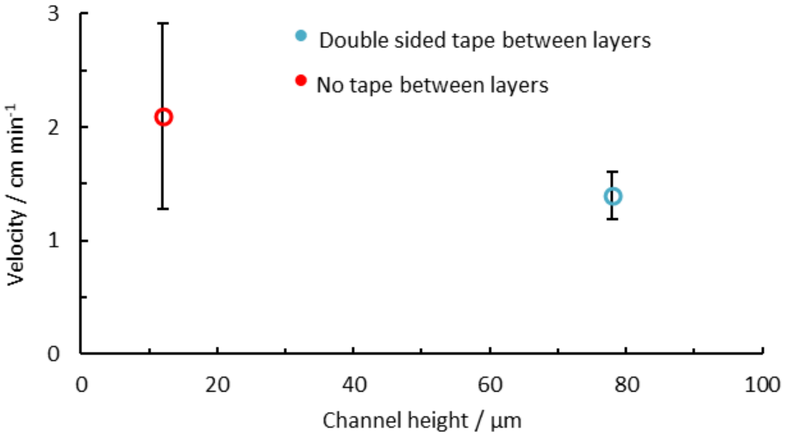

Figure S3.1. Effect of confining channel height with or without double sided sticky tape on the velocity for multilayer µPADs, vertical orientation, (n = 5) flow taken up to 5.55 cm. The channel height for the untapped device is an estimate based on previous multilayer

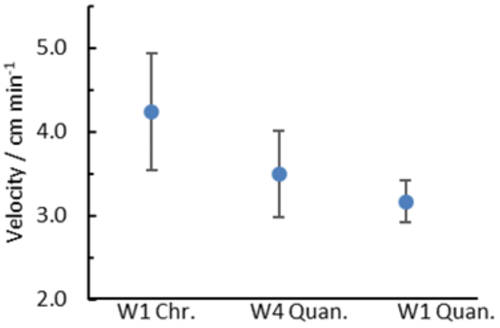

Figure S3.2 Effect of paper type on flow rate using vertical µPADs with 3 layers of tape between the two paper layers. Velocity is calculated for flow up to 5.55 cm (n = 5).

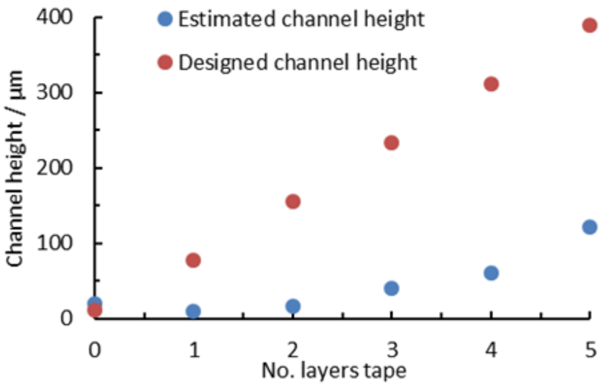

Figure S3.3 Estimated channel height from theoretical models based on the observed device velocities and actual channel height based on design of the multilayer μPADs, for horizontally orientated devices.

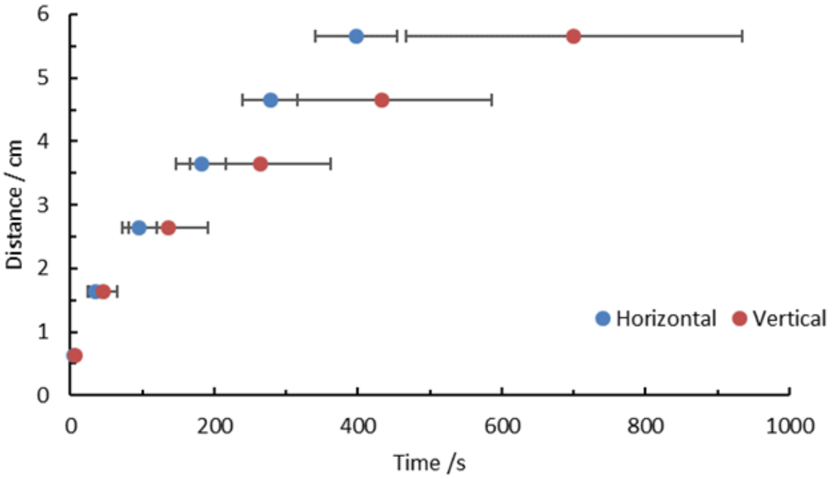

Figure S3.4. Length traversed down straight channel 1-layer of paper μPADs with horizontal and vertical orientation (n = 5).

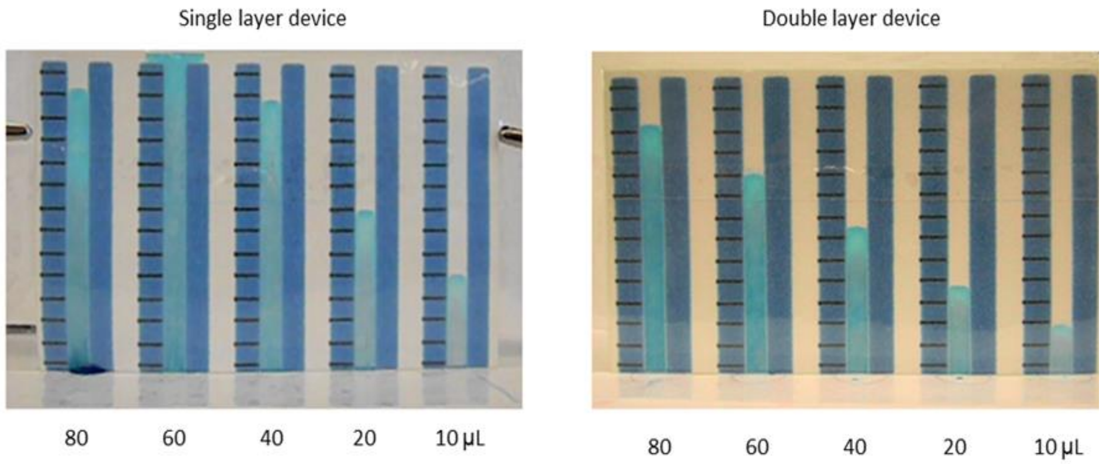

Figure S3.5. Photograph of volume dependent fluid transport in a single vs double layer device (10, 20, 40, 60, 80 µL), as described in Figure 5 of the main paper. Note the separation of dye and water after long periods of time (dark to light blue).

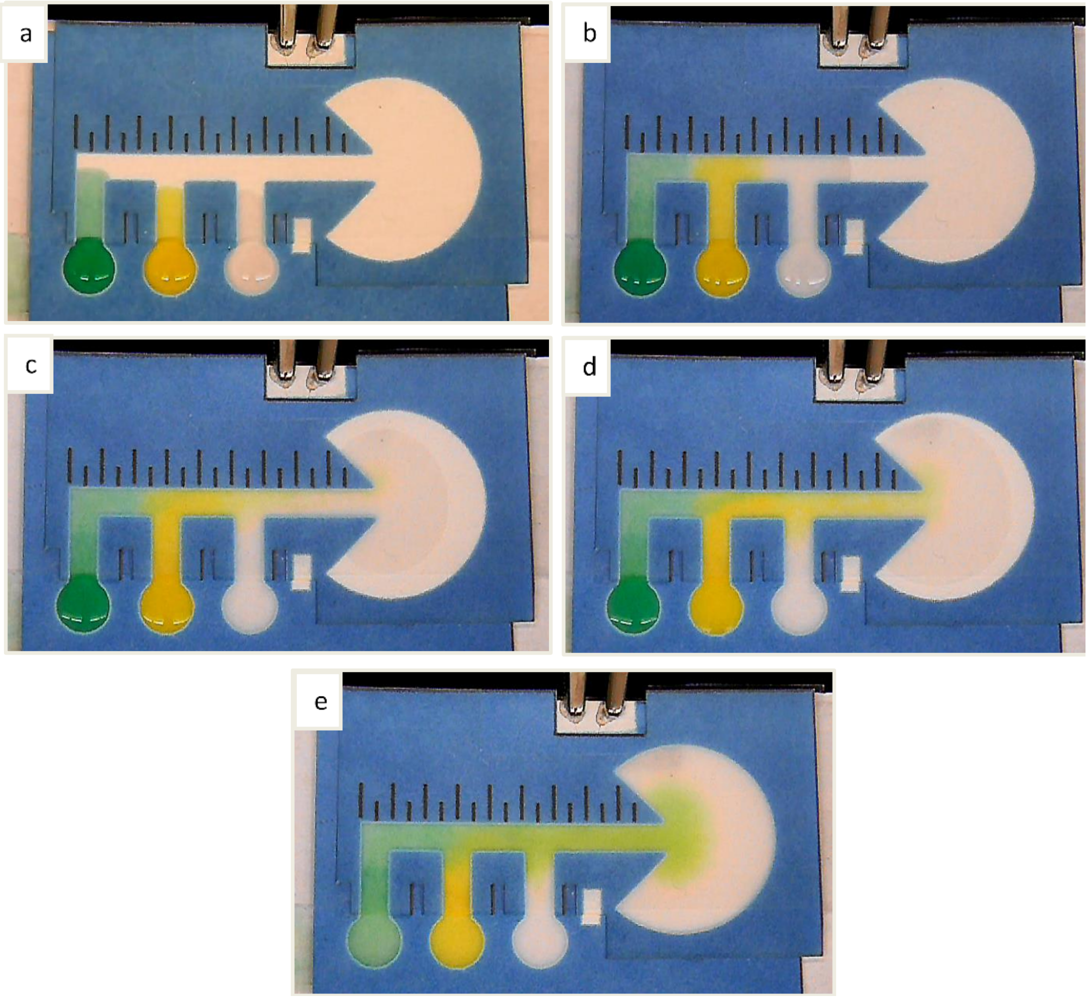

Figure S3.6. Images of a multilayered 3DPN device using 3 layers of tape between the layers, at different stages of sequential injection (Figure 6 if main paper, blue line). The 80 µL injections from right to left are as follows: KNO_3, 1 mM $FcTMA^+$ with 0.1 M KNO_3 spiked with a yellow dye, and finally 0.1 M KNO_3 spiked with a green dye. The snapshots represent a) addition of sample to wells and wicking up the inlet legs, b) KNO_3 reaching the electrodes, c) $FcTMA^+$ reaching the electrodes, d) The maximum current signal from the $FcTMA^+$ injection, e) the final (wash) KNO_3 injection washes the $FcTMA^+$ past the electrode and the flow ceases as the fan is filled and the sample wells are depleted.

APPENDIX 5. ELECTRONIC SUPPORTING INFORMATION: READ-BY-EYE QUANTIFICATION OF ALUMINUM (III) IN A DISTANCE-BASED MICROFLUIDIC PAPER-BASED ANALYTICAL DEVICE

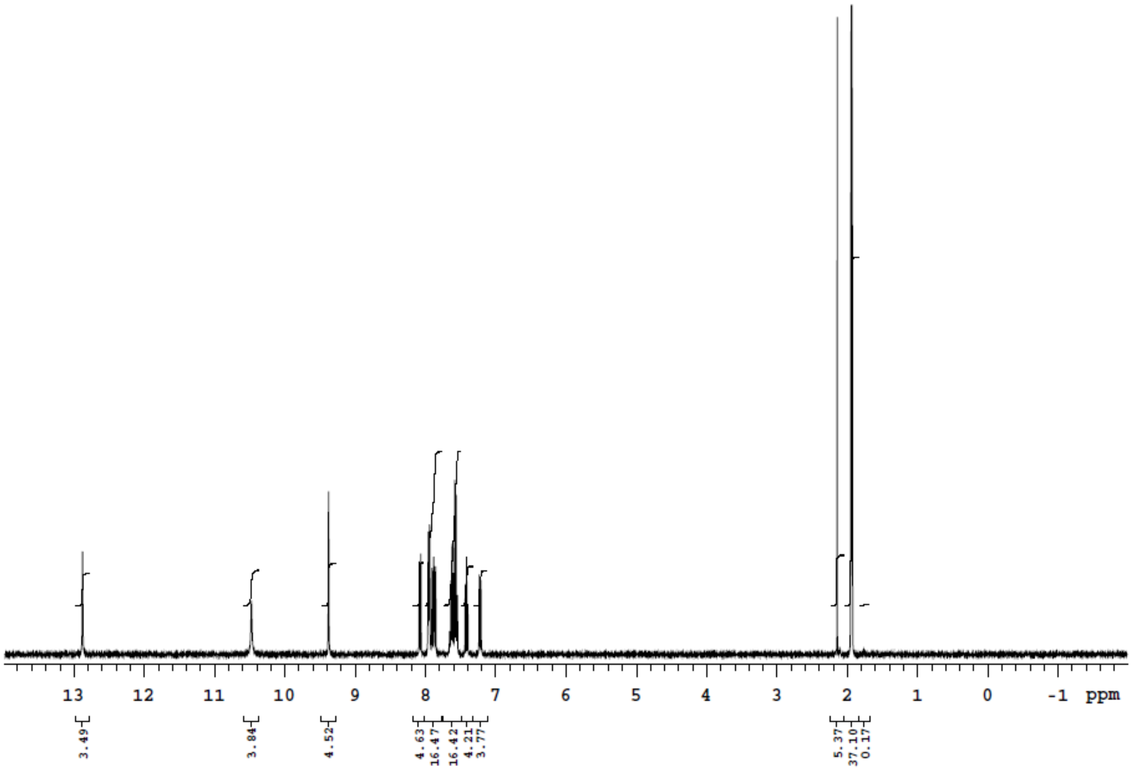

Figure S4.1. ^{1}H NMR spectrum of ligand “L” in CD_3CN.

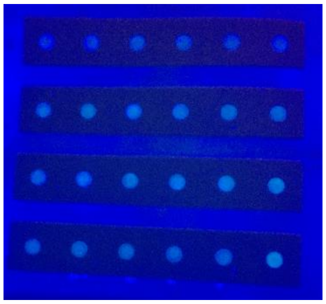

Figure S4.2. Photograph of Al(III) spot tests showing no discernable emission intensity with increasing Al(III) concentration.

Table S4.1. Summary of metal concentrations of in Gold King Mine samples as measured by ICP-MS.

Analyte	Mill Lower Tunnel (ppb)	Plant Influent (ppb)
In	34.512679	22.459319
As	541.085775	1.578
Ag	0.650464	0.070707
Al	9821.243795	11123.61502
Cd	409.139188	94.272814
Pb	786.698064	14.131592
Cu	10008.72723	2572.06173
Mn	6325.09762	---
Mg	19471.12938	44043.90718
Ni	153.361413	153.370329
Fe	96068.58133	32104.25323
Zn	79193.57916	26777.34476
Ca	31980.79273	144459.8

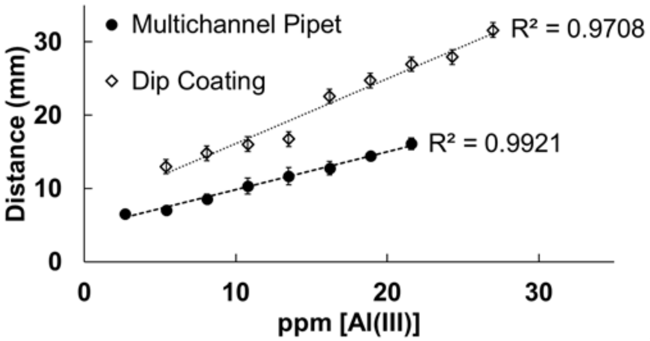

Figure S4.3. Plot showing the distance-dependence on the concentration of Al(III) with varying ligand deposition techniques.

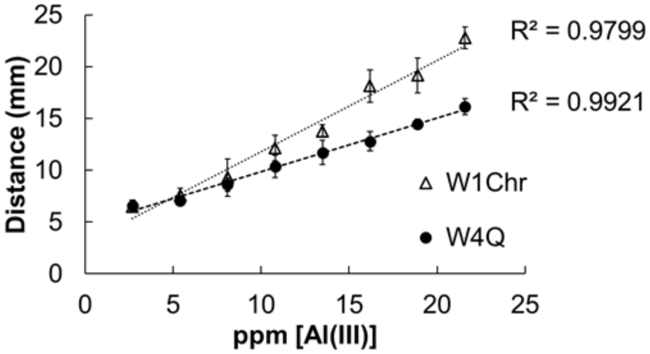

Figure S4.4. Plot showing the distance-dependence on the concentration of Al(III) with varying paper types.

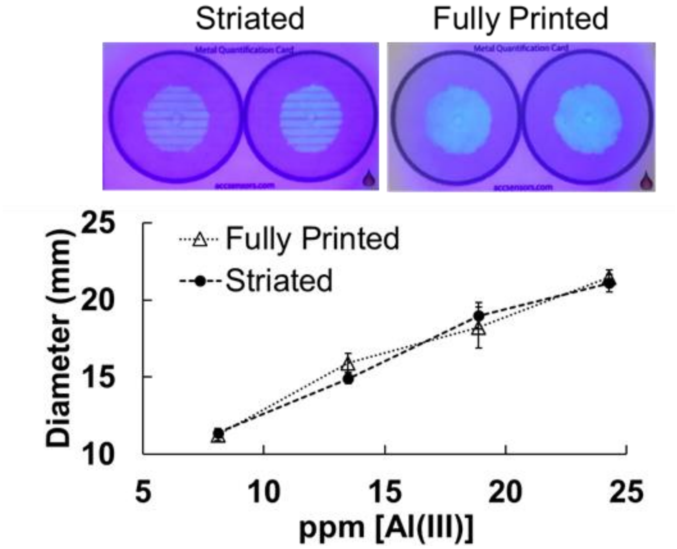

Figure S4.5. (Above) Photographs of striated versus fully printed devices. (Below) Plot showing the distance-dependence on the concentration of Al(III) with clean (fully printed) versus clogged print heads (striated).